Karlsruhe Institute of Technology

Study of Cosmic-ray Anisotropies with KASCADE, KASCADE-Grande and IceTop

Untersuchung der Anisotropien kosmischer Strahlung mit KASCADE, KASCADE-Grande und IceTop

Master's Thesis of

Joshua Turnwald

At the KIT Department of Physics
Institute for Experimental Particle Physics (ETP)
and Institute for Astroparticle Physics (IAP)

First examiner:	Prof. Dr. Ralph Engel
Second examiner:	Prof. Dr. Thomas Schwetz-Mangold
Advisor:	Dr. Donghwa Kang

14 March 2025 – 13 March 2026

I declare that I have developed and written the enclosed thesis completely by myself. I have not used any other than the aids that I have mentioned. I have marked all parts of the thesis that I have included from referenced literature, either in their original wording or paraphrasing their contents. I have followed the by-laws to implement scientific integrity at KIT.

Karlsruhe, 13 March 2026

. . . . . .
(Joshua Turnwald)

. . . . . .
(Prof. Dr. Ralph Engel)

Abstract

Cosmic rays are extraterrestrial charged particles that mainly consist of protons, helium, and heavier nuclei. High-energy cosmic rays must be detected indirectly by observing extensive air showers that form in Earth's atmosphere following interactions of primary cosmic rays. Numerous questions remain regarding the origin and acceleration mechanisms of these particles. Despite significant advancements in detector performance in recent years, no cosmic-ray source has been conclusively identified, and the causes of spectral features such as the knee remain under debate. Because cosmic rays are charged particles, they are deflected by galactic magnetic fields, resulting in an incoming cosmic-ray flux that is largely isotropic, with anisotropies in the order of 10^{-3} to 10^{-4}. Investigating these anisotropies in the arrival-direction distribution may provide insights into the distribution of local sources, cosmic-ray propagation, and the transition from galactic to extragalactic cosmic rays.

KASCADE and its extension KASCADE-Grande were cosmic-ray detectors located in Karlsruhe that measure cosmic ray-induced air showers at energies ranging from 10^{14} to 10^{18} eV. In this study, for the first time the complete KASCADE dataset from 1998 to 2013 was analysed to investigate large- and medium-scale anisotropies. The KASCADE-Grande dataset from 2004 to 2013 was also examined. An iterative maximum-likelihood reconstruction was employed to estimate the relative intensity, detector acceptance, and the expected number of isotropic background events per sidereal time bin.

For KASCADE, a dipole with a maximum significance of 3.66 σ was identified for the energy bin with a median energy of 180 TeV, and an overall dipole for the complete dataset exhibited a significance of 4.01 σ. The maximum medium-scale significance observed was 3.77 σ at a median energy of 180 TeV. In contrast, KASCADE-Grande did not reveal any significant large- or medium-scale anisotropy in the PeV energy range.

The iterative likelihood method allows a combined analysis across multiple detectors. A comparison of the results from previous IceTop analyses and the KASCADE with KASCADE-Grande results from this work was performed with respect to the median energy and median rigidity of the bins. Bins with rigidity distributions similar to IceTop were identified for KASCADE and KASCADE-Grande, allowing for a combined analysis. However, as only the 1% burn sample of the IceTop data was available, no quantitative results could yet be obtained. Nonetheless, this approach demonstrates the possibilities and lays the groundwork for future analysis for the combination of KASCADE-Grande and KASCADE with the full data set of IceTop.

Zusammenfassung

Kosmische Strahlung besteht hauptsächlich aus Protonen, Helium und anderen schwereren Nukliden extraterrestrischen Ursprungs. Kosmische Strahlung mit hoher Energie wird indirekt durch die Messung von Luftschauern, die bei der Interaktion der Primärteilchen mit der Atmosphäre entstehen, gemessen. Zahlreiche Fragen bezüglich der Herkunft, der Beschleunigungsmechanismen und der Propagation sind noch unbeantwortet. Trotz der großen Fortschritte in der Entwicklung von Detektoren in den vergangenen Jahren konnte noch keine Quelle für kosmische Strahlung eindeutig identifiziert werden und die Ursprünge für die Merkmale im Spektrum der kosmischen Strahlung wie z.B. das Knie sind immer noch umstritten. Da kosmische Strahlung geladene Teilchen sind, werden sie von galaktischen Magnetfeldern abgelenkt, wodurch der ankommende Fluss äußerst isotrop ist und Anisotropien nur in der Größenordnung von 10^{-3} bis 10^{-4} auftreten. Die Untersuchung dieser Anisotropien in der Verteilung der Ankunftsrichtungen könnte Aufschluss über die Verteilung lokaler Quellen, die Propagation der Teilchen und den Übergang von galaktischer zu extragalaktischer Strahlung geben.

KASCADE und seine Erweiterung KASCADE-Grande waren Detektoren für kosmische Strahlung in Karlsruhe, welche die Teilchenschauer in der Atmosphäre messen, die von Primärteilchen im Energiebereich von 10^{14} bis 10^{18} eV erzeugt werden. In dieser Arbeit wird erstmals der komplette Datensatz von KASCADE im Messzeitraum von 1998 bis 2013 analysiert und die Anisotropien auf großen und mittleren Skalen bestimmt. Um die relative Intensität, die Detektor-Akzeptanz und die erwartete Anzahl an Ereignisse pro siderischem Zeitintervall zu bestimmen, wird eine iterative Maximum-Likelihood-Rekonstruktion verwendet.

Für den ersten Energiebereich des KASCADE-Datensatzes mit einer Medianenergie von 180 TeV wurde ein Dipol mit der höchsten Signifikanz von 3.66 σ gemessen. Für das komplette Datenset wurde eine Signifikanz von 4.01 σ gefunden. Die maximale Signifikanz für Anisotropien auf mittleren Skalen betrug für diese Energie 3.77 σ. Im Gegensatz dazu konnte für KASCADE-Grande keine signifikante Anisotropie auf großen oder mittleren Skalen gefunden werden.

Die iterative Likelihood-Methode erlaubt es, Datensätze von verschiedenen Detektoren zu kombinieren. Ein Vergleich der Ergebnisse zwischen vorherigen IceTop Studien und KASCADE sowie KASCADE-Grande wurde mit Bezug auf die Medianenergie und die Median magnetische Steifigkeit (Rigidity) durchgeführt. Außerdem wurden Energie-Bins für KASCADE und KASCADE-Grande bestimmt, die mit der Verteilung der Rigidity von IceTop übereinstimmen. Da aber nur ein Burnsample von 1% der Daten zur Verfügung stand, konnte keine quantitative Analyse durchgeführt werden. Trotzdem konnten die Möglichkeiten einer

kombinierten Analyse aufgezeigt werden und die Grundlage für eine zukünftige Analyse von KASCADE und KASCADE-Grande mit dem kompletten IceTop-Datensatz geschaffen werden.

Contents

1. Introduction

Earth's atmosphere is constantly hit by high-energy charged particles moving at relativistic speeds. These particles, which mainly consist of protons, helium, and other heavier nuclei, are referred to as cosmic rays. Many questions about these particles like their origin, acceleration mechanisms and propagation through the interstellar medium, are still unanswered. The discovery of cosmic rays in the 1910s laid the groundwork for not only high-energy particle physics but also astroparticle physics. They are studied either through direct measurements for lower-energy cosmic rays or by the measurement of air showers produced by interactions of the primary particle with the atmosphere. In recent years, multi-messenger astronomy allowed for a new approach in cosmic ray research by combining information from charged cosmic rays with observations of gamma rays, neutrinos, and gravitational waves.

Examples of indirect detectors are the KASCADE and KASCADE-Grande detectors located in Karlsruhe. Through the measurements of the distribution of charged air-shower particles at ground level, the energy and direction of the primary can be estimated. For indirect measurements, the charge and mass of the primary particles can be estimated on an event-by-event basis, but only with limited resolution and shower fluctuations. Another detector is IceTop, the surface detector of the IceCube Neutrino Observatory at the South Pole.

Since cosmic rays are charged particles, they are deflected by magnetic fields. This leads to a diffusive motion of the cosmic rays throughout the Galaxy. As these deflections obscure the directional information about the origin, the search for cosmic-ray sources is difficult. Most of the cosmic rays are thought to originate from the sun for lower energies or from our Galaxy, but there also seems to be an extragalactic component. With the study of the variations in the arrival direction, i.e. anisotropies in the cosmic-ray flux, information about the origin, the propagation in our Galaxy or the distribution of local sources might be obtained.

The iterative likelihood method used in this work allows for the combination of multiple detectors. This enables a combination of multiple datasets, which extends the field of view and increases the available statistics. A limited field of view only allows for the reconstruction of the pseudo-multipole moments and can cause degeneracy between the multipole moments, especially for lower multipoles [12]. Therefore, a full sky analysis might lower the systematic effects on the power spectrum.

In this work, the large- and medium-scale anisotropies from KASCADE and KASCADE-Grande are analysed. The IceTop Burnsample will also be analysed and a comparison between the previous IceTop results [8] and the KASCADE/KASCADE-Grande results in

relation to the median energy and median rigidity is performed. With the IceTop rigidity distributions obtained from simulations, selection cuts for KASCADE and KASCADE-Grande bins with similar rigidity distributions are found and a qualitative analysis of the combined bins is performed.

2. Foundations

This chapter provides a brief introduction to cosmic rays and the foundations of the topic. After a short description of the history of cosmic-ray measurements, their composition and spectrum are described. Possible acceleration mechanisms and the basics of extensive air showers are then introduced. Finally, the current understanding of cosmic-ray anisotropies and an overview of current measurements are presented.

2.1. Cosmic Rays

History

The study of cosmic rays spans more than 100 years of investigation. It began with Becquerel's discovery of natural radioactivity in 1896. The source of this natural radioactivity was assumed to be in Earth's crust. Therefore, scientists believed that, with increasing height, the ionisation rate should decrease until it disappeared completely. In 1911 and 1912, Victor Hess began measuring the ionisation rate at different altitudes. He found that the ionisation rate initially decreased with increasing height, but then increased significantly at higher heights. By measuring the ionisation rate at various heights and during both night and day, he could prove the extraterrestrial origin of this radiation for the first time. But Hess's measurements were not recognized by the scientific community until his results were confirmed by Werner Kolhörster, who undertook balloon flights up to altitudes of about 9200 m [67]. The nature and origin of this radiation were still unknown. In 1927, Jacob Clay measured the ionisation rate during a sea journey from Java to the Netherlands and observed that the rate of cosmic radiation depends on the geomagnetic field. This shows that cosmic rays are predominantly charged particles rather than photons [47].

In 1932, Carl Anderson discovered antimatter while studying cosmic rays with a cloud chamber [24]. He measured tracks of a particle, which possessed the same mass as the electron but an apparent opposite charge. Other discoveries using cosmic rays include the muon in 1936 and the Pion and Kaon in 1947 [47]. In the years that followed, significant progress was made in the study of cosmic rays. However, many fundamental questions, such as their origin, acceleration mechanisms, and propagation, still remain unanswered.

Cosmic rays can be detected by direct or indirect measurements. Direct measurements with balloons and space-based detectors have the advantage of being able to detect the mass and charge on an event-by-event basis. However, at higher energies, the flux of cosmic rays becomes so low that direct measurements are no longer feasible. Instead, indirect

measurements, which probe the extensive air showers developing in the atmosphere, must be employed. Indirect measurements are typically performed using large arrays of scintillation detectors or water Cherenkov detectors, which record the cascade of secondary charged particles produced in an extensive air shower. Additional detection methods to the surface detector array include air Cherenkov telescopes, fluorescence telescopes or radio antennas. These can provide additional information about the longitudinal profile of cosmic rays. An important approach in current and future cosmic-ray research is multi-messenger astronomy. This method combines information from charged cosmic rays with observations of gamma rays, neutrinos, and gravitational waves to obtain a more detailed understanding of astrophysical processes and to identify possible cosmic-ray sources.

Composition

Cosmic rays consist of about 90% protons, about 9% helium nuclei. The remaining fraction is composed of heavier nuclei and some electrons, positrons and anti-protons. It is believed that the majority of cosmic rays originate from our galaxy. Due to the steeply falling cosmic-ray spectrum, most of the energy above 1 GeV is carried by protons or Helium. The estimated Larmor radius for these particles within a typical magnetic field of the interstellar medium ($\sim \mu$G) is many orders of magnitude smaller than the galactic disk ($\sim 10\,$kpc). Gamma-ray emission at GeV energies is expected to be produced by the decay of neutral pions generated in cosmic-ray interactions with the interstellar medium. Measurements of the gamma ray flux from the Small Magellanic Cloud have shown, that the possibility of a cosmological origin could be ruled out [39].

In Fig. 2.1 the composition of the cosmic rays in comparison to the relative abundance of elements in the solar system is shown. The abundance of the light elements Li, Be and B and the sub-iron elements Sc, Ti, V, Cr and Mn are several orders of magnitude higher than in the solar system. These elements are thought to be produced in spallation process, when cosmic rays with higher nuclear number interact with the interstellar medium. By using the measured difference in elemental abundance, and the cross-sections for spalltion it is possible to estimate the amount of matter traversed by cosmic rays between their creation and observation. Given the density of the galactic disk, it can be inferred that a lower limit on the travelled distance is around 1000 kpc, implying that the cosmic rays stay inside the galactic disk for timescales in the order of Myr. Since this distance is orders of magnitude larger the thickness of the disk $d \approx 0.1\,$kpc, the cosmic rays must propagate in a diffuse motion throughout the galaxy [41].

Spectrum

Cosmic rays cover an extremely wide range of energies from approximately 1 GeV up to 10^{20} eV. The highest-energy cosmic rays exceed by many orders of magnitude the energies achievable with current particle accelerators. This means that cosmic rays enable the study

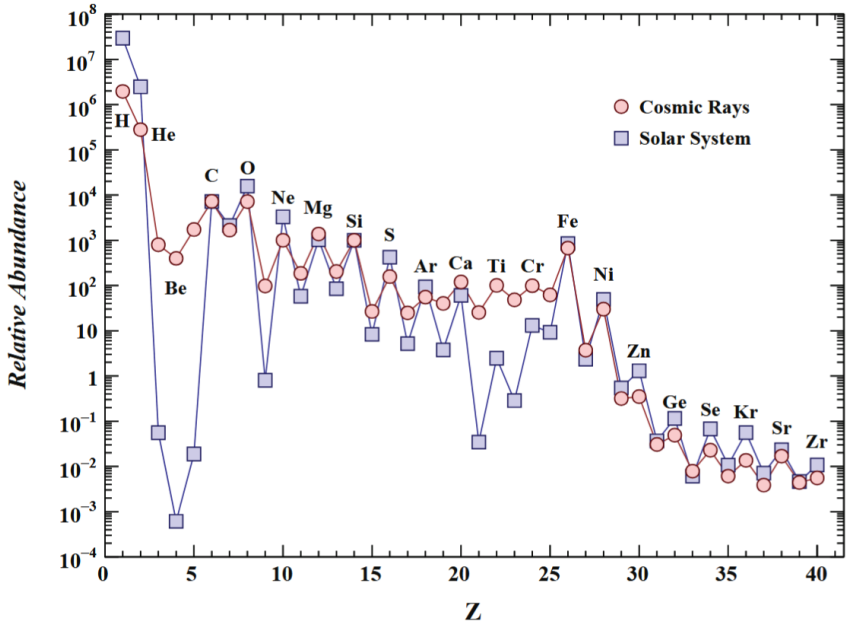

Figure 2.1.: Cosmic-ray elemental abundances compared to those in present-day solar system material. Taken from [46].

of high-energy particle physics and astrophysics. Generally, the spectrum is described by a power law:

$$\frac{dN}{dE} \propto E^{-\gamma}, \tag{2.1}$$

where $\frac{dN}{dE}$ is the cosmic-ray flux per energy given in units of $m^{-2} \cdot s^{-1} \cdot sr^{-1}$. The cosmic-ray spectrum is shown in Fig. 2.2, where the spectrum has been multiplied by E^2 to make the features in the spectrum more visible. The power-law index γ varies with energy at distinct points. The first of these is the knee at $\sim 10^{15}$ eV, where the spectral index changes from $\gamma \sim 2.7$ to $\gamma \sim 3$. A second feature, the second knee, occurs at $\sim 10^{17}$ eV and the ankle at $\sim 10^{19}$ eV. One possible explanation for both knees is that galactic cosmic-ray sources reach their maximum acceleration energy. Because the maximum attainable energy depends on the rigidity, this leads to charge-dependent cutoffs, commonly referred to as the Peters cycle [61]. Therefore, the knee appears first in protons and shifts to heavier nuclei, reaching iron at the highest energies.

The KASCADE experiment observed a knee at approximately 3 PeV in the all-particle energy spectrum, mainly caused by the light components of cosmic rays [25]. An "iron-like" break in the spectrum of the heavy primaries of cosmic rays, as well as in the all-particle energy spectrum, is observed by KASCADE-Grande at around 100 PeV (see Fig. 1.3) [28]. At the same energy, an ankle-like structure, i.e. a remarkable hardening, in the energy spectrum of light components of cosmic rays is observed [27]. At energies above the ankle, the Galactic magnetic field can no longer confine cosmic-ray particles inside the Galaxy. Therefore, their origin must be extragalactic.

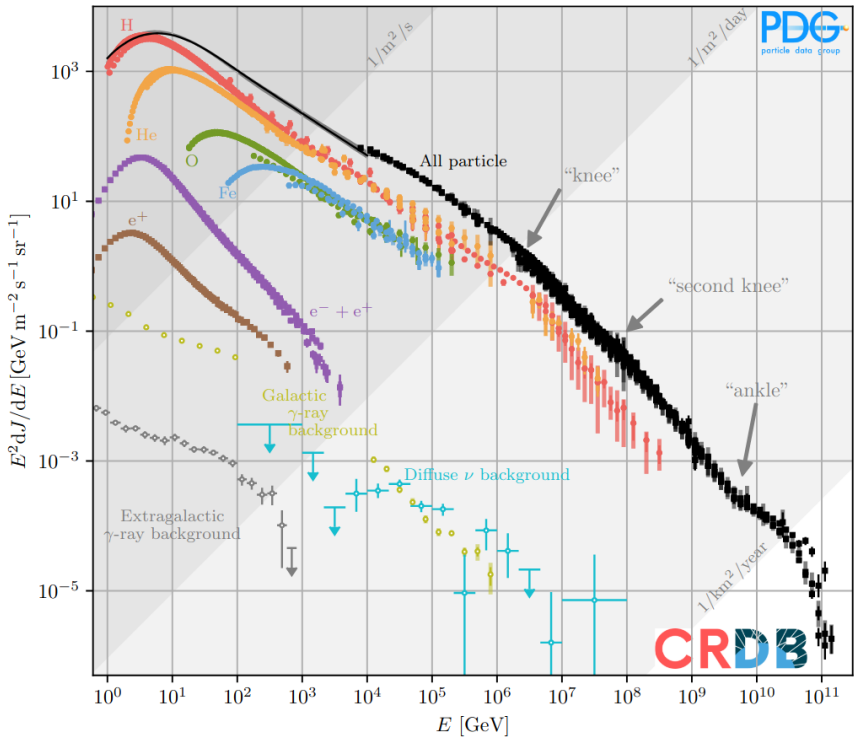

Figure 2.2.: The primary cosmic-ray energy spectrum measured by several experiments. Taken from [59].

At energies of around 10^{20} eV the spectrum falls off steeply. Suggested reasons for this are the maximum acceleration energy of cosmic-ray sources and the GZK effect. The GZK cutoff was independently proposed by Greisen and Zatsepin and Kuzmin in 1966 [72, 45]. It predicts cosmic rays above a threshold energy of $5 \cdot 10^{19}$ eV to interact with the Cosmic Microwave Background (CMB) to produce delta resonances Δ^+. These then decay further into:

$$p + \gamma_{CMB} \rightarrow \Delta^+ \rightarrow p + \pi^0 \tag{2.2}$$

$$p + \gamma_{CMB} \rightarrow \Delta^+ \rightarrow n + \pi^+ \tag{2.3}$$

There is also electron-positron pair production due to the CMB interacting with cosmic rays, but this process only causes a small energy loss. For heavier elements, photo-disintegration occurs at high energies.

2.2. Acceleration

The bulk of galactic cosmic rays is believed to be accelerated by supernova remnants (SNRs). With the typical rate of three type 2 supernovae per century and some assumptions on typical ejecta velocities, the supernovae are ejecting a power of about 10^{42}erg/s into the ISM. If even a few per cent of this energy is converted into cosmic-ray energy, it would still be sufficient to provide the energy for all the galactic cosmic rays [41].

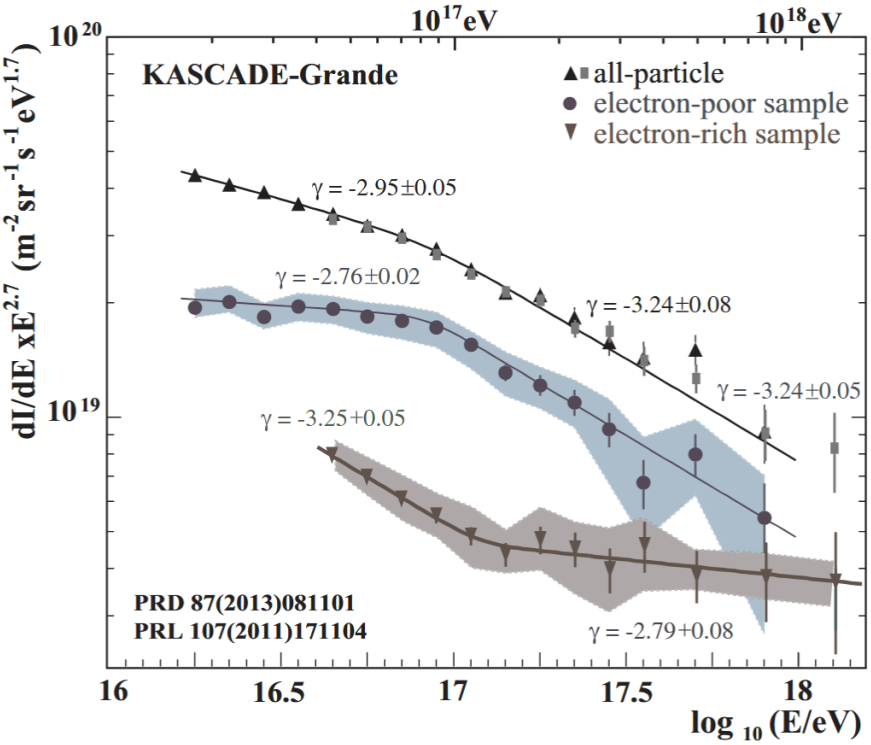

Figure 2.3.: Energy spectra of the electron-poor and electron-rich components with the all-particle spectrum. Taken from [49].

The mechanism of acceleration at supernovae is the Fermi acceleration [41]. There are two types of Fermi acceleration; in the first, the particles come into contact with a moving ionised cloud. In the second, they are accelerated at a moving shock front, as it is the case in SNRs. The supernova shock front moves with velocity $-u_1$ upstream, and the shocked gas behind it follows with a velocity u_2 relative to the front. If the particle moving downstream is overtaken by the shock front, it is diffused by magnetic fields in the downstream gas. This deflection can cause the particle to move upstream and traverse the shock front again. After these two crossings of the shock front, one downstream into the shocked gas and one upstream into the unshocked gas, the particle energy becomes:

$$E_1' = \Gamma^2 E_1 (1 - \beta \cos\theta_1)(1 + \beta \cos\theta_2'), \tag{2.4}$$

where E_1 is the initial energy of the particle before the scattering process and θ_1 and θ_2 are the deflection angles, when entering and exiting the cloud. By averaging over $\cos\theta_1$ and $\cos\theta_2'$ it can be found that the increase in energy after one pair of crossings $\Delta E = \xi \cdot E$ is given with:

$$\xi \sim \frac{4}{3}\beta = \frac{4}{3}\frac{u_1 - u_2}{c}, \tag{2.5}$$

It can be shown, that this Fermi process leads to a power law energy spectrum, which is consistent with the measured power law form of the cosmic-ray spectrum [41].

$$\frac{dN}{dE} \sim (E)^{-\gamma}, \tag{2.6}$$

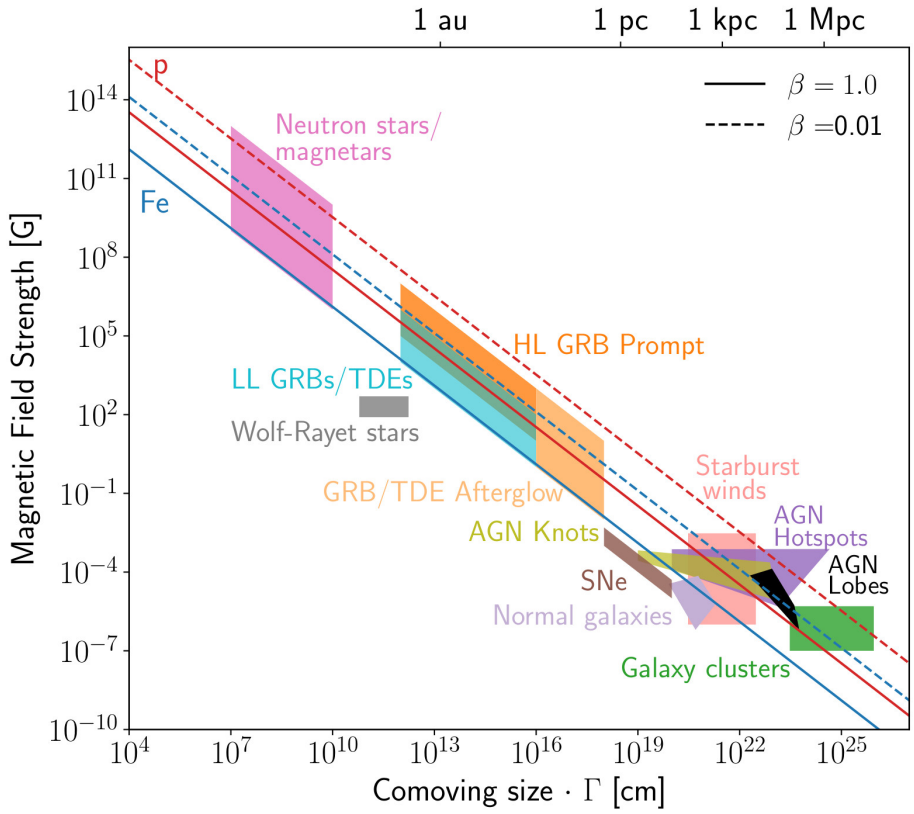

Figure 2.4.: Hillas diagram showing source candidates as a function of their comoving size and their magnetic field strength. The solid (dashed) lines demonstrate the values for the product of the magnetic field B and the radius R to achieve energies of 10^{20} eV for outflows with velocities of $\beta = 1$ ($\beta = 0.01$). Taken from [19].

Hillas formulated a criterion for the maximum energy that a cosmic accelerator can achieve by requiring that the magnetic field of the source be strong enough to confine the particle's trajectory within the acceleration region [54]. If the Larmor radius exceeds the size of this region, the particle will escape before being further accelerated. The resulting maximum energy is therefore given by:

$$E_{max} = q \cdot B \cdot R \tag{2.7}$$

where R is the size of the acceleration region, q is the charge of the particle, and B is the magnetic field of the source. A diagram with possible source candidates as a function of their size and their magnetic field is shown in Fig. 2.4.

2.3. Air showers

The flux at energies around 10^{11} eV is approximately one event per m^2s. At this energy from MeV to TeV, it is possible to study cosmic rays via direct detection, such as satellites or high-altitude balloons. The advantage of direct detection is that the particle species

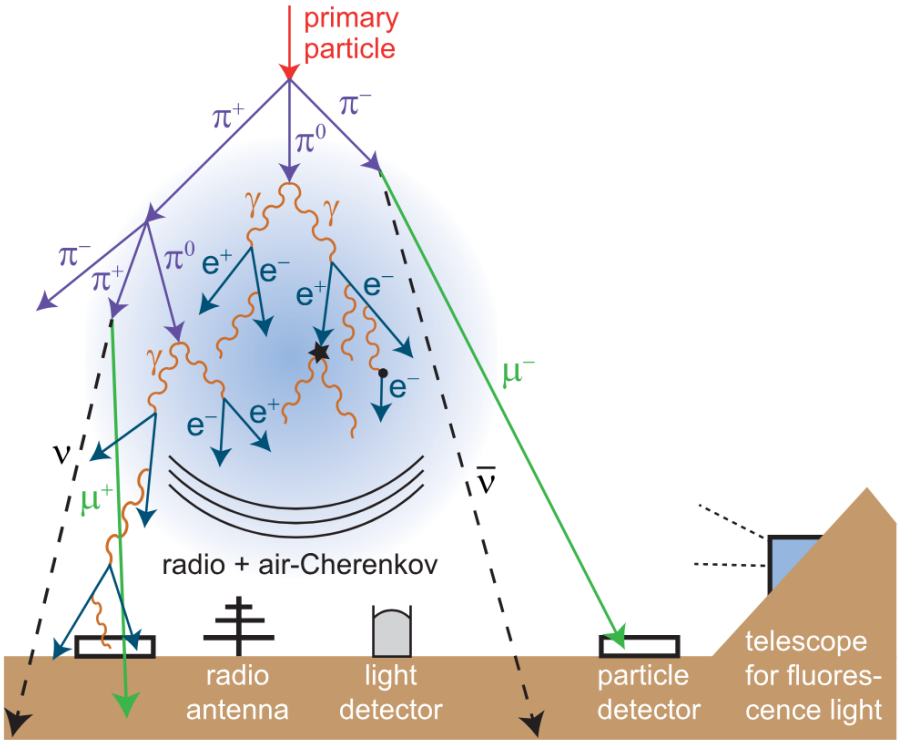

Figure 2.5.: Sketch of an air shower and detection methods [64].

or even the isotope of every reconstructed event can be determined. Because at energies above the knee at approximatlely 10^{15} eV, however, there is less than one event per square meter detection area per year, direct detection is not feasible in this energy range anymore. Cosmic rays can then only be measured indirectly through the measurement of extensive air showers. In this method, only the cascade of secondary particles that is created due to interactions of high-energy cosmic rays in the atmosphere is detected. Fig. 2.5 illustrates the development of an air shower and the associated detection methods.

The air shower consists of electromagnetic, muonic, and hadronic components. The hadronic component generates a shower core that provides photons to electromagnetic showers through the production of neutral pions, which subsequently decay into two photons [41]. Heitler developed a straightforward model to describe the electromagnetic shower produced by photons or electrons. The model assumes that only one particle with energy E_0 is considered at the beginning. After an interaction length X_0 the particles interact and produce two new secondary particles, each with energy $E/2$. Therefore, after every interaction length a new generation n of particles, with the energy

$$E(X) = \frac{E_0}{2^{X/X_0}}, \tag{2.8}$$

is created and the number of particles

$$N(X) = 2^n = 2^{X/X_0} \tag{2.9}$$

is doubled [37]. At an interaction point, an incoming photon leads to pair production, creating an electron and a positron. Positrons and electrons produce a photon via bremsstrahlung. This cascade production is resumed until the energy of the generation reaches the critical energy E_c. This is the energy at which losses due to ionisation are equal to those due to bremsstrahlung. The maximum number of particles in the shower is given as

$$N_{MAX} = \frac{E_0}{E_c} \tag{2.10}$$

and the depth of the shower maximum as [41]

$$X_{max}(E_0) \sim \lambda_e \ln(\frac{E_0}{E_c}). \tag{2.11}$$

Below the critical energy, the ionisation losses dominate and the shower gradually dies out.

Matthews later extended this model to describe hadronic showers. In this case, it is assumed that at every interaction point a number of particles n_{tot} is produced. One third of the particles are neutral pions π^0, which decay almost immediately into two gammas. The remaining two-thirds of the particles are charged pions, which will either interact after an interaction length λ_{int} or if their energy is smaller than the critical energy E_{dec} decay via $\pi^{\pm} \rightarrow \mu^{\pm} + \nu_\mu/\bar{\nu}_\mu$ [41]. Because the decaying neutral pions transfer energy into the electromagnetic component, the portion of energy in the electromagnetic component will increase with each generation, so that after six generations already 90% of the initial energy E_0 has been transferred to the electromagnetic shower [37].

In the superposition model, it is assumed that a nucleus with mass number A and energy E_0 is equivalent to A independent showers with energies E/A. This is motivated by the fact that the binding energy per nucleon with MeV is many orders of magnitude smaller than the interaction energies [37]. In this model, the maximum number of particles $N(X_{max})$ is the same as for proton-induced showers. However, X_{max} becomes smaller and the number of muons in the shower increases. This can be explained by the smaller initial energy per nucleon with which fewer interactions are possible, therefore the shower maximum is reached at a higher altitude in the atmosphere, and less energy is transferred into electromagnetic showers [58]. These differences in the longitudinal profile of different components for iron and proton-induced showers are shown in Fig. 2.6 with the results from CORSIKA Monte Carlo simulations. The longitudinal profile can be measured with air-Cherenkov telescopes, fluorescence telescopes and radio antennas. As previously mentioned, the electromagnetic shower peaks and then dies out once the critical energy threshold is reached. The hadronic component behaves similarly, as it feeds both electromagnetic and muonic components. In contrast, the muonic component attenuates much more slowly because ionisation causes only minor energy losses [51]. Only a small fraction of low-energy muons decay into electrons and neutrinos. These features in the longitudinal development are also depicted in Fig. 2.6.

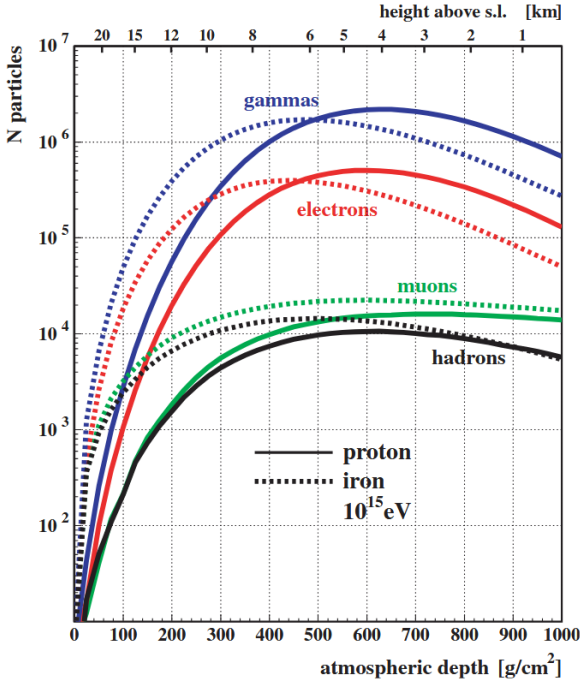

Figure 2.6.: Comparison of longitudinal profiles of secondary particles of iron and proton induced showers. Taken from [51].

2.4. Anisotropy

The cosmic-ray flux arriving at Earth is highly isotropic, as it is expected, since cosmic rays are charged particles and are thus deflected by magnetic fields during propagation. Due to this scattering at magnetic fields, only the small anisotropies can be used to study the propagation and distribution of their sources. But for ultra-high energy cosmic rays (UHECRs) the deflections may be small enough to allow probing the distribution of sources to some extent [35]. A measure of anisotropy is often performed by determining the relative intensity. Generally, the flux of cosmic rays can be expressed in spherical harmonics:

$$\Phi(\boldsymbol{n}) = \sum_{l\geq 0} \sum_{m=-l}^{l} a_{lm} Y_{lm}(\boldsymbol{n}) \tag{2.12}$$

The variations in the relative intensity can be characterized at different angular scales using the multipole moments. But for partial sky coverage, the true multipole moments a_{lm} cannot be recovered, only the pseudo-multipole moments given by:

$$\tilde{a}_{\ell m} = \int \mathrm{d}\mathbf{n}\, \omega(\mathbf{n})\, \Phi(\mathbf{n})\, Y_{\ell m}(\mathbf{n}) \tag{2.13}$$

with the relationship between true and pseudo multipole moments:

$$\tilde{a}_{\ell m} = \sum_{\ell'\geq 0} \sum_{m'=-\ell'}^{\ell'} a_{\ell' m'} \int d\mathbf{n}\, \omega(\mathbf{n})\, Y_{\ell m}(\mathbf{n})\, Y_{\ell' m'}(\mathbf{n}) \tag{2.14}$$

If an upper bound l_{max} is assumed, this equation can be inverted to find the true multipole moments [35]. One reason for the non-isotropy of the arriving cosmic-ray flux is also the Compton-Getting effect. As the Earth moves relative to the rest frame of the cosmic rays, the flux arriving in the direction of Earth's motion increases [34]. This effect can be described by

$$\frac{\Delta I}{I} = (\gamma + 2)\frac{v}{c}\cos\theta, \tag{2.15}$$

where γ is the spectral index, v is the speed of Earths motion and θ is the angle between the arrival direction and the direction of motion. The expected amplitude of this effect is of the order of 10^{-3} [6].

The first analyses of cosmic-ray anisotropies were conducted in the early 1930s. With large air shower arrays and underground muon detectors, it became possible to collect more data and therefore to reduce the statistical and systematic uncertainties [16]. Underground muon detectors are used to measure cosmic rays with energies below 10^{13} eV. For higher energy primaries, the probability of the secondary pions, produced in interactions with the atmosphere, to interact is higher than to decay. Therefore, the number of detectable muons decreases and the statistics for high-energy events are limited. Anisotropy at higher energies can be studied with air shower arrays, which offer the advantage of large detection areas. However, it is difficult to control and to operate an air shower detector to measure anisotropies at a level of 10^{-4}. Because the atmosphere is part of the detector, the acceptance may vary with changes in temperature and pressure. Therefore, the estimation of acceptance and exposure is not achievable with simulations to within 10^{-4} and must be estimated from data instead. However, this estimator may also exhibit artefacts that lead to artificial over- or underdense regions in the resulting relative intensity sky maps [65].

The earliest evidence for periodic intensity variations in the sidereal reference frame was found by Hess and Steinmauer in 1932 [71]. In the last two decades, detectors have achieved enough statistics to probe the anisotropies in the TeV-PeV range at levels of 10^{-4} to 10^{-3}. Examples for such experiments include Tibet ASγ [21], Super-Kamiokande [48], Milagro [10], EAS-TOP [13], ARGO-YBJ [31], HAWC [11], LHAASO [43], IceCube [9], IceTop [5] and KASCADE-Grande [29]. At energies higher than 10 PeV the anisotropy was probed by the Pierre Auger Observatory located in the southern hemisphere [2]. An overview of these results is shown in Fig. 2.7. The amplitudes increase until 10 TeV. After this the amplitudes decreases rapidly to a level of 10^{-4} at 100 TeV and then consistently increases until 10 PeV. The Phase stays approximately stable at 50° up to energies of $\sim$ 300 TeV. At this energy, a phase flip occurs and the phase falls down to about 260°, which is close to the right ascension of the Galactic centre. Overall, the data shows large differences between the results of different experiments. One reason for this could be that air shower arrays don't allow for determining the energy and mass of the primary particle on an event-to-event basis, and therefore could induce uncertainties on the energy and the rigidity dependence of the experiments. The limited field of view (FOV) of experiments leads to interference between large- and mediums-size anisotropies [16].

For isotropic diffusion and stationary sources smoothly distributed in the Galaxy, the resulting dipole vector is expected to point to the galactic centre. The amplitude is believed

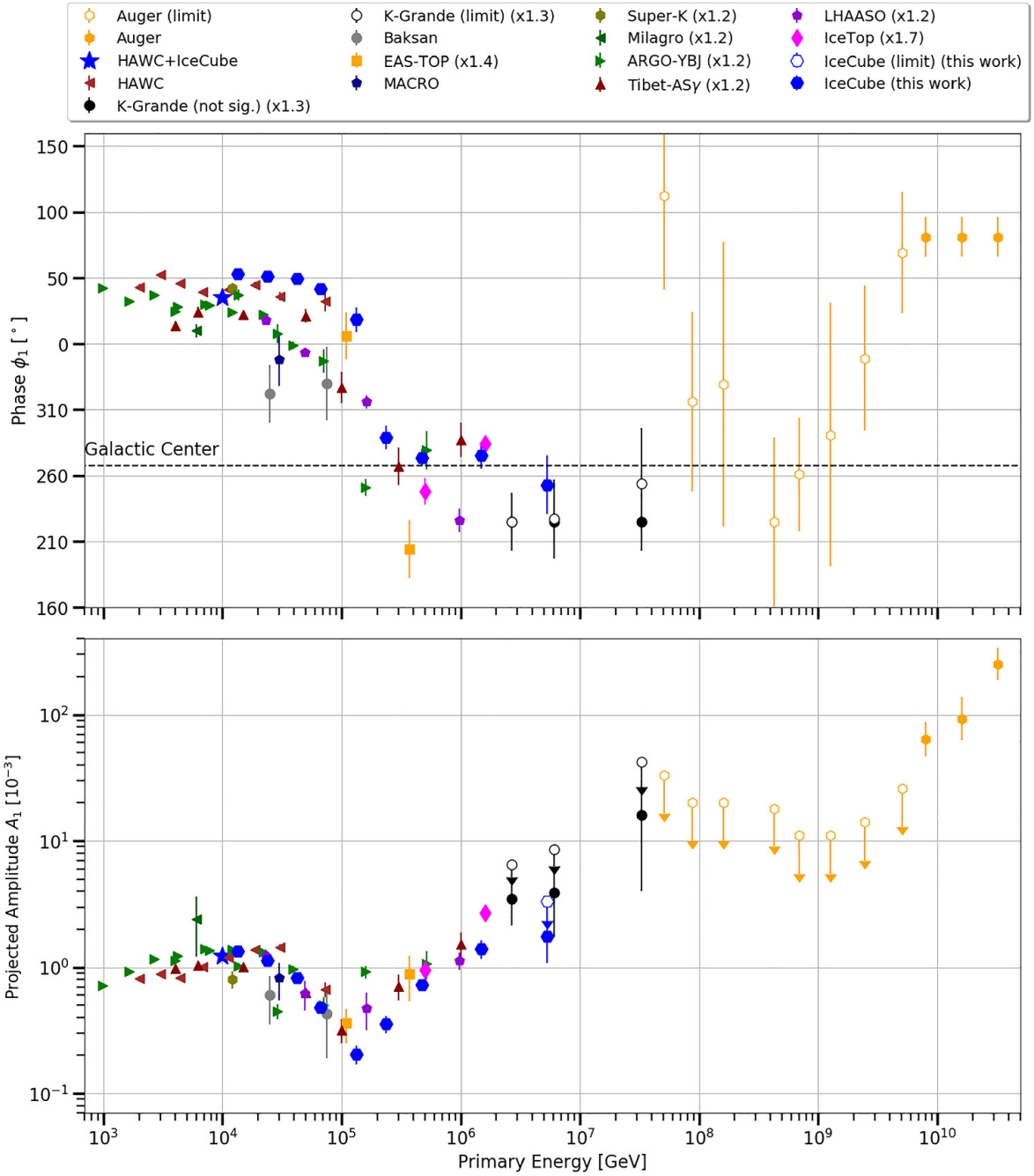

Figure 2.7.: Results for reconstructed phase and amplitude for various experiments. Taken from [9]. The amplitudes for the one-dimensional fits have been corrected for their limited FOV with a location and maximum zenith angle dependent factor: K-Grande [29] $C_{FOV} = 1.34$, EAS-TOP [13] $C_{FOV} = 1.74$, Super-K [48] $C_{FOV} = 1.21$, Milagro [10]$C_{FOV} = 1.21$, ARGO-YBJ [31] $C_{FOV} = 1.18$, Tibet-ASγ [21] $C_{FOV} = 1.18$, LHAASO [43] $C_{FOV} = 1.18$ and IceTop [5] $C_{FOV} = 1.74$. MACRCO [20] and Baksan [18] could not be rescaled due to limited information about their FOV, and the two-dimensional results for HAWC and IceCube and the three-dimensional results for Auger do not require correction.

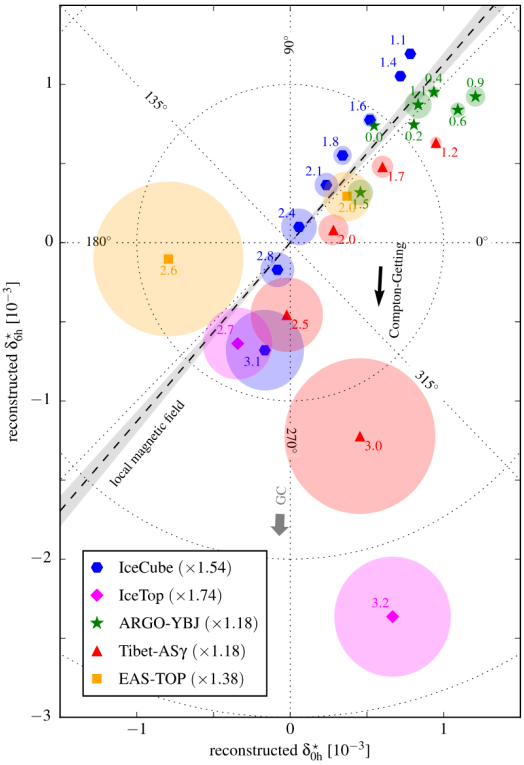

Figure 2.8.: Reconstructed equatorial dipole components in comparison to the local magnetic field (dashed line) measured by IBEX. The amplitudes have been corrected for the FOV, and the Compton-Getting effect has been subtracted. Taken from [16].

to increase with E^{β}, where $\beta \simeq 0.3 - 0.6$ [16, 35]. Since the data do not agree with this simple model for diffusion, a spatially and temporally stochastic distribution of sources might be considered. These fluctuations in the distribution of local sources would then introduce fluctuations in the dipole parameters even if these contributions to the total flux are relatively small. In this scenario, the cosmic-ray distribution would depend on the properties of the local diffusion medium [16]. In Fig. 2.8, the results for the dipole components and the local magnetic field measured with Interstellar Boundary Explorer (IBEX) are shown. The dipole vector is defined as the vector (d_{0h}, d_{6h}), where the components point in the direction of the local sidereal time of 0 h and 6 h, respectively. An alignment of the reconstructed dipole and the local magnetic field direction is observed.

In this thesis the large- and medium scale anisotropies for KASCADE and KASCADE-Grande are estimated. In addition, a qualitative combined analysis with IceTop, KASCADE, and KASCADE-Grande is performed.

3. Analysis Method

In this chapter, the iterative Likelihood method for reconstructing the relative intensity sky map is discussed. A modification of this method, in which the Likelihood is redefined as a pure dipole likelihood and explicitly depends on the dipole components, is shown in Chapter 3.2. After this, an adaptation of the Li & MA significance to this problem is introduced.

3.1. Likelihood method

For simplicity and computational reasons, the sky map will be binned into pixels. This is done with the HEALPix package [44] and its Python implementation, healpy [73]. This is accomplished by defining a parameter as $N_{side} = 64$, which will correspond to a number of pixels $N_{pix} = 49,152$ with an approximate angular diameter of 1°. The anisotropy of cosmic rays is described with the relative intensity, which is calculated with:

$$\delta I = \frac{N_i - \langle N_i \rangle}{\langle N_i \rangle} = I - 1, \tag{3.1}$$

where N_i is the measured number of cosmic rays per pixel in the sky map and $\langle N_i \rangle$ is the background, which is the expected number of events per pixel assuming an isotropic flux. One key problem in all ground-based cosmic-ray anisotropy studies is determining this background. In direct measurements or other areas of particle physics, this is achieved by performing a Monte-Carlo simulation to determine the detector acceptance. For ground-based observatories, where the atmosphere is part of the detector, this is not achievable at a sufficient level to measure anisotropies at the expected magnitude of 10^{-3} to 10^{-4}. Therefore, the data itself is used to estimate the detector exposure and relative intensity. Another aspect is that the distribution of cosmic-ray arrival directions measured by experiments such as KASCADE, KASCADE-Grande and IceTop is inherently non-uniform. This can arise from detector effects, including uneven sky exposure, detector downtime, and variations in detector performance. Subsequently, these detection effects must be corrected for [9]. Notable methods for the estimation of the reference map include the time-scrambling method and direct integration. In both methods, the event rates are integrated with the relative acceptance over a time interval Δt. This leads to an estimate for the number of events expected in the time interval between t and $t + \Delta t$.

In this work, the likelihood-based reconstruction method developed by Ahlers et al. (2016) [17] is used. The likelihood method, as well as the time-scrambling and direct integration

method, assumes that the detector exposure ε accumulated over many sidereal days $\mathcal{E}$ is given as:

$$\mathcal{E}(t, \varphi, \theta) \simeq E(t)A(\varphi, \theta), \tag{3.2}$$

where A is the relative acceptance, which depends on the local coordinates (φ, θ) and is normalised to 1. Therefore, this assumes that the relative acceptance of the detector remains approximately constant over time. And $E(t)$ is the angular-integrated exposure.

This work follows the convention introduced by Ahlers et al. (2016) [17] , where pixels in the local sky map are denoted with roman indices, pixels in the equatorial sky map as fraktur indices and time bins with greek indices. Usually, the reconstructed directions from a detector are reported in the local coordinate system, denoted as (φ, θ) in this work. This coordinate system rotates with the Earth and therefore remains fixed with respect to the detector. The position in the equatorial coordinate system can be described with the right ascension and the declination (α, δ). The equatorial unit vector $\mathbf{n} = (\cos\alpha\cos\delta,\ \sin\alpha\cos\delta,\ \sin\delta)$ can be transformed into the local unit vector $\mathbf{n}' = (\cos\varphi\sin\theta, -\sin\varphi\sin\theta, \cos\theta)$ via:

$$\mathbf{n}' = \mathbf{R}(\mathbf{t})\mathbf{n} \tag{3.3}$$

with

$$\mathbf{R}(\mathbf{t}) = \begin{pmatrix} -\cos(\omega t)\sin\Phi & -\sin(\omega t)\sin\Phi & \cos\Phi \\ \sin(\omega t) & -\cos(\omega t) & 0 \\ \cos(\omega t)\cos\Phi & \sin(\omega t)\cos\Phi & \sin\Phi \end{pmatrix} \tag{3.4}$$

where t is the local sidereal time and $\omega = \frac{2\pi}{24hr}$. Φ is the geographic latitude of the detector and the local sidereal time t is obtained from the Greenwich sidereal time t' with the detector longitude λ:

$$t = t' + \frac{\lambda}{\omega} \tag{3.5}$$

The expected number of cosmic rays per sideral time bin τ and local pixel i is given as:

$$\mu_{\tau_i} \simeq I_{\tau_i} N_\tau A_i \tag{3.6}$$

where I_{τ_i} denotes the relative intensity transformed into the local coordinate system, with the transformation dependent on the sidereal time bin τ. N_τ represents the expected number of background events per sidereal time bin τ, and A_i indicates the acceptance at local pixel i. Assuming that the number of events per pixel is Poisson distributed, μ_{τ_i} can be used to formulate a likelihood to find n events with a hypothesis for I, N, A:

$$\mathcal{L}(n \mid I, N, A) = \prod_{\tau_i} \frac{(\mu_{\tau_i})^{n_{\tau_i}} e^{-\mu_{\tau_i}}}{n_{\tau_i}!} \tag{3.7}$$

Where n_{τ_i} is the number of events in the local pixel i and time bin τ. The best estimates of I, N, A are derived by maximising the likelihood ratio with respect to the null hypothesis, which corresponds to an isotropic flux:

$$\lambda = \frac{\mathcal{L}(n \mid I, N, A)}{\mathcal{L}(n \mid I^{(0)}, N^{(0)}, A^{(0)})} \tag{3.8}$$

Under the assumption of isotropy, the intensity is simply $I_{\mathfrak{a}}^{(0)} = 1$. With the boundary condition $\sum_i A_i = 1$ follows:

$$N_t^{(0)} = \sum_i \mathbf{n}_{\tau i} \tag{3.9}$$

$$A_i^{(0)} = \sum_\tau \mathbf{n}_{\tau i} \Big/ \sum_{\kappa_i} \mathbf{n}_{\kappa i} \tag{3.10}$$

The results for the maximum likelihood are $I^\star$, $N^\star$ and $A^\star$. These must satisfy the following relations:

$$I_a^\star = \frac{\sum_\tau n_{\tau\mathfrak{a}}}{\sum_\kappa A_{\kappa\mathfrak{a}}^\star N_\kappa^\star} \tag{3.11}$$

$$N_\tau^\star = \frac{\sum_i n_{\tau i}}{\sum_j A_j^\star I_{\tau j}^\star} \tag{3.12}$$

$$A_i^\star = \frac{\sum_\tau n_{\tau i}}{\sum_\kappa N_\kappa^\star I_{\kappa i}^\star} \tag{3.13}$$

as well as the normalisation of A and the normalization condition $\sum_\alpha w_\alpha Y_\alpha^{l0} \delta I_\alpha^\star = 0$,which follows from the invariance under declination scaling [17]. Here, w_α is a weight function corresponding to the detector's FOV. This set of nonlinear equations can be solved by an iterative algorithm [17]:

1. First the maximum estimators for isotropy i.e. $I^{(0)} = 1, N^{(0)}, A^{(0)}$ are calculated. For this, the data is binned by sidereal time into 360 bins and stored in a local sky map with a pixel diameter of approximately 1. Therefore, the number of events in the local coordinate system per sidereal time and per pixels are $n_{\tau i}$.
2. Then, the next iteration value of $I^{(n+1)}$ is determined by inserting $N^{(n)}$ and $A^{(n)}$ into Eq. 3.11. For this, the acceptance needs to be transformed into the equatorial coordinate system with the sidereal time dependent transformation function Eq. 3.3 to find $A_{\kappa\mathfrak{a}}^\star$.
3. The anisotropy $\delta I^{(n+1)}$ in the equatorial coordinate system is then expanded into spherical harmonics and the multipole moments $m = 0$ are removed to fulfil the normalisation condition $a_{l0} = 0$ for all l (see [17])
4. Determine $N^{(n+1)}$ with Eq. 3.12 and $I^{(n+1)}, N^{(n)}, A^{(n)}$.
5. Determine $A^{(n+1)}$ with Eq. 3.13 and $I^{(n+1)}, N^{(n+1)}, A^{(n)}$
6. Calculate the renormalisation factor $c = \sum_i A_i^{n+1}$ and normalise the expected number of background events and the acceptance with $A_i^{n+1} \longrightarrow A_i^{n+1}/c$ and $N^{n+1} \longrightarrow N^{n+1}c$
7. This iterative process is repeated until convergence is achieved, defined by a sufficiently small likelihood ratio $2\ln(\lambda^{n+1}/\lambda^n)$. For this work, a maximum of 20 iterations was chosen.

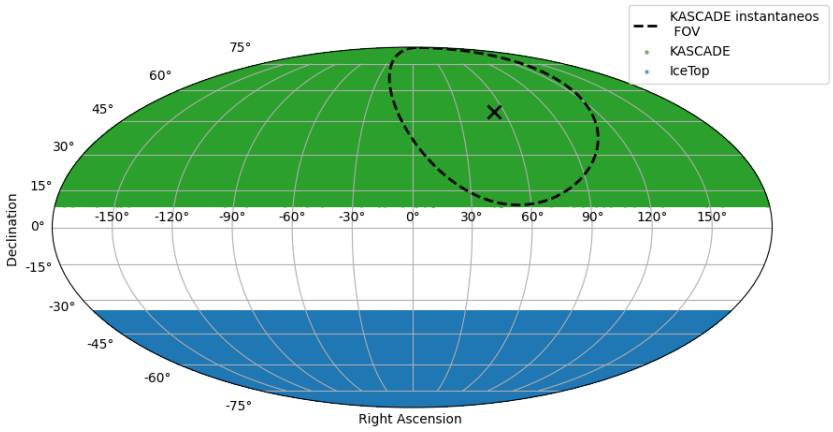

Figure 3.1.: Integrated FOV for KASCADE and KASCADE-Grande with $\theta_{max} = 40°$ at latitude 49.1° and IceTop at latitude −90° and with $\theta_{max} = 55°$ in comparison. The instantaneous FOV of KASCADE and KASCADE-Grande is indicated for a sideral time of 3 h.

Detectors located at mid-latitudes, such as KASCADE and GRANDE, can observe only a limited portion of the sky. In Fig. 3.1 the fields of view of KASCADE and KASCADE-Grande, for a maximum zenith angle of $\theta_{max} = 40°$ in the local coordinate system, are illustrated. Through the rotation of the earth, the time-integrated field of view covers a declination band from $\delta = 9.1°$ to $\delta = 89.1°$. In contrast, since IceTop is located at the South Pole, the time-integrated field of view is equal to the instantaneous field of view (see Fig. 3.1). One advantage of the LLH method is that data from different detectors, with differing FOVs, can be easily combined. However, because the background map is basically calculated by averaging over right ascension, the LLH method is not able to reconstruct anisotropies along Earth's rotation axis. Note that this limitation also applies to the East-West method, as well as to the time-scrambling and direct integration method.

A C^{++} implementation of the analysis method by J. C. Diaz Vélez [66] was used for parts of this work.

3.2. Dipole anisotropy likelihood

The maximum likelihood method for the anisotropy reconstruction mentioned above is used to find estimators for the relative intensity, the detector acceptance and the expected number of events per sidereal time bin. With these results, the background map and anisotropy map can be calculated. When dealing with limited statistics, the likelihood method must be modified to ensure the stability of numerical reconstruction [15]. One approach is a smoothing of the local data maps with a Gaussian smoothing function. Another possibility is to redefine the likelihood to directly incorporate a smoothing scale into the method, as done in Ahlers et al. (2019) [14] for KASCADE-Grande. This is done by expanding the

anisotropy in spherical harmonics Y^{lm} and truncating it at a maximum multipole moment l_{max}:

$$\delta I(\alpha, \delta) = \sum_{\ell \geq 1}^{\ell_{\max}} \sum_{m \neq 0} \hat{a}_{\ell m} \, Y^{\ell m}\left(\tfrac{\pi}{2} - \delta, \alpha\right) \tag{3.14}$$

where $\hat{a}_{\ell m}$ are the true multipole moments. Note that the true multipole moments can be expressed as a superposition of the pseudo multipole moments $a_{\ell m}$. The pseudo multipole moments are defined as in the equation above, but the spherical harmonics function is multiplied by the weight function w_α, which is related to the detectors limited FOV. For a simple dipole fit with $l_{max} = 1$ this simplifies to

$$\delta I_{\text{dipole}}(\alpha, \delta) = d_x \, x(\alpha, \delta) + d_y \, y(\alpha, \delta) \tag{3.15}$$

where $x(\alpha, \delta) = \cos\alpha \cos\delta$ and $y(\alpha, \delta) = \sin\alpha \cos\delta$ are the projections of the previously defined unit vector $\boldsymbol{n}$ onto the equatorial plane. The parameters d_x and d_y are the dipole components belonging to the dipole vector $\vec{d}$. x and y can also be described in terms of spherical harmonics as $x = \sqrt{\frac{2\pi}{3}}\left(Y^{1-1} - Y^{11}\right)$ and $y = i\sqrt{\frac{2\pi}{3}}\left(Y^{1-1} + Y^{11}\right)$. As explained above, the dipole component along the Earth's rotation axis d_z (m=0) cannot be reconstructed with this method. Under the assumption of small anisotropies $\delta I \ll 1$ the truncation at $l_{max} = 1$ leads to a matrix equation [15], which replaces step 2 in the iterative method:

$$\sum_{\tau_i} n_{\tau_i} \begin{pmatrix} x_{\tau_i}^2 & x_{\tau_i} y_{\tau_i} \\ x_{\tau_i} y_{\tau_i} & y_{\tau_i}^2 \end{pmatrix} \begin{pmatrix} d_x^\star \\ d_y^\star \end{pmatrix} \simeq \sum_{\tau_i} \begin{pmatrix} \left(n_{\tau_i} - N_\tau^\star A_i^\star\right) x_{\tau_i} \\ \left(n_{\tau_i} - N_\tau^\star A_i^\star\right) y_{\tau_i} \end{pmatrix} \tag{3.16}$$

One advantage of this method is that the likelihood directly depends on the dipole properties. By maximising the likelihood, it is possible to directly estimate the dipole fit parameters. Therefore, the likelihood ratio, which is given by the likelihood of the dipole divided by the isotropic likelihood, can be used to quantify the uncertainty of the fit results and the general agreement of the data with the dipole hypothesis [15].

$$\lambda = 2 \ln \frac{\mathcal{L}\left(n \mid d_x^\star, d_y^\star, N_\tau^\star, A_i^\star\right)}{\mathcal{L}\left(n \mid 0, 0, N_\tau^{(0)}, A_i^{(0)}\right)} \tag{3.17}$$

The Wilks theorem [68] states that data distributed according to the null hypothesis will cause λ to be distributed according to the χ^2 distribution for a sample size approaching infinity. Therefore, the p-Value, meaning the probability to detect a dipole with this likelihood under the assumption of isotropy i.e. a false positive identification, can be obtained from the χ^2 distribution. As the likelihood for a dipole has two degrees of freedom more than the null hypothesis, the p-value is given by the function:

$$p = e^{-\lambda/2} \tag{3.18}$$

For the dipole likelihood the uncertainties on the dipole components d_x is approximated as

$$\sigma_x^{-2} \simeq \sum_{\tau_i} n_{\tau_i} \left(x_{\tau_i}\right)^2 - \sum_{\tau} \frac{\left(N_\tau^*\right)^2}{\sum_i n_{\tau_i}} \left(\sum_j A_j^* x_{\tau_j}\right)^2 \tag{3.19}$$

and the uncertainty on d_y is obtained analogously [15].

3.3. Significance

To determine the significance for the medium-scale anisotropy, an adaptation of the Li & Ma [56] method, which accounts for time-dependent exposure, similar to [17] is used. For this resulting sky maps are smoothed with a top-hat function (in this work with a smoothing radius of 20°. With this, the sum of measured events and expected events for all pixels within a radius of 20° around the central pixel $\mathfrak{a}$ can be calculated as:

$$\tilde{n}_a = \sum_{\mathfrak{b}\in\mathcal{D}_\mathfrak{a}} \sum_{\tau} n_{\tau\mathfrak{b}}, \tag{3.20}$$

$$\tilde{\mu}_a = \sum_{\mathfrak{b}\in\mathcal{D}_\mathfrak{a}} \sum_{\tau} A^\star_{\tau\mathfrak{b}} N^\star_\tau I^\star_\mathfrak{b}, \tag{3.21}$$

$$\tilde{\mu}^{\mathrm{bg}}_a = \sum_{\mathfrak{b}\in\mathcal{D}_\mathfrak{a}} \sum_{\tau} A^\star_{\tau\mathfrak{b}} N^\star_\tau I^{\mathrm{bg}}_\mathfrak{b}. \tag{3.22}$$

where $\mathcal{D}_\mathfrak{a}$ denotes the set of pixels within the smoothing radius. In general, the background can be chosen for different definitions of the "off-source" events. For example, in small-scale anisotropy analysis, the relative intensity can be expressed as a sum of small- and large-scale components, $I = I_{small} + I_{large}$, where the large-scale component is the skymap for $l \leq 3$.

For the medium-scale analysis performed in this work, the background is defined as isotropic $I^{\mathrm{bg}}_\mathfrak{b} = 1$. Note that in this case the estimators $A^\star_{\tau\mathfrak{b}} N^\star_\tau$ in Eq. 3.22 correspond to $A^0_{\tau\mathfrak{b}} N^0_\tau$ as these are the estimators in case of isotropy. If the relative intensity estimator is not isotropic, the estimators $A^\star_{\tau\mathfrak{b}} N^\star_\tau$ will differ from $A^0_{\tau\mathfrak{b}} \mathcal{N}^0_\tau$ and the significance will be overestimated if they are used in the calculation of $\tilde{\mu}^{\mathrm{bg}}_a$. With this the smoothed anisotropy is given as:

$$\delta\tilde{I}_\mathfrak{a} = \tilde{\mu}_\mathfrak{a} / \tilde{\mu}^{bg}_\mathfrak{a} - 1 \tag{3.23}$$

The corresponding smoothed significance in units of Gaussian standard deviations is then given as:

$$\tilde{S}_\mathfrak{a} = \sqrt{2(-\tilde{\mu}_\mathfrak{a} + \tilde{\mu}^{bg}_\mathfrak{a} + \tilde{n}_\mathfrak{a} \log(1 + \delta\tilde{I}_\mathfrak{a})}} \tag{3.24}$$

This significance is then multiplied by the sign of the relative intensity to indicate excess and deficit regions. Since the maps were smoothed using a top-hat function, the number of independent trials can be approximated as

$$N \simeq \frac{\Delta\Omega_{\mathrm{FOV}}}{\Delta\Omega_{\mathrm{bin}}}, \tag{3.25}$$

where $\Delta\Omega_{\mathrm{FOV}}$ denotes the time-integrated field of view of the detector and $\Delta\Omega_{\mathrm{bin}}$ represents the effective bin size after smoothing [15]. For KASCADE, this yields a trial factor of approximately $N \simeq 14$. The post-trial p-value is then given as:

$$p_{post} \simeq 1 - (1 - p_{pre})^{N_{trial}} \tag{3.26}$$

3.4. Monte Carlo simulations

Simplified Monte Carlo simulations were conducted to evaluate the reconstruction method and quantify the significance of subsequent results. Simplified means that no shower simulations were carried out. Only the event distribution was simulated and analysed with the different methods. Given the expected small anisotropy amplitudes, it is necessary to examine the distribution of reconstructed amplitudes for an isotropic flux, as well as a few examples for a non-horizontal dipole.

Initially, a sky map in local coordinates was reconstructed, with each pixel representing the probability of an event originating from that direction. In the case of an isotropic flux, this probability map is uniform and can be represented by an array of ones. For a non-isotropic flux, the equatorial relative intensity map is:

$$\delta I = d_x \cdot x + d_y \cdot y + d_z \cdot z, \tag{3.27}$$

where d_x, d_y and d_z are the components of the dipole vector and $x = \cos\phi \cdot \cos\delta$, $y = \sin\phi \cdot \cos\delta$ and $z = \sin\delta$. Note that for a non-isotropic flux given as an equatorial sky map, the sky map first has to be transformed via Equation 3.3 to obtain the anisotropy map in local coordinates for every sidereal timestamp. Subsequently, n random pixels are chosen from this probability distribution. To follow the analysis workflow and validate the analysis script, random directions (θ, ϕ) were assigned to each event by sampling uniformly within the selected pixel. However, since the likelihood method works with sky maps binned into pixels, this step is not strictly necessary. For each event, a random sidereal time was also selected. The resulting events were then binned into 360 sidereal-time bins and analysed as described above. Initially, three different three-dimensional dipoles are simulated, and the reconstruction using the dipole LLH method is shown in Fig 3.2. The first example has the dipole vector $d = (0, 0.05, 0.05)$, meaning that the maximum of the dipole is at $(\phi, \delta) = (90°, 45°)$. Since the LLH method can only reconstruct the horizontal component of this dipole, the reconstructed dipole has only the horizontal amplitude, i.e., 0.05, and a maximum at $\phi = 90°$. In the second scenario, a dipole with only a vertical component $d = (0, 0, 0.05)$ was simulated. The horizontal dipole is therefore only an isotropic distribution, which leads to the reconstruction of a small amplitude of $1.5 \cdot 10^{-4}$ and a high p-value. In the final example, a dipole with $d = (0.05, 0, -0.05)$, where the maximum of the relative intensity lies outside of the FOV, was simulated. Again, the reconstructed dipole matches the expected horizontal component.

Subsequently, isotropic distributions were simulated 10 000 times, and the dipole fit was performed with the one-dimensional (1D) method. The reconstructed amplitudes, corrected for the FOV and phases, are shown in Fig. 3.3 for $N_{Events} = 10^8$ events. The resulting mean amplitude and the amplitudes corresponding to the 0.95 and 0.997 p-values are shown in the top-right corner. The phases are, as expected, uniformly distributed. Note that these simulations assume the best-case measurement scenario, with no reconstruction error and a detector acceptance represented as a uniform sky map of ones. Therefore, it does not change with time or season, unlike the true atmosphere-dependent acceptance. Additionally, no Compton-Getting effect was simulated, so no interference between different reference

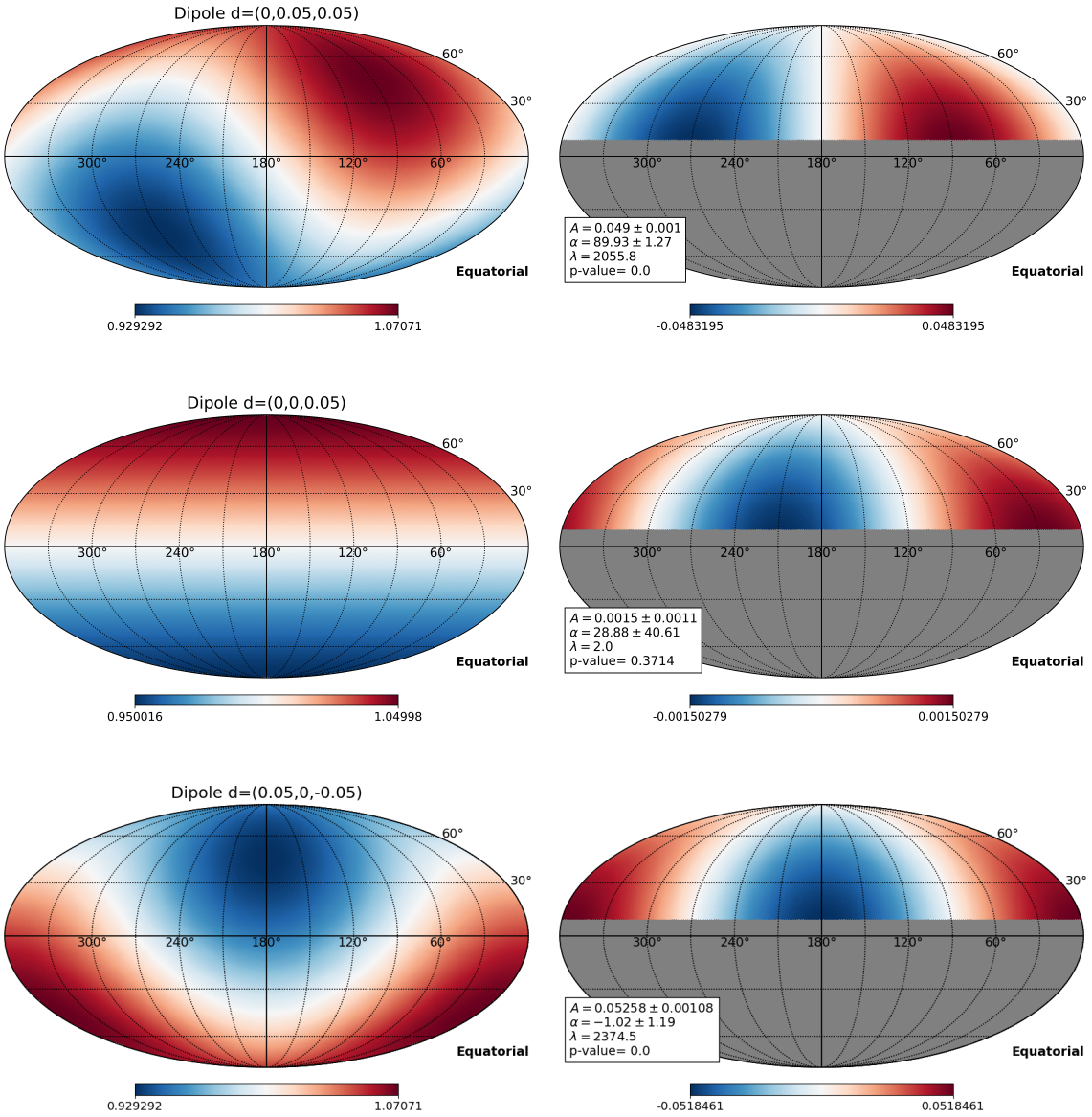

Figure 3.2.: Toy Monte Carlo simulation of three dipoles with various amplitudes and phases. Left: Simulated dipole anisotropy determined with Eq. 3.27. Right: Reconstructed dipole.

frames can introduce an anisotropy. With this baseline study of the analysis method, the best-case significance can be estimated. If the resulting amplitudes for KASCADE or KASCADE-Grande are not significant in this idealised simulation, then they cannot be considered significant in a realistic scenario that includes various systematic effects. The Li & Ma significance maps were also calculated, and the resulting maximum pre-trial and post-trial significance is shown in Fig. 3.6. For the determination of the post-trial significance, the pre-trial significance was corrected for the number of trials, as described in the previous chapter. Since the maximum of this post-trial distribution is about 2.5 Gaussian σ, the standard method for estimating the number of trials appears to be an underestimation.

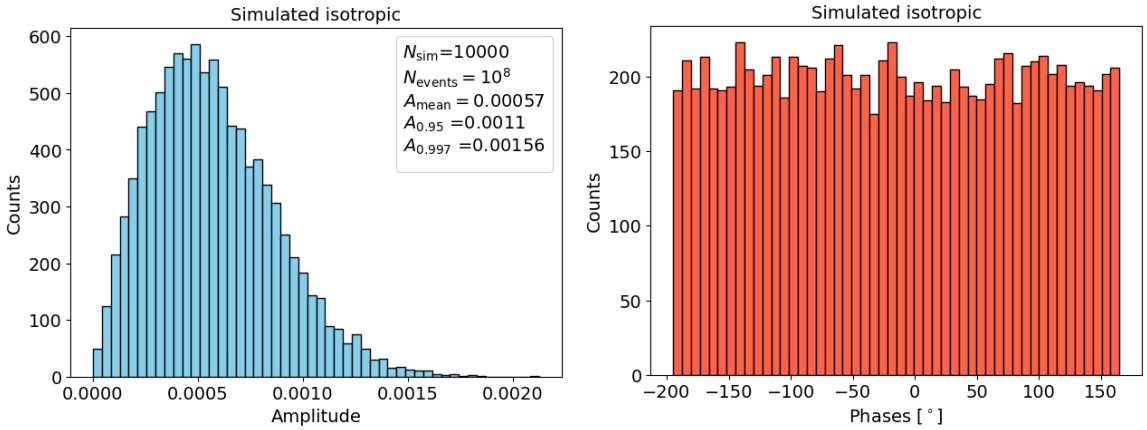

Figure 3.3.: Toy Monte Carlo simulations for KASCADE with $N_{Events} = 10^8$. Left: Resulting dipole amplitudes. The amplitudes corresponding to the mean result and the 0.95 and 0.997 p-values are indicated in the top-right corner. Right: Distribution of reconstructed phases.

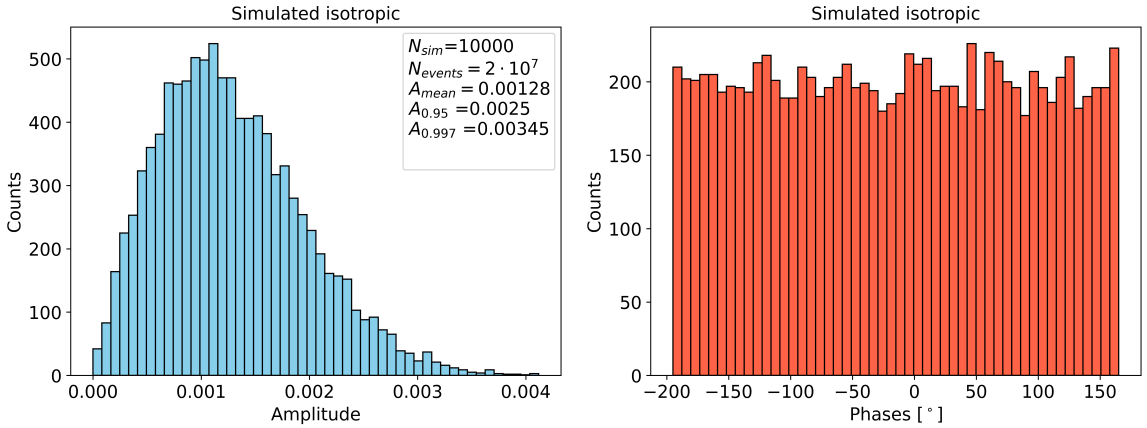

Figure 3.4.: Toy Monte Carlo Simulations for KASCADE with $N_{Events} = 2 \cdot 10^7$. Left: Resulting dipole amplitudes. The amplitudes corresponding to the mean result and the 0.95 and 0.997 p-values are indicated in the top-right corner. Right: Distribution of reconstructed phases.

Note that the simulation uses only the detector location and the maximum zenith angle and therefore the results can be applied to KASCADE and KASCADE-Grande. The simulation was repeated with $N_{Events} = 2 \cdot 10^7$ (Fig. 3.4) and $N_{Events} = 6 \cdot 10^6$ (Fig. 3.5), in order to quantify the impact of statistical fluctuations on the reconstructed dipole amplitude and phase, as well as to evaluate the statistical significance of the analysis. As the reconstructed dipole is only due to statistical fluctuations, the mean amplitude increases with decreasing event count.

To assess whether multiple time gaps could affect this idealised scenario, the simulations were repeated, and the time events were sampled from a distribution representing the detector's uptime (see Fig. 4.3). The resulting amplitudes and phases are shown in Fig. 3.7. The distributions of amplitude and phase are similar to the result in Fig. 4.22, as expected, because the LLH method assumes a time-dependent exposure $\mathcal{E}(t)$.

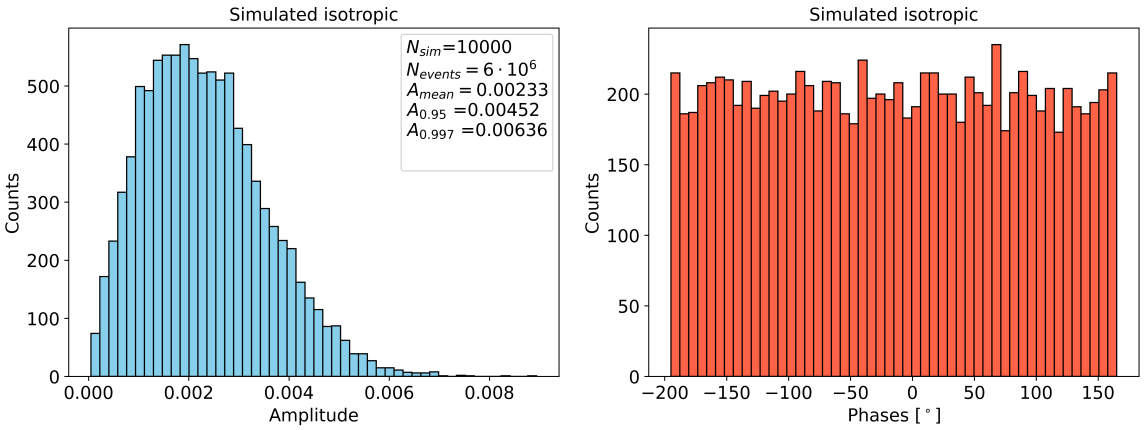

Figure 3.5.: Toy Monte Carlo simulations for KASCADE with $N_{Events} = 2 \cdot 10^6$. Left: Resulting dipole amplitudes. The amplitudes corresponding to the mean result and the 0.95 and 0.997 p-values are indicated in the top-right corner. Right: Distribution of reconstructed phases.

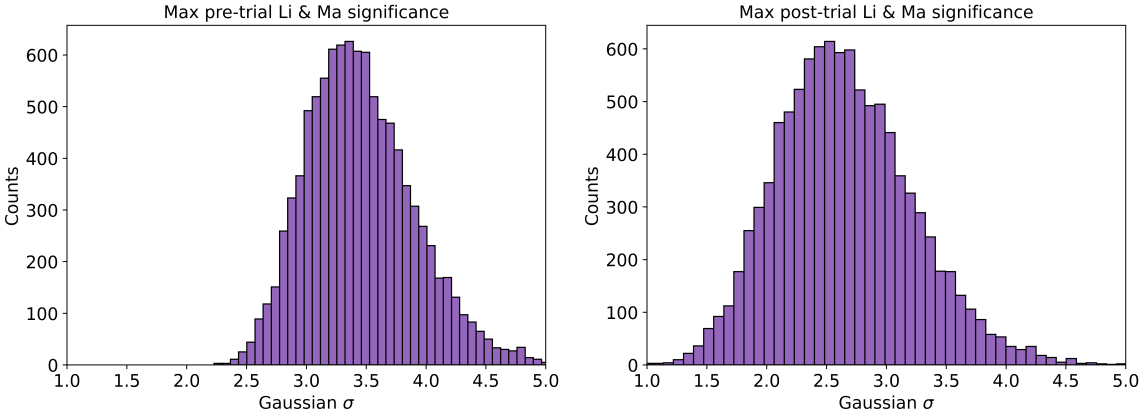

Figure 3.6.: Distribution of the maximum pre- and post-trial Li & Ma for Toy Monte Carlo Simulations with $N_{Events} = 10^8$.

The isotropic simulation for $N_{Events} = 10^8$ was repeated using the reconstruction of the dipole LLH method. This allows a comparison of the results obtained with the one-dimensional method and it also provides the distribution of the likelihood ratios, enabling the verification of the estimated p-value. The resulting distribution of the reconstructed amplitudes and the distribution of the likelihood ratio λ are shown in Fig. 3.8. The distribution of λ seems to follow the expected Chi-squared distribution and is used in the following chapters to cross-check the significance of the reconstructed results.

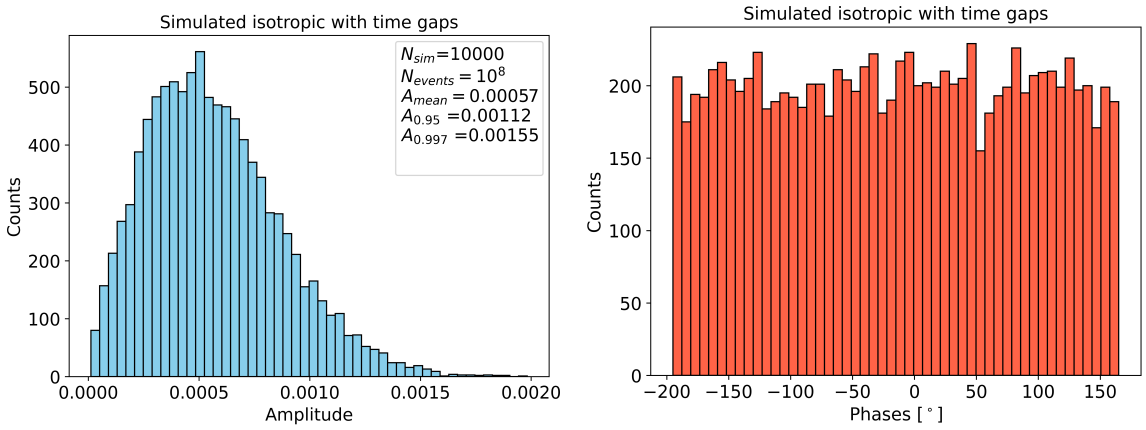

Figure 3.7.: Toy Monte Carlo Simulations for KASCADE with event times sampled from detector uptime distribution. Left: Resulting dipole amplitudes. The amplitudes corresponding to the mean result and the 0.95 and 0.997 p-values are indicated in the top-right corner. Right: Distribution of reconstructed phases.

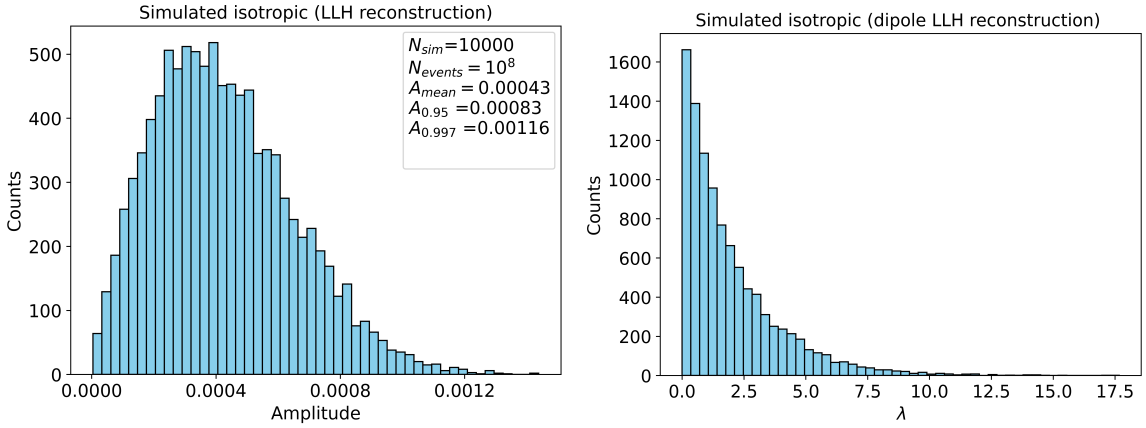

Figure 3.8.: Pure dipole LLH reconstruction for istoropic flux. Left: Resulting dipole amplitudes. Right: Distribution of reconstructed likelihood ratio λ.

4. Analysis of KASCADE data

4.1. KASCADE detector

The KASCADE (KArlsruhe Shower Core and Array DEtector) is an air-shower detector designed to investigate cosmic rays at energies from 10^{14} eV to 10^{17} eV around the knee region. It was located in Karlsruhe at latitude of 49.1°, a longitude of 8.4° and altitude approximately 110 m above sea level at the Campus North of KIT. The detector comprises three main components: the electromagnetic detector, consisting of an array of scintillation counters, the muonic detector component, using scintillators and tracking chambers and the hadronic component, with a sampling calorimeter located at the centre of the detector array. The array covers an area of 200 x 200 m^2 [26]. The measurement period ran from 1996 to 2013. A schematic layout of the KASCADE detector is shown in Fig. 4.1.

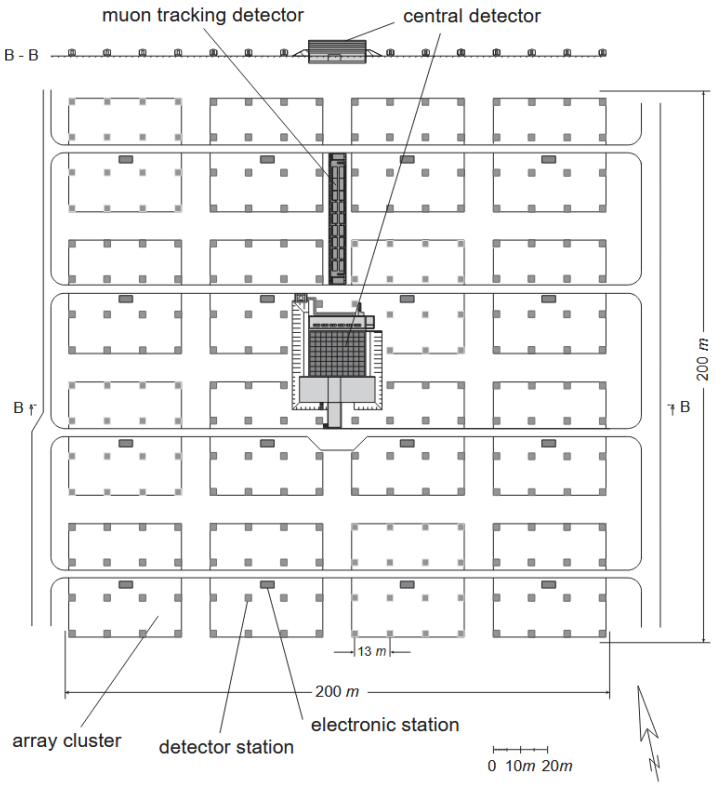

Figure 4.1.: Layout of the KASCADE detector. Taken from [26].

The central detector is composed of eight layers of absorbers made of lead, iron, and concrete, arranged alternately with nine layers of liquid ionisation chambers [26]. An additional layer of plastic scintillators, serving as a trigger, is located within the top layers. Under the calorimeter are two additional layers of multi-wire proportional chambers and a layer of streamer tubes to measure high-energy muons. Above the calorimeter is the top trigger cluster, which collects information on the electromagnetic component. The thickness of the calorimeter relates to 11.5 nuclear interaction lengths in the vertical direction. The hadronic calorimeter is primarily used to distinguish nuclei of different masses, as heavier nuclei initiate cascades with fewer hadrons [38]. In this analysis, no data from the calorimeter were used.

The second part of the detector is the muon detector system. The muon tracking detector measured muon tracks by reconstructing their positions using three horizontal layers of streamer tubes and additional vertical detector modules on the sides. This detector component was installed underground beneath an absorber layer composed of concrete, iron, and soil. Its primary purpose was to reconstruct the muon tracks and to use them primarily for the reconstruction of the muon production heights [26].

The third component is the detector array, which consisted of 252 detector stations arranged on a rectangular grid with a spacing between the stations of 13 m. The array is organised in 16 clusters (see Fig. 4.1) and each station collected data independently. There are two types of detector stations. The inner detector stations consist of 4 liquid scintillators. The liquid scintillator was filled into a circular tub with a diameter of 1 m and a height of 5 cm, and a light-collection cone with a PMT was placed on top of the liquid scintillator. The outer stations were only equipped with two liquid scintillation detectors, but also included an additional plastic scintillator for muon detection, located beneath an iron and lead absorption layer [26]. The electromagnetic and muonic components ($E_\mu > 230$ MeV) were measured by unshielded liquid scintillators and shielded plastic scintillators, respectively. This detector setup enables to reconstruct the number of muons and electrons separately on an event-by-event basis. A schematic of an outer detector station is shown in Fig. 4.2. Only data from the array were used in this analysis.

One of the main goals and results of the KASCADE experiment was the observation of the knee feature at around 3-4 PeV in the cosmic-ray energy spectrum. Another primary objective was to examine and fine-tune hadronic interaction models by studying correlations between the central detector and the air-shower array [1]. By analysing all data, it was shown that the knee is caused by a decrease in light primaries rather than a decrease in medium and heavy primaries. This has been determined by unfolding the spectrum for different primaries (H, He, C, Si, and Fe) using simulations. These results depend on the hadronic interaction model, but a general trend towards heavier mass composition after the knee could be found independently of the interaction model [1].

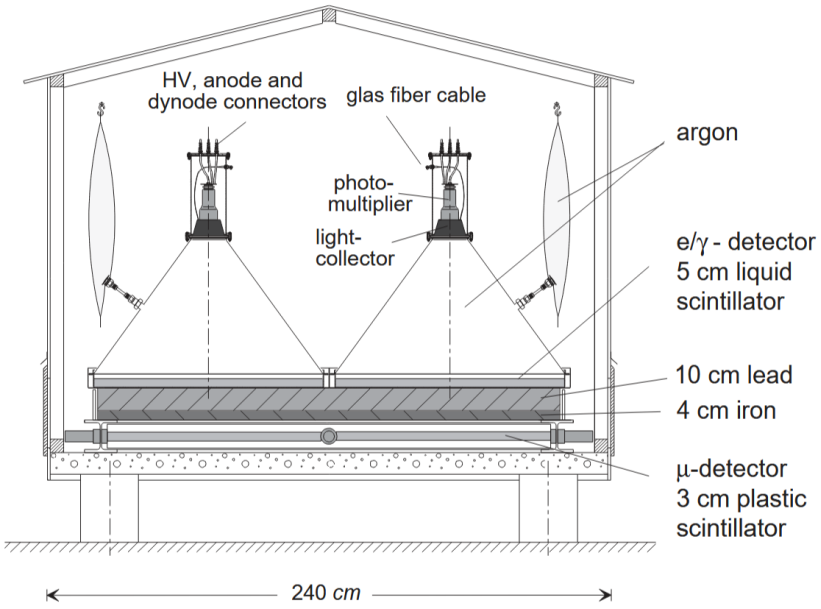

Figure 4.2.: Schematic view of KASCADE array station setup. Taken from [26].

4.2. Large and medium scale anisotropy

To date, only one anisotropy study of KASCADE data has been performed by G. Maier [57] covering data up to October 2002. This work aims to analyse the full KASCADE dataset using the iterative likelihood method. All data and simulations for this analysis were obtained from the KASCADE Cosmic Ray Data Centre (KCDC) [50]. For KASCADE and KASCADE-Grande, the combined number of events is around 1.7 billion, of which 433 million survived the quality cuts and are available for the public. The available dataset covers the period from April 1998 to January 2013. In Fig. 4.3 the event counts per day over time are shown. Although the recorded zenith angles range from 0° to 60°, only events with zenith angles lower than 40° were considered to ensure an accurate shower reconstruction. For KASCADE, the primary energy is estimated using the measured numbers of electrons N_e and muons N_μ and is calculated with [69]:

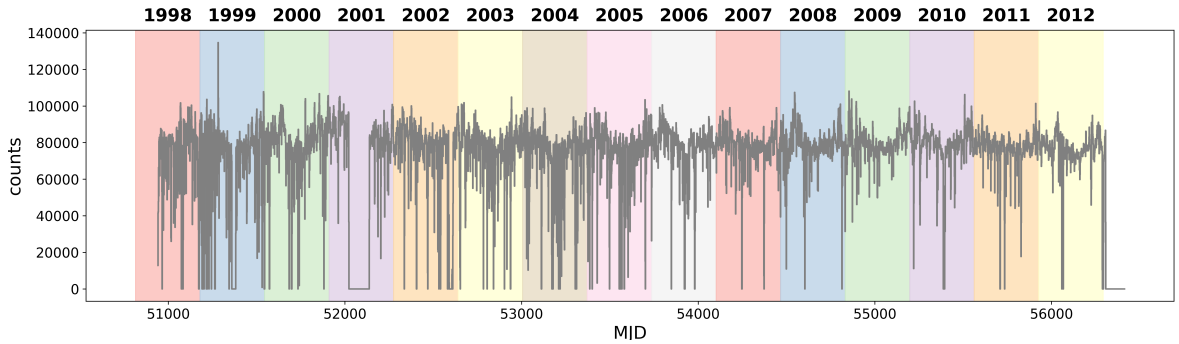

Figure 4.3.: KASCADE events over measurement time per Modified Julian Date (MJD)

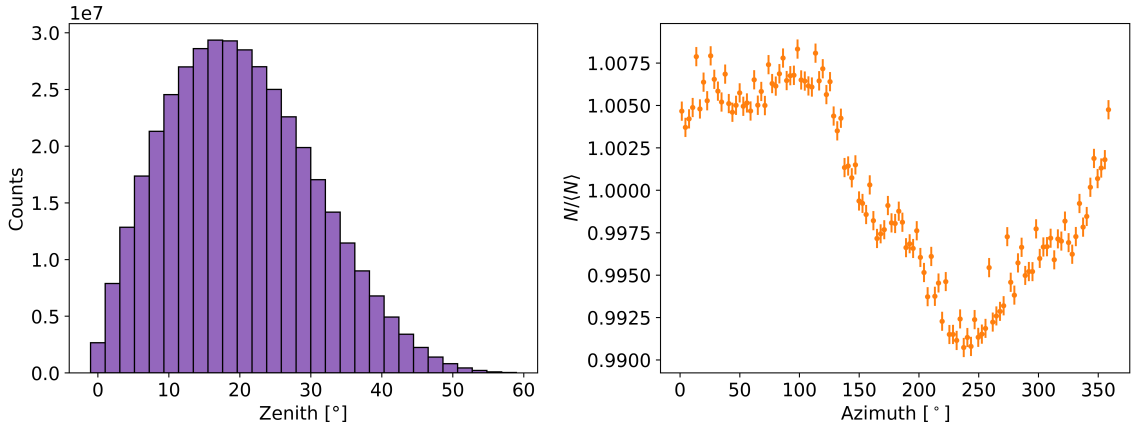

Figure 4.4.: Left: Distribution of zenith angles. Right: relative counts over azimuth angle ($\theta \leq 40$).

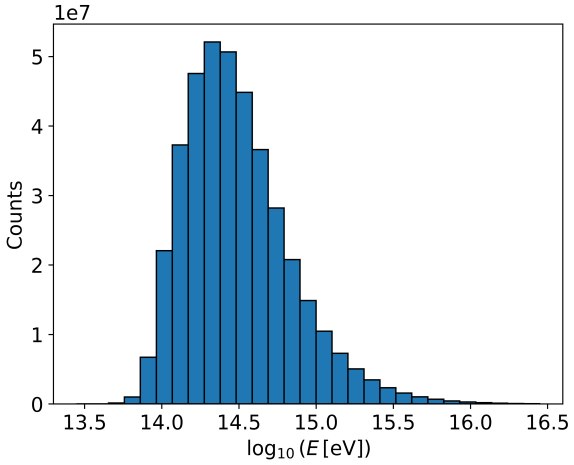

Figure 4.5.: KASCADE energy distribution.

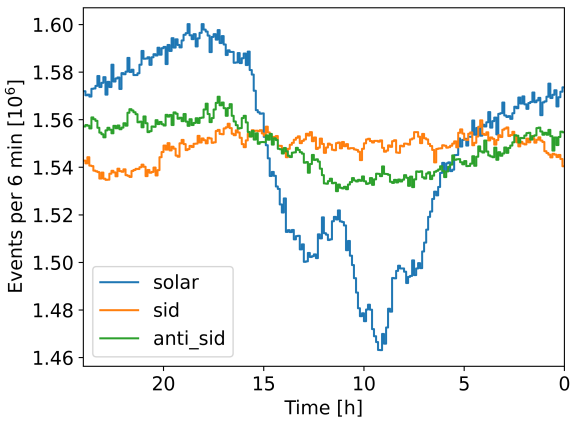

Figure 4.6.: Distribution of KASCADE events over time in different reference frames.

$$\log(E/eV) = 1.93499 + 0.25788 \cdot \log(N_e) + 0.66704 \cdot \log(N_\mu) + 0.07507 \cdot \log(N_e)^2 + 0.09277 \cdot \log(N_\mu)^2 - 0.16131 \cdot \log(N_e) \cdot \log(N_\mu) \quad (4.1)$$

The energy distribution is shown in Fig. 4.5, while Fig. 4.4 displays the distributions of the zenith and azimuth angles. A non-isotropic azimuthal distribution with a maximum deviation of about ±1% is observed, primarily due to detector site effects and the influence of the Earth's magnetic field. Nevertheless, this does not bias the anisotropy analysis, as the ϕ- and θ-dependent detector acceptance $A(\phi, \theta)$ is estimated by the likelihood method, which therefore accounts for a non-isotropic azimuthal distribution. The distribution of KASCADE events over time in sidereal, solar and anti-sidereal reference frames is presented in Fig. 4.6 to illustrate the variation of rates over a solar day and in non-physical reference frames. These variations and possible resulting systematic effects through interference are further discussed in the next chapter. The data were obtained from the KCDC Data Shop selection tool. The quality cuts automatically applied to the data by KCDC are [69]:

1. Successful reconstruction in all steps
2. The KASCADE array produced a trigger signal
3. A maximum of two array clusters are missing
4. The reconstructed shower core is within a radius of 91 m around the center of the KASCADE array.
5. The AGE parameter of the lateral shower shape fit is restricted in the range 0.1 < AGE < 1.48
6. The reconstructed zenith angle is smaller than 60°
7. The number of electrons measured needs to be $N_e > 100$
8. The number of muons measured needs to be $N_\mu > 100$

The only additional quality cut applied in this analysis was a maximum zenith angle of 40° and a minimum estimated energy of 10^{14} eV. The energy estimator is used to bin the data into four distinct energy bins. The specific energy cuts, the resulting median energies and the number of events per bin are presented in Table 4.1. The likelihood-based reconstruction was then applied to each energy bin. The LLH method returns estimators for A, N, and I. The anisotropy is then determined with the number of events per pixel i.e., the data $d_\mathfrak{a} = \sum_\tau n_{\tau\mathfrak{a}}$ and the reference map $b_\mathfrak{a} = \sum_\kappa A_{\kappa\mathfrak{a}} \cdot N_\kappa$ both in the equatorial coordinate system. Figure 4.7 presents the outputs for an exemplary run of the lowest energy bin, including the unsmoothed data, background, and exposure, to illustrate the results of the likelihood method. To determine the smoothed anisotropy map, both the data and background maps are smoothed with a top-hat function and a smoothing radius of 20°. With these smoothed values $\tilde{d}_\mathfrak{a}$ and $\tilde{b}_\mathfrak{a}$ the smoothed anisotropy map is calculated as:

$$\delta\tilde{I}_\mathfrak{a} = \tilde{d}_\mathfrak{a}/\tilde{b}_\mathfrak{a} - 1 \quad (4.2)$$

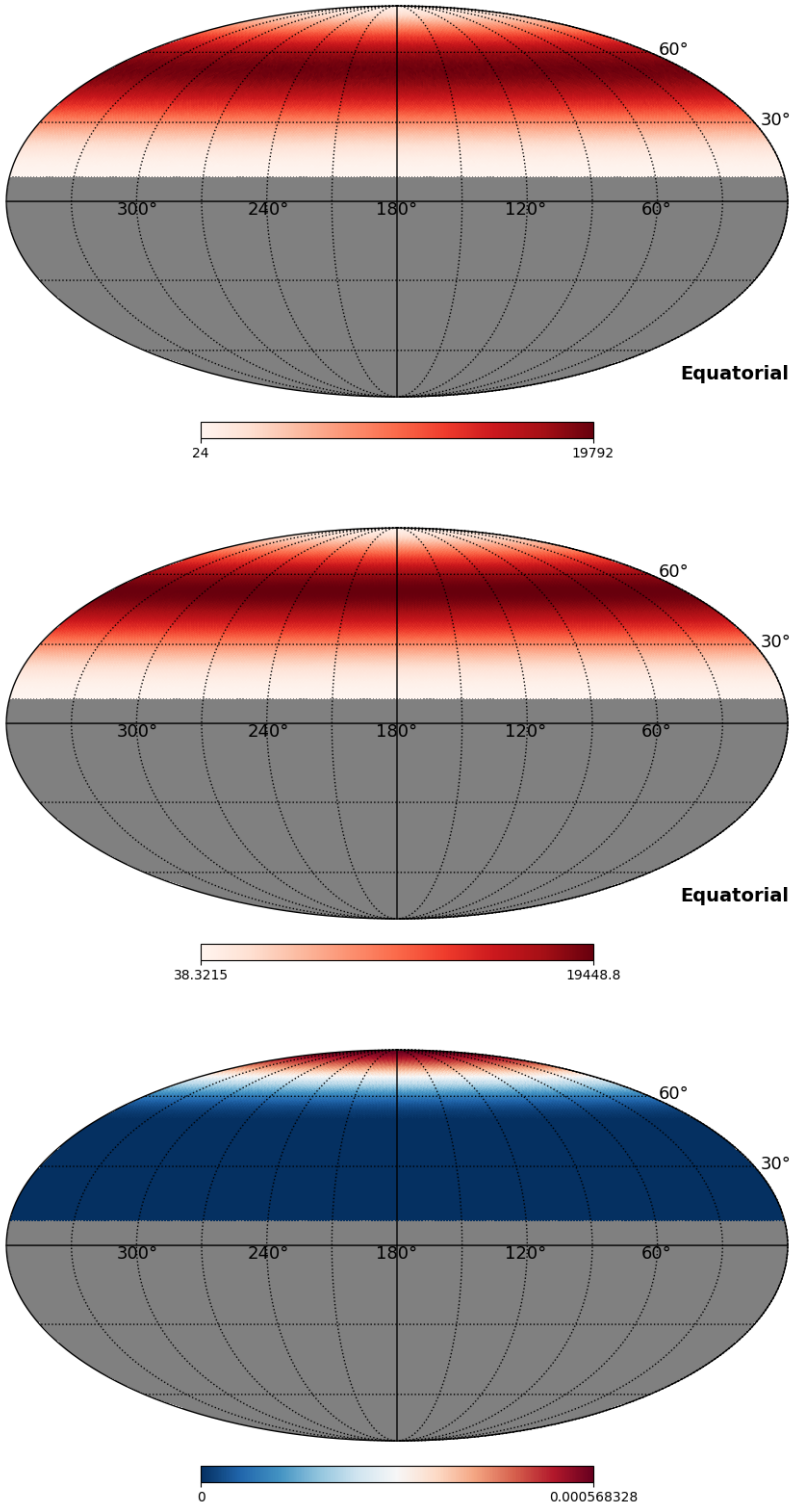

Figure 4.7.: Examplary outputs for the likelihood-based anisotropy reconstruction method of energy bin 1 of KASCADE. Top: A combined map of all events in this energy bin $d_\mathfrak{a}$ in the equatorial coordinate system. Middle: estimated background $b_\mathfrak{a}$ in equatorial coordinates. Bottom: the estimated detector acceptance in local coordinates.

	energy range	E_{med} [TeV]	N [10^6]
bin 1	$[10^{14}, 10^{14.5})$	180	194.70
bin 2	$[10^{14.5}, 10^{15})$	439	147.05
bin 3	$[10^{15}, 10^{15.5})$	1374	26.48
bin 4	$[10^{15.5}, 10^{16})$	4248	3.12
complete data	$[10^{14}, 10^{16})$	225	371

Table 4.1.: Four different energy ranges of KASCADE data, along with the median energy and the number of events for each energy bin.

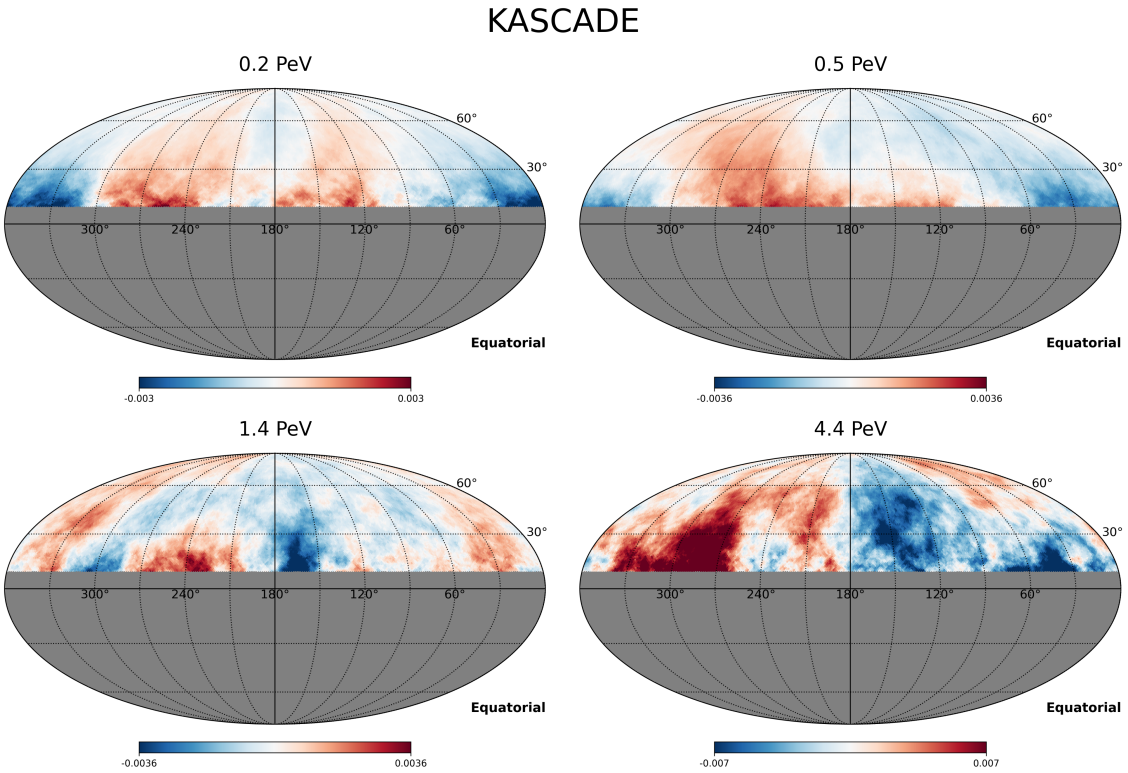

Figure 4.8.: Smoothed sky maps of the reconstructed anisotropy for KASCADE.

The resulting sky maps are shown in Fig. 4.8, where pixels outside the field of view are shown as grey.

To describe the significance of the medium-scale anisotropy, a generalisation of the Li & Ma significance [56] similar to Ahlers et al. [17] was performed. A detailed description of this method is provided in Chapter 3.3. The resulting smoothed pre-trial significance maps, along with the resulting maximum absolute value of the pre-trial significance, are shown in Fig. 4.9. Note that the absolute value of the significance is dependent on the smoothing radius. However, it is fixed to 20° in this work. This pre-trial significance has to be accounted for the number of trials. Since the maps were smoothed with a top hat function, the number of trials can be estimated as $N_{trial} \simeq \Delta\Omega_{FOV}/\Delta\Omega_{bin}$ with the size of the detector's time

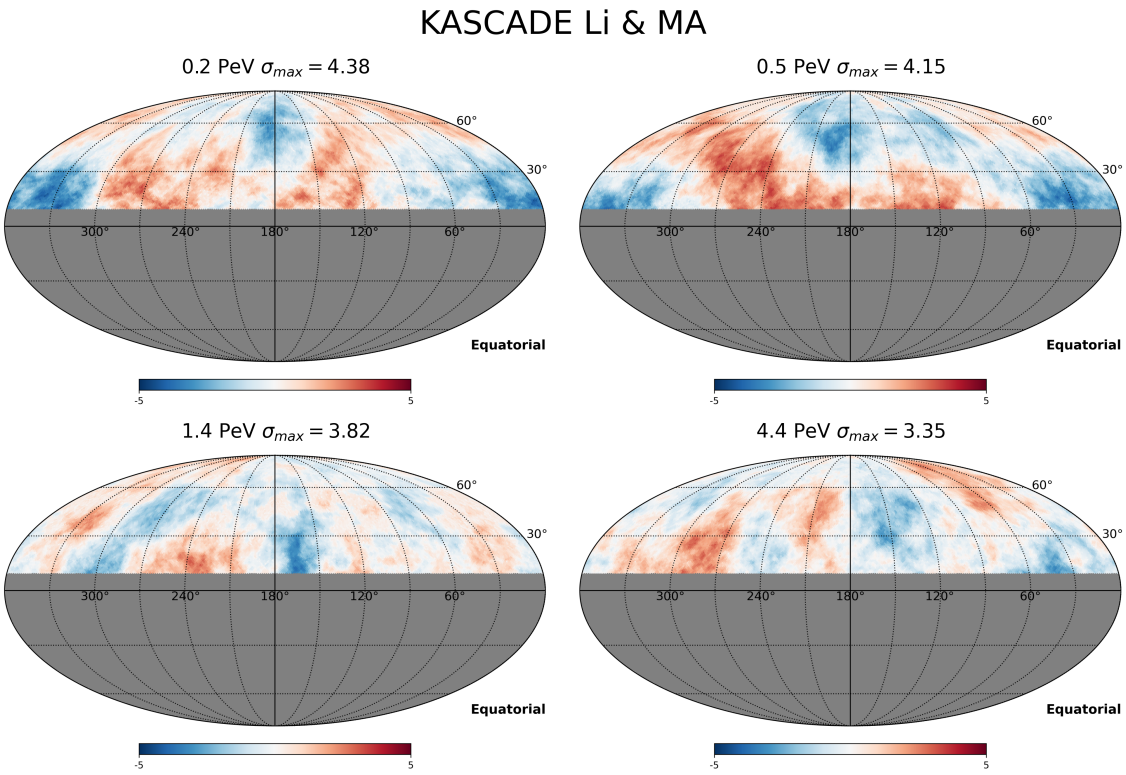

Figure 4.9.: Smoothed sky maps of the reconstructed pre-trial Li & Ma significance for KASCADE. The maximum absolute pre-trial significance is indicated above the corresponding sky map.

integrated field of view $\Delta\Omega_{FOV}$ and the effective bin size after smoothing $\Delta\Omega_{bin}$ [15]. For KASCADE the trial factor is $N \simeq 14$. After the estimation of the anisotropy, a dipole is fitted to the sky map. Several methods can be employed for this purpose. One approach involves the projection of the anisotropy on to right-ascension, meaning calculating the declination average over a right-ascension bin. This is equal to the calculation of [16]:

$$\tilde{A}_1 e^{i\tilde{a}_1} = \frac{1}{\pi} \int_0^{2\pi} d\alpha \, e^{i\alpha} \left[\frac{1}{s_2 - s_1} \int_{s_1}^{s_2} ds \, I(\alpha, \delta) \right] \tag{4.3}$$

where $s = \sin\delta$ and δ_1, δ_2 are upper and lower declination bounds of the field of view. With $s_{1/2} = \sin\delta_{1/2}$ and $c_{1/2} = \cos\delta_{1/2}$ the rescaled amplitude $\tilde{A}_1$ is then:

$$\tilde{A}_1 \simeq \frac{\delta_1 - \delta_2 + c_1 s_1 - c_2 s_2}{2\,(s_1 - s_2)} A_1 \tag{4.4}$$

For a pure dipole anisotropy, the phase is equal to the true dipole phase $\tilde{\alpha}_1 = \alpha$. Amplitudes from experiments, which only report 1D results, therefore need to be rescaled to be compared to each other. For KASCADE and KASCADE-Grande, this yields a rescaling factor of 1.34.

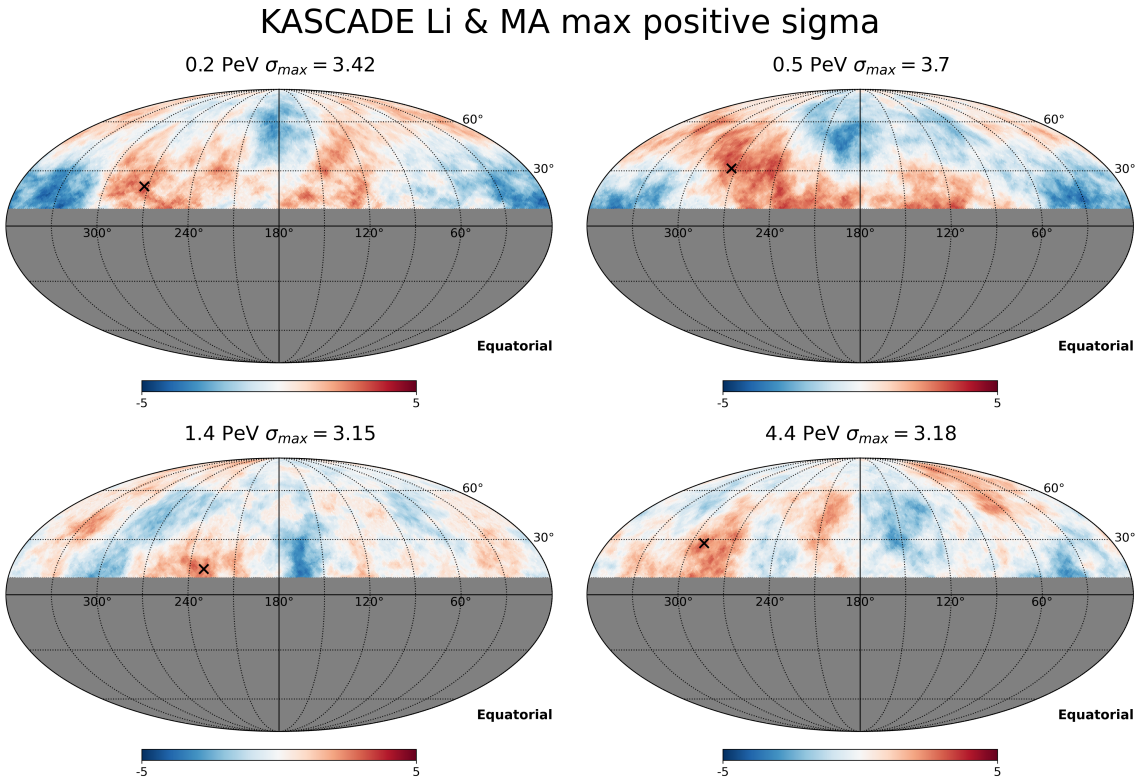

Figure 4.10.: Smoothed sky maps of the reconstructed pre-trial Li & Ma significance for KASCADE. The maximum positive pre-trial significance is indicated above the corresponding sky map and the location is marked with a cross.

The second option is to fit a 2D function to the anisotropy, as it was also done in Abbasi et al. [9] for IceCube data:

$$F(\alpha_i, \delta_i) = \sum_{n=1}^{3} A_n \cos^n(\delta_i)\ \cos(n\alpha_i + \phi_n) \tag{4.5}$$

where n corresponds to the multipole order and A_n and ϕ_n are the corresponding amplitudes and phases.

For both the 1D and 2D fits, the unsmoothed data and background maps were used to calculate anisotropies. In the one-dimensional analysis, as presented in Fig. 4.11, the sky map was divided into 20 right ascension bins. Data and background maps were summed over all pixels within each right ascension bin, and relative intensity was computed from these sums. Assuming that the LLH method accurately estimates the expected number of events, the error on the relative intensity is given by the Poisson uncertainties of the data $\sigma_I = \sqrt{d_a}/b_a$. This relation was used to calculate the errors on the one-dimensional projection. To illustrate the result of the two-dimensional fit, Fig. 4.12 presents the smoothed map of the 1.4 PeV energy bin alongside the corresponding two-dimensional fit.

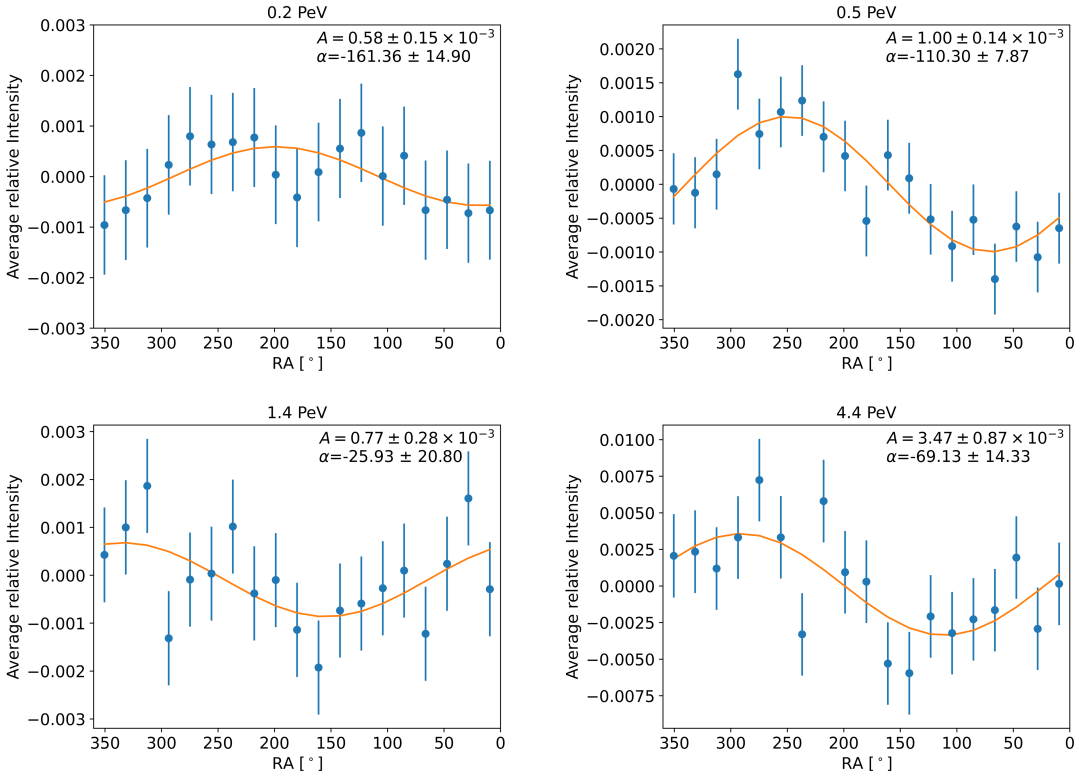

Figure 4.11.: One-dimensional projection for KASCADE. The unsmoothed data and background maps were used to calculate an average relative intensity for right ascension bins.

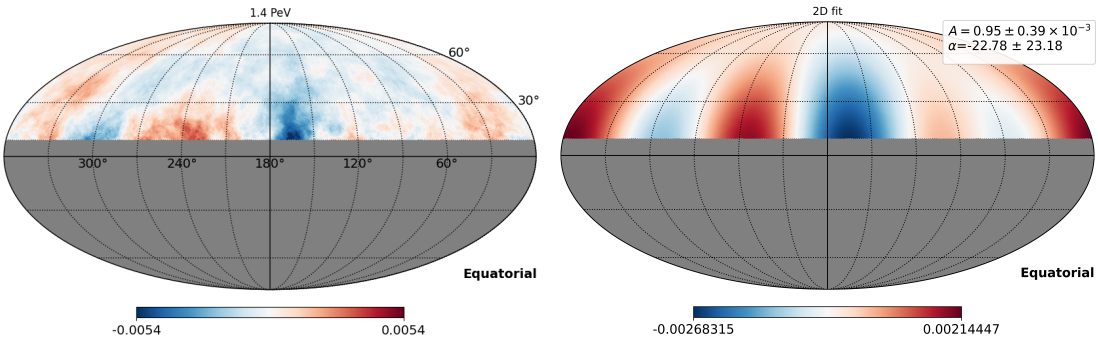

Figure 4.12.: Example comparison of the smoothed anisotropy map (left) and the two-dimensional fit (right) for the 1.4 PeV energy bin of KASCADE is shown.

Another option is to redefine the likelihood, so that it depends directly on the components d_x and d_y of the dipole vector (see Chapter 3.1):

$$\lambda = 2 \ln \frac{\mathcal{L}\left(n \mid d_x^\star, d_y^\star, N_\tau^\star, A_i^\star\right)}{\mathcal{L}\left(n \mid 0, 0, N_\tau^{(0)}, A_i^{(0)}\right)} \tag{4.6}$$

The results from direct dipole likelihood estimation are compared with the results of the 1D and 2D fits in Table 4.2. The 1D results have been corrected for the limited field of view and coincide with the 2D results within their uncertainties, as anticipated. Note that the uncertainties for the 1D and 2D results present only the statistical errors on the estimators derived from the fits. In the case of direct likelihood estimation, parameter uncertainties are determined using the likelihood ratio. The magnitude of these uncertainties depends directly on the total event count and on an additional factor, which accounts for the fact that the statistical power of the data is also used to independently estimate the background rate (see chapter 3.2). A comparison between these dipole results with various other experiments is shown in Fig. 4.13. Overall, the results of this work are in good agreement with previous observations. The phase increases from 200° (1D Results) at 0.2 PeV to 334° at 1.4 PeV and then slightly decreases to 288° at 4.4 PeV. For the lowest energy bin, the phase is lower than that reported from IceCube and Tibet, but it aligns with the phase flip at around 10^{14} eV seen by several observatories. The phase values between the dipole likelihood estimation and the 1D projection for energy bin 2 differ. The resulting uncertainties associated with the dipole LLH are larger for the phase and amplitude across all energy bins, especially for energy bin 3. This may be due to the dipole likelihood method's assumption of dipole anisotropy. If the reconstructed anisotropy is not primarily a dipole, as it is for energy bin 3 (see Fig. 4.8) the resulting likelihood ratio, i.e. the dipole likelihood divided by the likelihood for isotropy, may be small, leading to larger uncertainties and higher p-values. This issue might be improved by truncating the multipole expansion at higher multipole moments l in future analyses. The amplitude rises with increasing energy from $0.78 \cdot 10^{-3}$ at 0.2 PeV (1D result) to $4.66 \cdot 10^{-3}$ at 4.4 PeV.

	A_{1D} [10^{-3}]	α_{1D} [°]	A_{2D} [10^{-3}]	α_{2D} [°]	A_{LLH} [10^{-3}]	α_{LLH} [°]	Pre-trial max. Li & Ma	Post-trial max. Li & Ma	Dipole likelihood p-value
bin 1	0.78 ± 0.20	199 ± 15	0.97 ± 0.15	199 ± 9	0.77 ± 0.35	205 ± 26	4.38	3.77	0.077
bin 2	1.34 ± 0.18	250 ± 8	1.52 ± 0.17	245 ± 6	1.36 ± 0.32	214 ± 14	4.15	3.50	0.00012
bin 3	1.04 ± 0.38	334 ± 21	0.95 ± 0.39	337 ± 23	0.25 ± 0.68	355 ± 152	3.82	3.11	0.931
bin 4	4.66 ± 1.16	291 ± 14	5.31 ± 1.13	288 ± 12	3.33 ± 1.97	280 ± 34	3.35	2.54	0.237

Table 4.2.: Amplitudes and phases of the dipole reconstruction results. The 1D amplitudes have been corrected for the limited FOV. The reported Li & Ma values correspond to the maximum absolute significance.

The maximum absolute pre-trial Li & Ma significance for medium-scale features is observed for the lowest energy bin corresponding to 4.38 σ. After adjusting for the number of trials, the post-trial significance is 3.77 σ. The significance of large-scale features is estimated using the likelihood ratio of the pure dipole LLH method, assuming that Wilks' theorem is applicable (see Chapter 3.2). The minimum p-value is reached for bin 2 with a value of $1.2 \cdot 10^{-4}$. The significance in sigmas, meaning the number of standard deviations that a Gaussian variable would fluctuate in one direction to yield the same p-value, would then be 3.66 σ. The complete dataset was also analysed to identify a large-scale dipole. Since it covers a broad energy range and therefore yields only a mean of an energy-dependent dipole, it may not be suitable for direct comparison with results presented as a function of

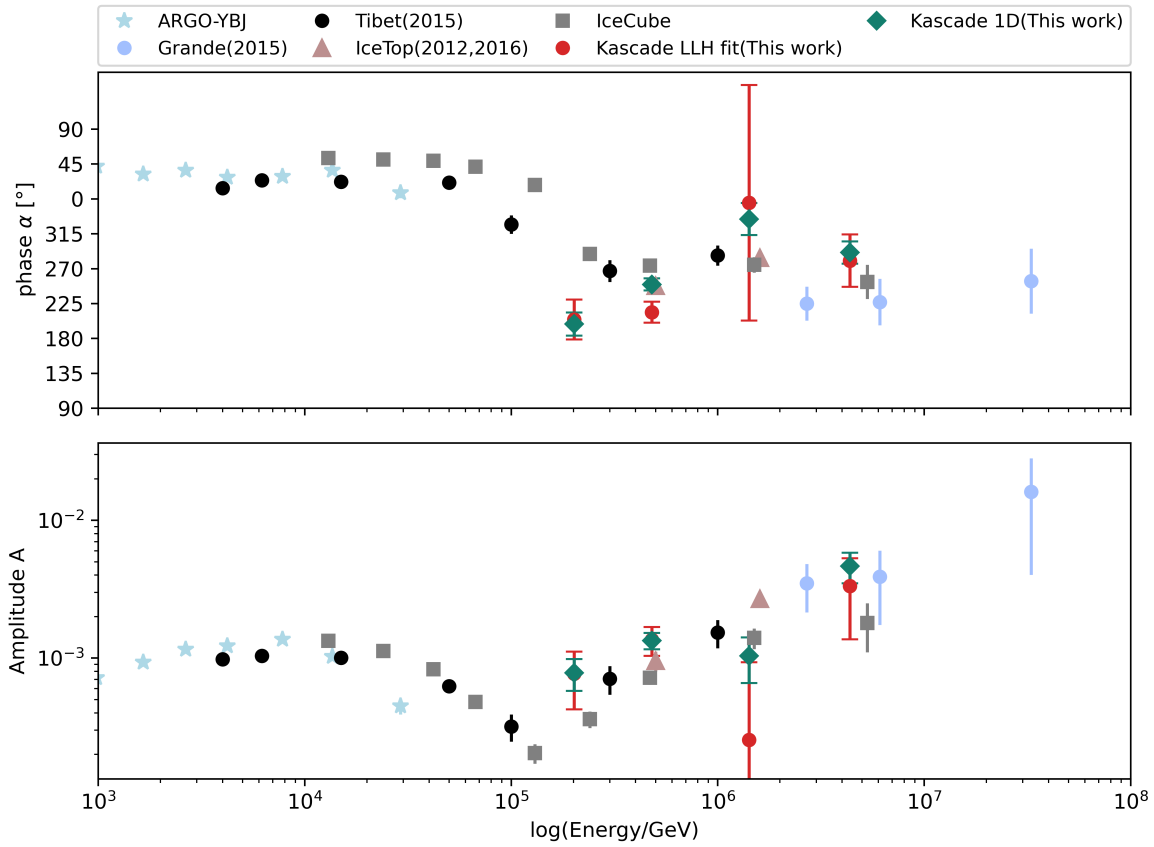

Figure 4.13.: KASCADE results compared with other experiments: IceTop [5], Tibet [22, 23], ARGO-YBJ [31], IceCube [9] and KASCADE-Grande with the East-West method [33]. The one-dimensional results have been corrected for the corresponding FOV. The reconstructed phase (top) and amplitude (bottom) of the dipole component, obtained from the 1D fit and the dipole LLH method, are shown with green and red markers, respectively.

energy. Nevertheless, it can still be used to assess the significance of a large-scale dipole signal across the dataset. A skymap and the corresponding dipole fit is shown in section 4.3. The p-value for the complete dataset is $3.04 \cdot 10^{-5}$, corresponding to 4.01σ.

4.3. KASCADE systematic checks

To assess the reliability and consistency of the findings described in Chapter 4.2, a series of systematic checks were conducted in different reference frames. To explain these reference frames, it is best to examine Earth's motion over a day. A solar day is defined as the time span after which the Sun is in the same position in the sky relative to the Earth. However, due to Earth's rotation around its axis, the period for celestial objects to complete an apparent orbit around Earth is slightly shorter and is referred to as a sidereal day. This is illustrated on the left side of Fig. 4.14. One year has 365.24 solar days, but 366.24 sidereal days. Consequently, the length of a sidereal day is around 23 hours and 56 minutes. In the solar reference frame,

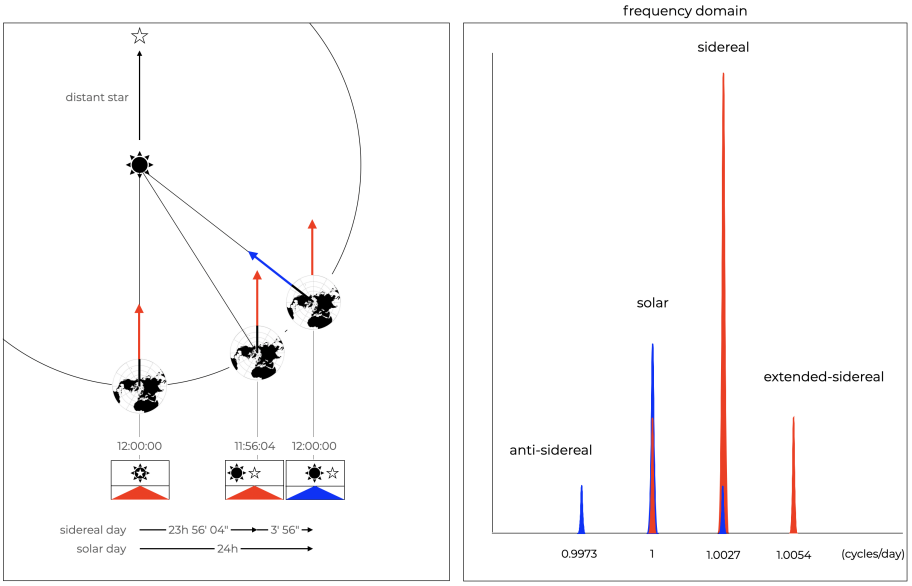

Figure 4.14.: Overview of reference systems. Left: Schematic of sidereal and solar reference frame. Right: Sidereal and solar frequency bands and the side-bands due to interference. Taken from [36].

an apparent excess of cosmic ray events in the direction of Earth's movement exists. This is known as the Compton-Getting effect and can be explained by Earth's motion through a flux of cosmic ray particles [34]. This dipole was measured by various detectors and should give inside on the stability of the analysis. The excess is given as:

$$\frac{\Delta I}{I} = (\gamma + 2)\frac{v}{c}\cos\theta, \tag{4.7}$$

where γ is the spectral index, v is the speed of Earth's motion and θ is the angle between arrival direction and the direction of motion. If the measurement time spans exactly one or more full years, the modulations average out. But in the presence of time gaps, there is a modulation of the solar and sidereal dipole. The interference between the solar and sidereal variations with frequencies $\omega_{sol} = 1/24\,\mathrm{h}$ and $\omega_{sid} = 1.0027/24\,\mathrm{h}$ creates modulations at frequency sidebands $\omega_{sol} \pm \omega_{sid}$. Therefore, the anti-sidereal and extended-sidereal sidebands shown in Fig. 4.14 can be used to determine the extent of the interference [36]. The anti-sidereal time frame comprises 364.24 days per year, while the extended-sidereal time frame consists of 367.25 days per year. Both frames are non-physical, therefore any detected dipole should be attributed to interference between different reference frames. Figure 4.15 presents the results for sidereal, solar, anti-sidereal, and extended-sidereal anisotropies for the complete KASCADE data set. Since this chapter does not aim to estimate an energy-dependent dipole but instead focuses on characterizing the influencing systematics, it is advantageous to use the complete data set to increase the available statistics. The anti-sidereal anisotropy exhibits a relatively large amplitude of $(1.13 \pm 0.09) \cdot 10^{-3}$ (1D results, uncorrected for FOV), which is in the same order of magnitude as the sidereal amplitude. This is also true for amplitude in the extended-sidereal reference system. The solar dipole measured by IceCube is $(2.242 \pm 0.029) \cdot 10^{-4}$ and a phase of $(268.00 \pm 0.75)^\circ$ [3] and is therefore about half as big as in this measurement. This discrepancy is likely due to frequent

gaps in data acquisition, ongoing recalibrations, and detector maintenance. An indication of this is also provided by the number of events per 6 minutes in various reference frames, as shown in Fig. 4.6. A strong variation appears in the solar reference frame, while smaller variations in the sidereal and anti-sidereal frames are observed. An additional indication is the phase of the solar dipole, which differs from the expected value of 270°. If gaps in data-taking are distributed so that they cancel each other out, the measured anisotropy is not expected to be influenced. But if, for instance, every Monday morning there is a gap in data collection or a recalibration, this could affect the measured sidereal and solar amplitudes. To assess these potential effects, the sidereal, solar, and anti-sidereal amplitudes were calculated and the complete data set was divided into various bins. Since the number of events is insufficient to split the data into smaller time bins, such as individual years, the data is split into two halves. This was done for the selections: day, night, summer, winter, first half and last half of data taking, even and odd Unix time, which gives the time of the event in seconds after January 1st 1970, as well as for different days of the week. Table 4.3 summarises the different tests and the reconstructed amplitudes and phases. The corresponding sky maps as well as the dipole fits are shown in Fig. 4.16.

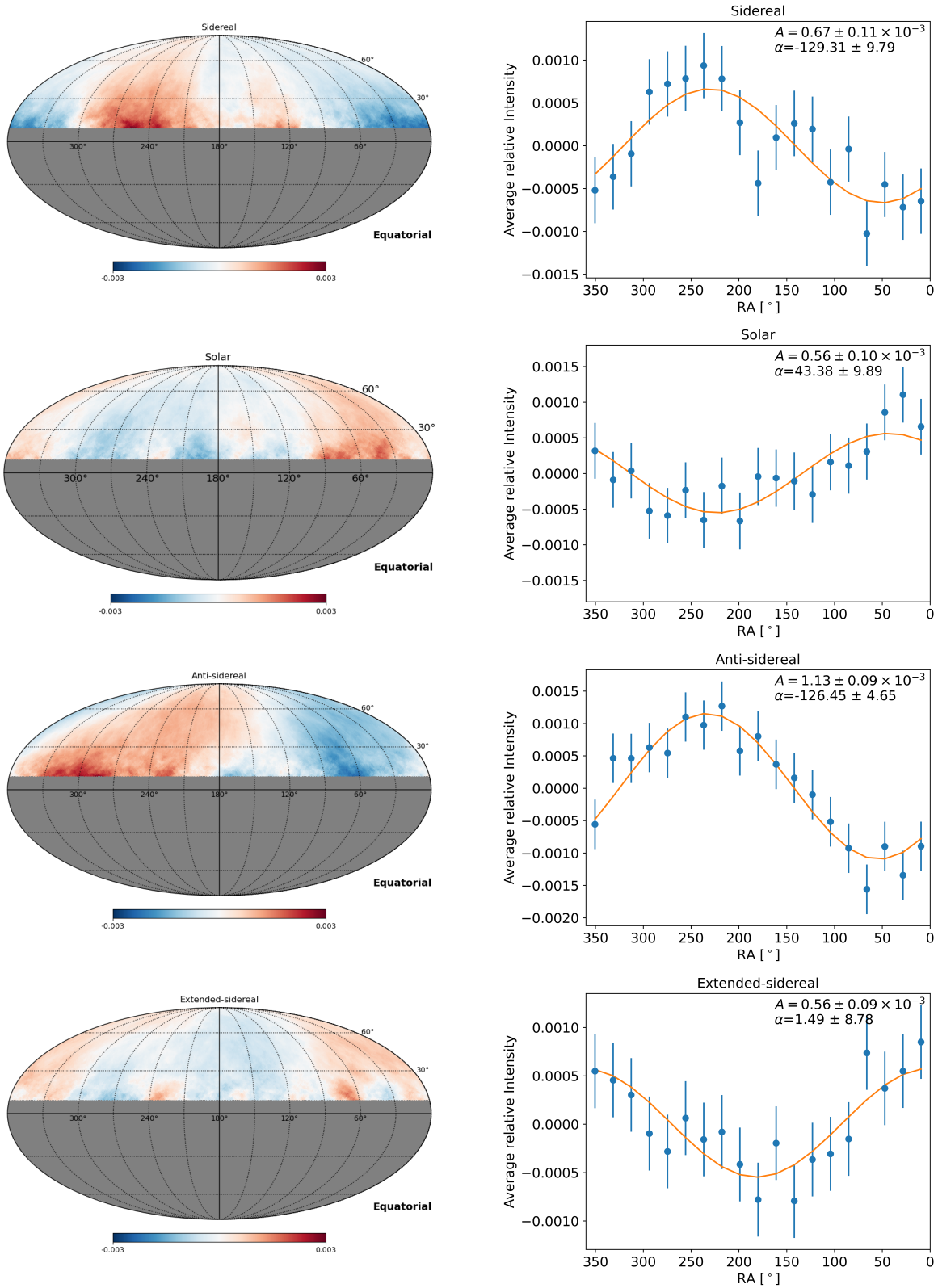

Figure 4.15.: Sidereal, solar, anti-sidereal and extended sidereal smoothed anisotropy sky maps for the complete data set of KASCADE.

Table 4.3.: Results of systematic tests for KASCADE. The one dimensional results A_{1D} are not corrected for the FOV

	Definition	N_{Events} [10^6]	A_{1D} [10^{-3}]	α_{1D} [°]
Sidereal	complete data	371.36	0.67 ± 0.11	230.69 ± 9.79
Solar	complete data	371.36	0.56 ± 0.1	43.38 ± 9.89
Anti-Sidereal	complete data	371.36	1.13 ± 0.09	233.55 ± 4.65
Ext-Sidereal	complete data	371.36	0.56 ± 0.09	1.49 ± 8.78
Day	between 6.00 am and 18 pm	184.69	1.76 ± 0.23	174.36 ± 7.38
Night	between 18.00 pm and 6 am	190.39	1.35 ± 0.16	303.89 ± 6.92
Summer	01.04 to 31.09	179.12	1.03 ± 0.19	266.99 ± 10.35
Winter	01.10 to 31.03	195.95	0.84 ± 0.14	177.11 ± 9.41
Unix even	Unix time is even	185.68	0.62 ± 0.18	243.05 ± 17.04
Unix odd	Unix time is odd	185.67	0.74 ± 0.13	220.41 ± 9.99
First half	01.01.1999 to 01.01.2006	168.57	1.15 ± 0.16	236.54 ± 7.91
Last half	01.01.2006 to 01.01.2013	186.01	0.48 ± 0.14	300.46 ± 17.07
Mondays and Tuesday	each from 00:00:00 to 23:56:04	104.49	0.37 ± 0.16	260.85 ± 23.85
Wednsday and Thursday	each from 00:00:00 to 23:56:04	106.80	0.90 ± 0.20	222.94 ± 12.63
Saturday and Sunday	each from 00:00:00 to 23:56:04	105.36	0.83 ± 0.23	228.25 ± 15.91

The amplitude results for the first half, last half, Unix even, and Unix odd exhibit significant fluctuations, while the reconstructed phase remains more stable. The results from only daytime and only nighttime also differ significantly, due to a phase-shift by about 120°. To some degree, a difference between these two measurements is expected, as neither could cover a full sidereal days. Also, the day reference frame is always affected by the Sun's shadow, whereas the night reference frame is not. The amplitudes for summer and winter are similar, but the phases differ by about 90°. Some of this may result from differences in atmospheric pressure and temperature. The binning by weekday was done by collecting events from 00:00:00 to 23:56:04 for each day, corresponding to one entire sidereal day. This approach ensured that the analysis was not affected by partial sidereal-day intervals, which could otherwise introduce bias. The results for the different weekday selections is relatively stable for the phase and only for Monday and Tuesday show differences in amplitude. The results for the weekdays (Fig. 4.18) and the first half, last half, Unix even, and Unix odd in Fig. 4.16 indicate that, despite the large anti-sidereal and solar amplitudes, the phase in the sidereal reference frame remains relatively stable.

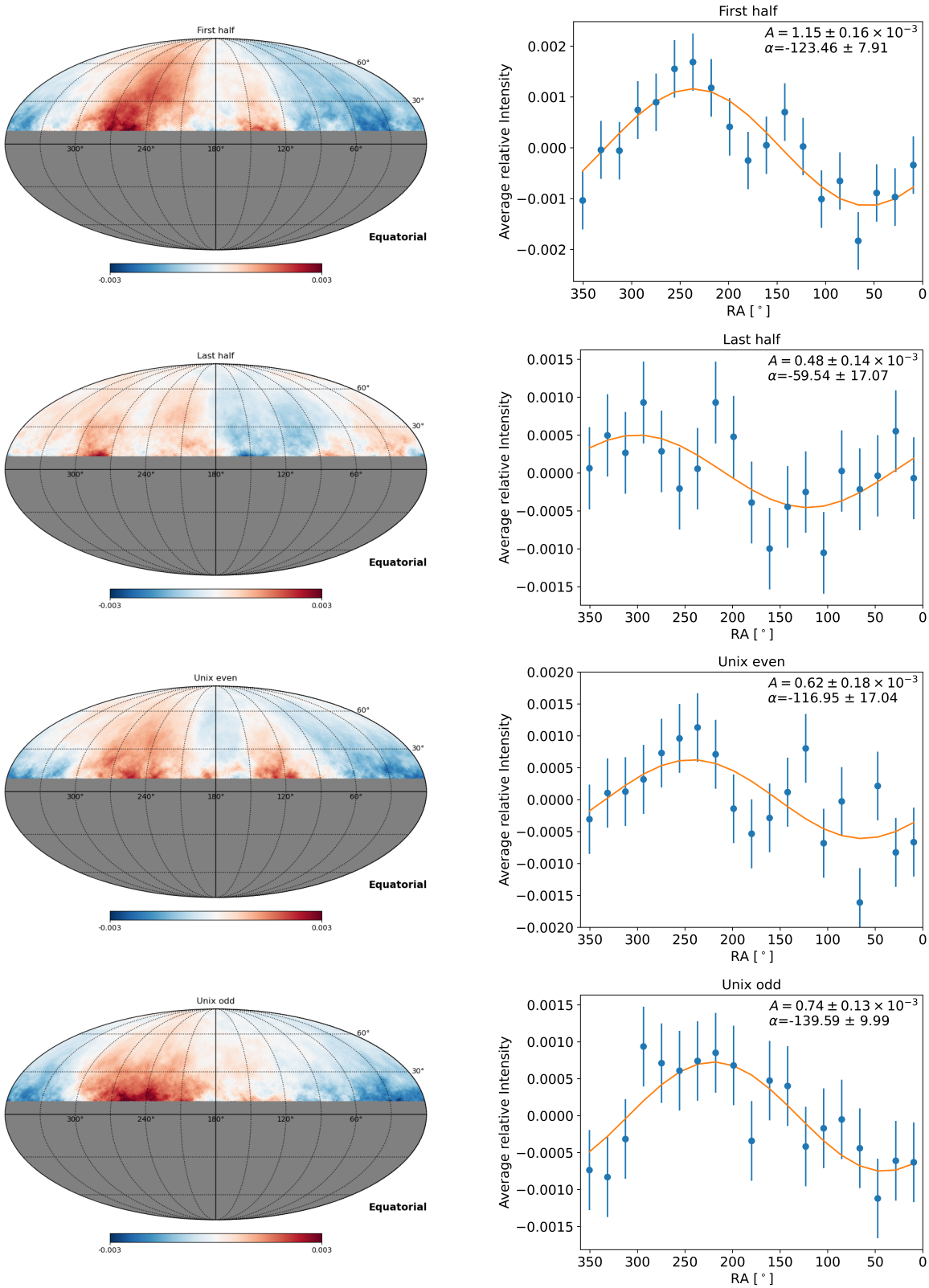

Figure 4.16.: Results for various systematic tests for the complete data set of KASCADE. Left: anisotropy sky maps smoothed with a 20° top hat function. Right: Dipole fits on unsmoothed 1D projected anisotropy. Top to bottom: First half of detection period, last half of detection period, Events with even Unix time and odd Unix time.

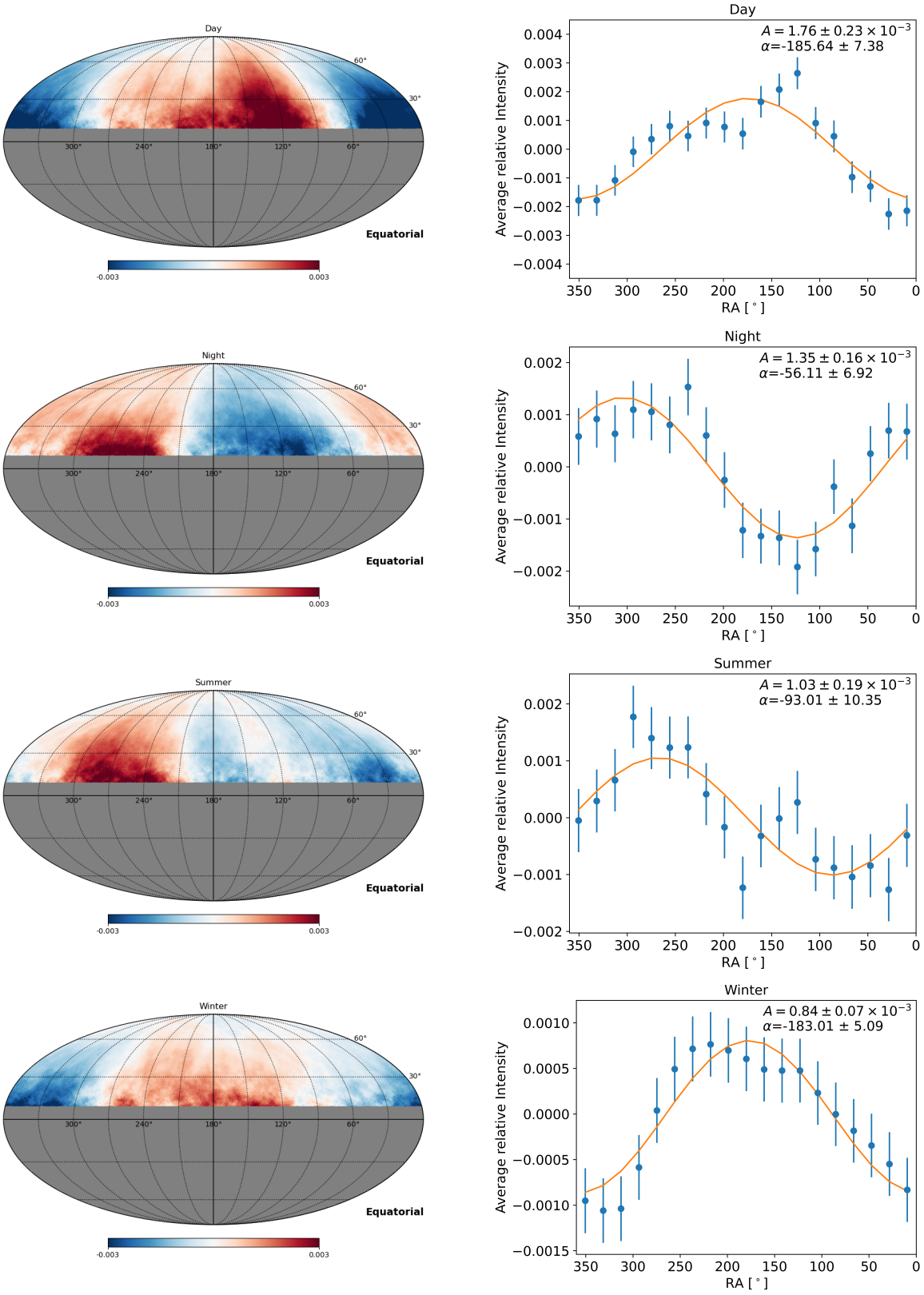

Figure 4.17.: Results for various systematic tests. Left: sky map smoothed with a 20° top hat function. Right: Dipole fits on unsmoothed 1D projected anisotropy. Top to bottom: Only using events during the day, night, summer and winter.

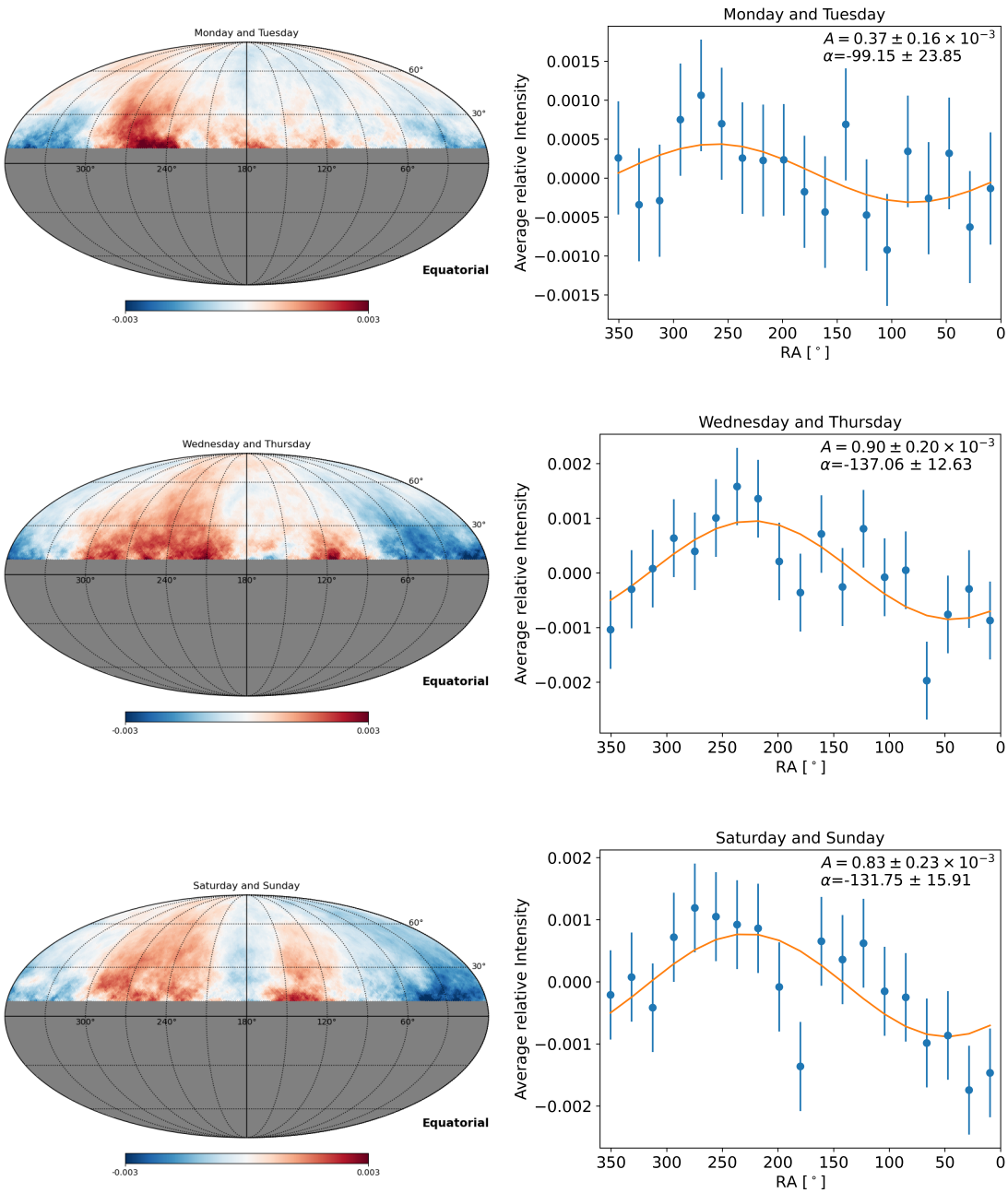

Figure 4.18.: Results for various days of the week. Left: sky map smoothed with a 20° top hat function. Right: Dipole fits on unsmoothed 1D projected anisotropy. Top to bottom: Only using Monday and Tuesday, Wednesday and Thursday and Saturday and Sunday.

Due to the presence of large amplitudes in the anti-sidereal and solar reference frames, as well as significant gaps in data acquisition, the complete dataset was analysed with a focus on fully recorded sidereal days. Since there is no available information on which runs were included in the KCDC release and which were excluded, the detector's uptime and, thus, the periods with full sidereal days had to be determined directly from the available data. First,

the counts per 6 minutes over the full measurement time of KASCADE was determined as shown in Fig. 4.19. To identify periods when the detector operated at full efficiency, only time bins containing more than 200 events were selected. Subsequently, data from these time periods of one or multiple sidereal days were selected for analysis. The resulting sidereal and anti-sidereal distributions, shown in Fig. 4.21, do not differ significantly from previous results. The distributions of events in different reference frames for the entire dataset and only for full sidereal days are depicted in Fig. 4.20, demonstrating that fluctuations in event counts are reduced when analysing solely full sidereal days.

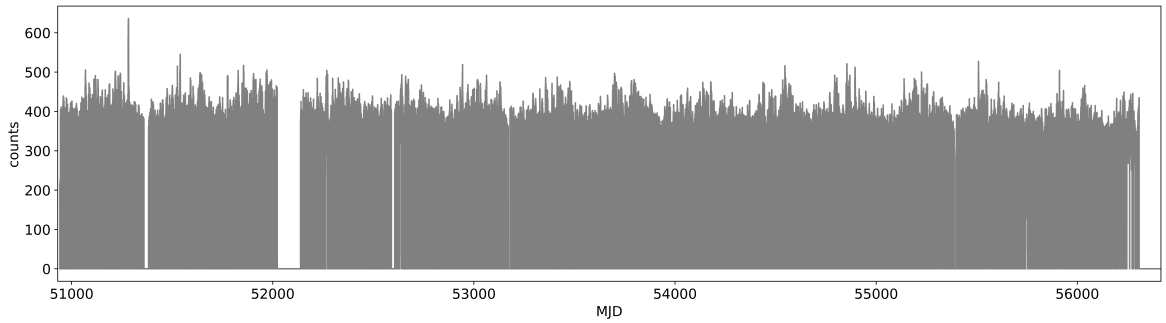

Figure 4.19.: Events per 6 minutes for KASCADE over the Modiefied Julian Date (MJD).

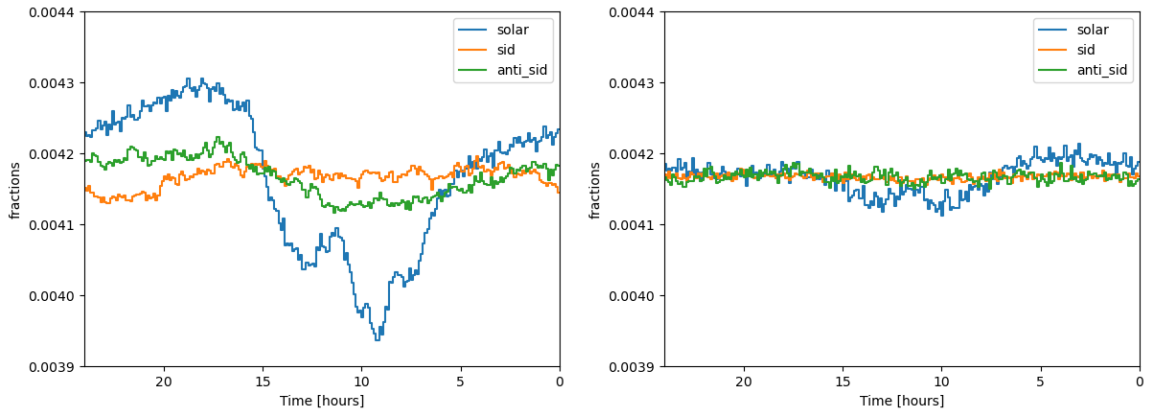

Figure 4.20.: Left: KASCADE fraction of events for various sidereal frames. Right: KASCADE fraction of events for various sidereal frames only considering full sidereal days.

The toy Monte Carlo simulation described in Chapter 3.4 is employed to further examine the significance of the results. In these simulations, an isotropic flux was simulated 10,000 times and a dipole was reconstructed with the one-dimensional methods as described previously. The obtained amplitude distributions are used to estimate the p-value, i.e., the probability of measuring an amplitude of this size or larger under assumption of isotropy, for 10^8, $2 \cdot 10^7$, and $6 \cdot 10^6$ events. The resulting amplitudes for the energy bins for KASCADE, the number of events per bin, the number of events per simulation and the resulting p-values are listed in Table 4.4. None of the measured amplitudes is large enough to yield a significant

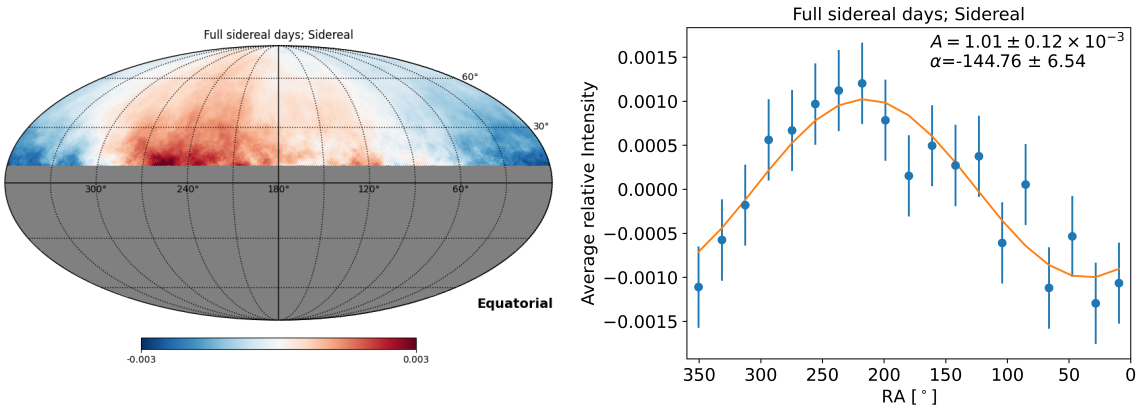

Figure 4.21.: Results for sidereal anisotropy considering only full sidereal days. Left: sky map smoothed with a 20° top-hat function. Right: Dipole fits on unsmoothed 1D projected anisotropy.

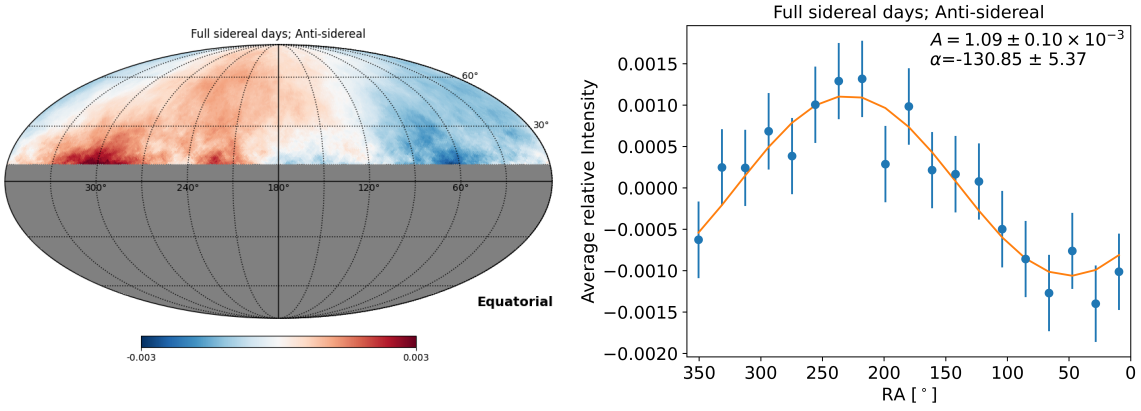

Figure 4.22.: Results for anti-sidereal anisotropy considering only full sidereal days. Left: sky map smoothed with a 20° top-hat function. Right: Dipole fits on unsmoothed 1D projected anisotropy.

p-value. Meaning that the value amplitude can be only treated as an upper limit. Note that this method considers only the value of the amplitude and does not account for the reconstructed phase or the full event distribution, which may result in an underestimation of the dipole's significance. As shown in the Monte Carlo simulations, an isotropic flux produces a uniformly distributed phase. In this measurement, we identify phases that are consistent with other results and remain stable when the dataset is divided into halves, weekdays, or other systematic subsets. A more robust estimate of the significance of large-scale anisotropy might be obtained by evaluating the likelihood ratio of the dipole likelihood relative to the null hypothesis. To cross-check the significance of the resulting likelihood ratio, the Monte Carlo simulations were analysed using the dipole LLH method, and the resulting ratios were saved. Table 4.5 shows the likelihood ratio λ for KASCADE and the resulting p-values estimated with the Monte Carlo simulations. Since only 10,000 Monte Carlo simulations were generated, the smallest resolvable p-value is limited by this

finite sample size. Consequently, for bin 2 and for the full data set, no p-value could be reliably determined because none of the simulated likelihood ratios exceeded the observed value. Overall, the LLH-based p-values are consistent with the expected value under the null hypothesis and the method does not seem to overestimate the significance of the reconstructed dipole structures.

Table 4.4.: Cross-check of the KASCADE amplitude results with Monte Carlo simulations

Bin	Amplitude 1D $[10^{-3}]$	N $[10^6]$	N_{sim} $[10^6]$	Amplitude p-Value
Bin 1	0.78 ± 0.20	194.7	100	0.25
Bin 2	1.34 ± 0.18	147.05	100	0.017
Bin 3	1.04 ± 0.38	26.48	20	0.59
Bin 4	4.66 ± 1.16	3.12	6	0.04

Table 4.5.: Cross-check of the KASCADE dipole LLH p-values

Bin	λ	LLH p-value	MC p-value
Bin 1	5.12	$7.7 \cdot 10^{-2}$	$7.6 \cdot 10^{-2}$
Bin 2	18.02	$1.2 \cdot 10^{-4}$	/
Bin 3	0.14	0.931	0.925
Bin 4	2.88	0.237	0.237
complete data	20.8	$3.04 \cdot 10^{-5}$	/

5. Analysis of KASCADE-Grande data

5.1. KASCADE-Grande detector

The KASCADE detector was extended by the addition of the Grande array to enable studies of cosmic-rays with energies up to 10^{18} eV [30]. The detection area was extended to 0.5 km^2. For this, 37 stations were placed in an irregular triangular grid. The average spacing between the stations is 137 m, and a layout of the detector is shown in Fig. 5.1. Each station consists of 10 m^2 of plastic scintillators. At every station, the scintillation area is formed by 16 stainless steel boxes. Inside each unit is an 80 x 80 x 4 cm^3 plastic scintillator and a photomultiplier tube (PMT). The array is divided into 18 overlapping trigger clusters. Each cluster consists of six detector stations arranged in a hexagonal shape and one central station. The trigger is performed either when 4 stations within a cluster trigger, or by the KASCADE central trigger. In case of a fully coincident event, meaning that all 7 stations from a cluster trigger, the KASCADE array is also read out [30]. KASCADE-Grande measured the total number of charged particles N_{ch} and the number of muons reconstructed by the KASCADE muon detectors. KASCADE-Grande enabled investigation of the knee region, revealing a concave spectral behavior at 10^{16} eV. At energies of around 10^{17} eV an additional knee-like feature was found, referred to as the heavy knee [1]. Furthermore, the individual mass group spectrum was extended to energies of 10^{18} eV.

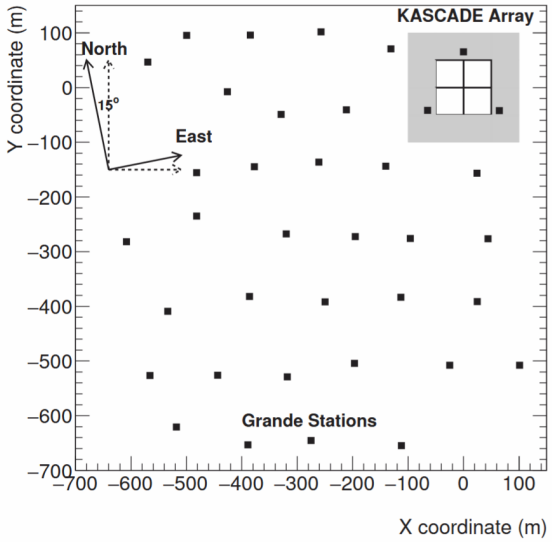

Figure 5.1.: KASCADE-Grande Layout. Taken from [1].

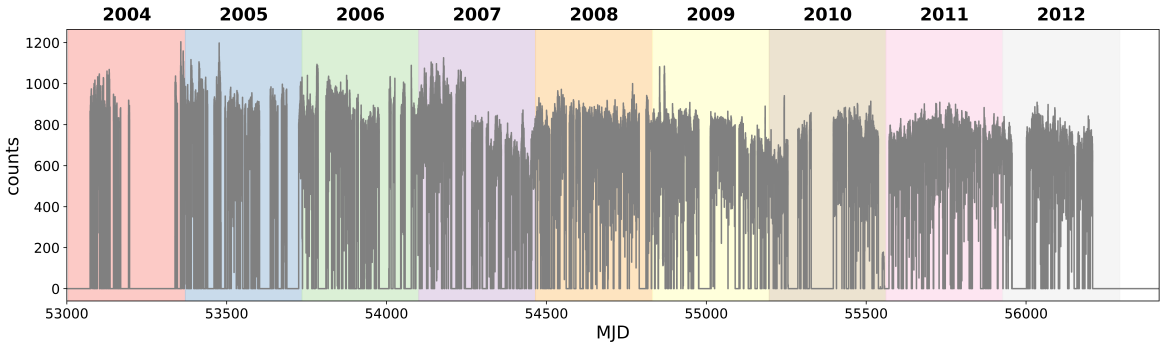

Figure 5.2.: KASCADE-Grande events per week over time.

5.2. Large and medium scale anisotropy

For KASCADE-Grande, the available data was also taken from KCDC [50]. The measurement period for this data set spans from March 2004 to October 2012. During this time period, a total of around 35 million recorded events passed the KCDC quality cuts. These are:

1. All 7 stations of at least one Grande hexagon have triggered.
2. The station with maximum energy deposit is not located at the border of the array.
3. The reconstruction was successful.
4. The shower core lies within a well-defined area and is therefore not too close to the border.
5. The AGE parameter, which describes the lateral shower shape, is between -0.385 and 1.485.
6. The reconstructed zenith angle is below the maximum of 40°.
7. The number of charged particles is greater than 11111.
8. The number of reconstructed muons N_μ is larger than 1500.
9. During the time of measurement the synchrotron facility ANKA was neither in injection nor in beam dumping mode.

The measured events per week over time are shown in Fig. 5.2. Similar to the KASCADE data set, there are several gaps in data taking. To compare the results with previous analyses, the data were binned by the number of reconstructed charged particles, N_{ch}, and the same selection cuts as in Chiavassa [33] and Ahlers [14] were applied. The applied cuts for the three KASCADE-Grande bins, the resulting number of events, as well as the median energy calculated by Chiavassa [33] are shown in Table 5.1. The distribution of the N_{ch} is shown in Fig. 5.3. For this analysis only high energy events with $N_{ch} \geq 10^{5.2}$ were considered.

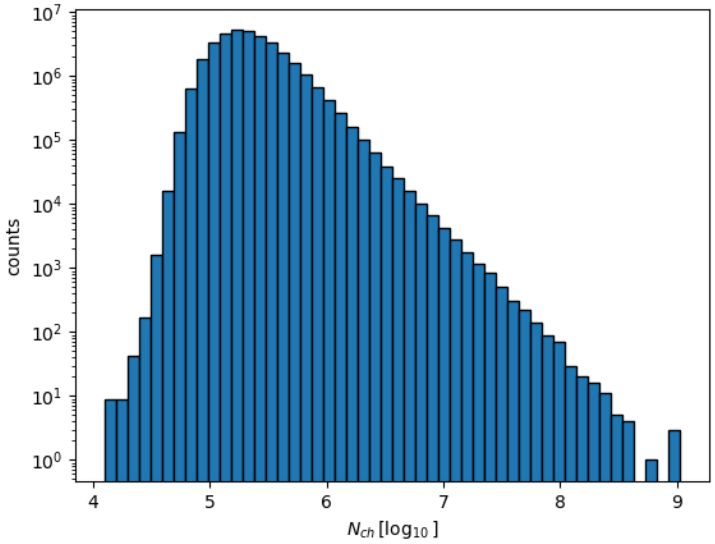

Figure 5.3.: Distribution of the number of charged particles for KASCADE-Grande

	N_{ch} cuts	E_{med} [PeV]	$N[10^6]$
bin 1	$[10^{5.2}, 10^{5.6})$	2.7	17.43
bin 2	$[10^{5.6}, 10^{6.4})$	6.1	6.07
bin 3	$\geq 10^{6.4}$	33	0.146

Table 5.1.: Energy bins for KASCADE-Grande with corresponding number of events per bin, as well as the applied cuts on N_{ch} and the resulting median energies from Chiavassa [33].

The analysis was performed as in Chapter 4.2. This means that the background and data maps were smoothed with a 20° top hat smoothing function. From these smoothed maps, the relative intensity for visualisation has been calculated. For the one-dimensional and two-dimensional fits, the unsmoothed data and background maps were used. The 1D results must be rescaled to account for the detector's limited FOV. In the case of KASCADE and KASCADE-Grande, with a latitude of 49.1° and a maximum used zenith angle of 40°, this results in a correction factor of 1.34. The analysis was also performed with the pure dipole likelihood method (see. Chapter 3.2). As this method was also performed in Ahlers [14], this allows a direct comparison of results with previous findings, as well as a comparison of the results and uncertainties obtained from the 1D and 2D fits with those from the dipole likelihood method. One difference to the analysis of the KASCADE data set is that the local event maps were smoothed with a Gaussian beam with a FWHM of 2°, similar to Ahlers [14], to increase the numerical stability.

A goal of this work is also to provide a detailed, systematic study of the data set and to assess the significance of the observed amplitudes. The resulting smoothed sky maps are shown in Fig. 5.5, and the corresponding pre-trial Li & Ma significances are shown in Fig. 5.6.

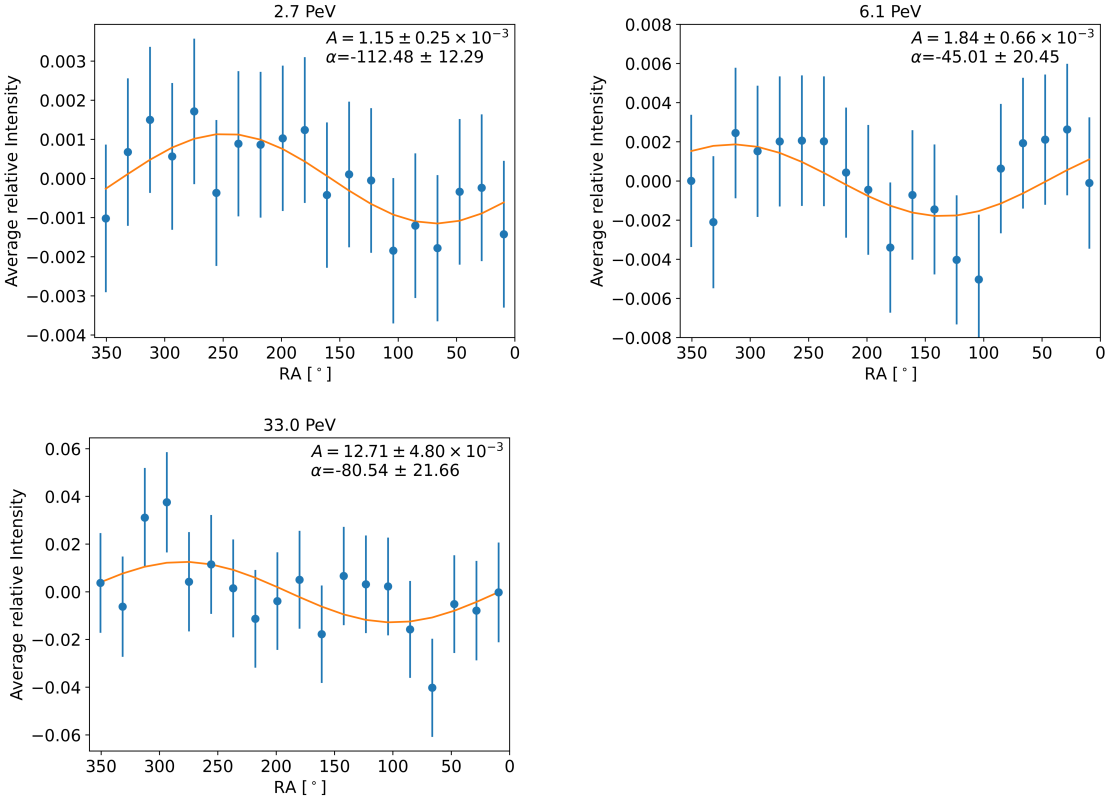

Figure 5.4.: One-dimensional projection for KASCADE-Grande. The unsmoothed data and background maps were used to calculate an average relative intensity for right ascension bins.

The corresponding results from the 1D fits (corrected for the limited field of view), the 2D fits, and the dipole LLH method are summarized in Table 5.2.

The results obtained from the 1D and 2D fits are consistent within their respective uncertainties. It should be noted that the uncertainties associated with the 1D fits are significantly larger than those of the 2D fits. However, this difference is not observed for the phase, where the uncertainties are comparable. The uncertainty obtained with the dipole LLH method depends directly on the number of events and a correction for the agreement with the dipole hypothesis. This leads to large uncertainties when the number of events is low or when the agreement with a dipole is poor. Since the highest energy bin contains only about 146,000 events, the corresponding uncertainties are comparatively large. The pure dipole likelihood results reported by Ahlers [14] are identical to those obtained in this work, as expected, since the same method and data set were employed. This validates the implementation of the dipole LLH method and the analysis procedure. A notable difference between this work and the previous is the maximum pre-trial significance for the medium-scale anisotropy. Although the significance maps look similar and have the same "features", the absolute values of this work are smaller. In the previous publication, the calculation was only stated to be

$$\tilde{\mu}_a^{\mathrm{bg}} = \sum_{b \in \mathcal{D}_a} \sum_{\tau} A^{\star}_{\tau b} \mathcal{N}^{\star}_{\tau} I^{\mathrm{bg}}_{b} \tag{5.1}$$

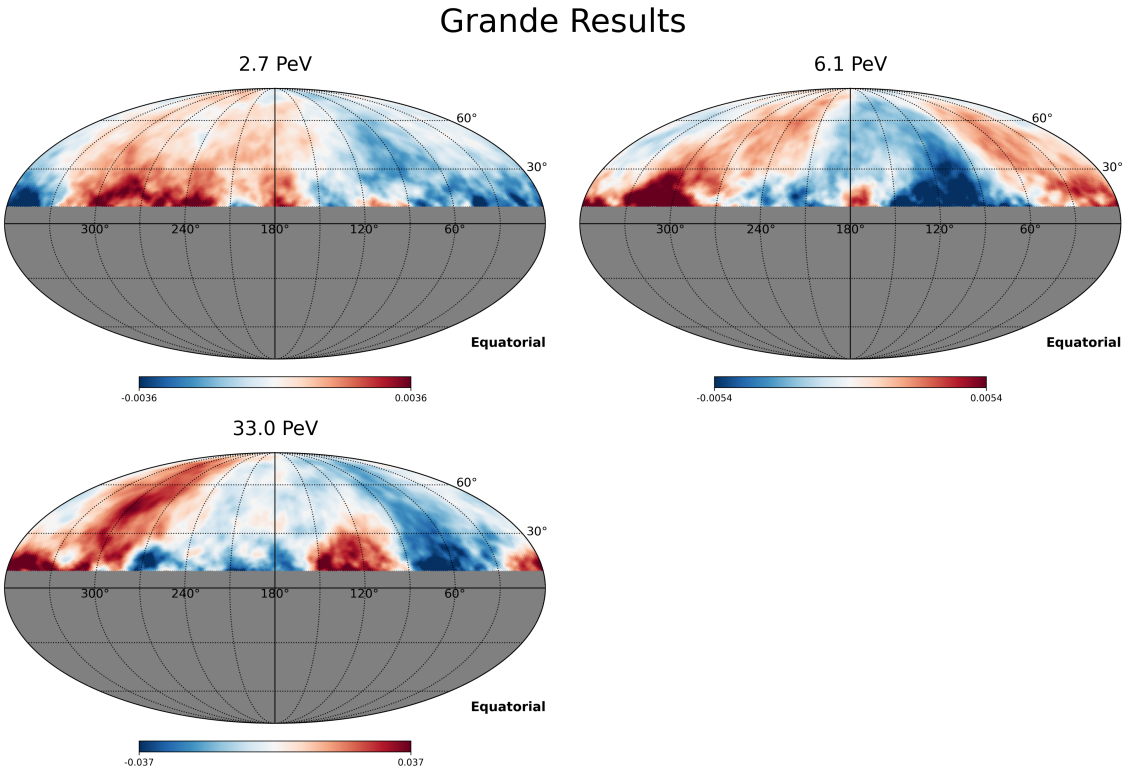

Figure 5.5.: Smoothed sky maps of the reconstructed anisotropy for KASCADE-Grande for the median energy of 2.7 PeV (top left), 6.1 PeV (top right), and 33.0 PeV (bottom left).

with the relative intensity set to $I_{\mathfrak{b}}^{\mathrm{bg}} = 1$. This work uses the 0th iteration estimators for the calculation of $\tilde{\mu}_{\mathfrak{a}}^{\mathrm{bg}}$. To investigate the discrepancy, the significance calculation of this work was performed with final iteration estimators $A_{\tau\mathfrak{b}}^{\star}\mathcal{N}_{\tau}^{\star}$. The resulting maximum pre-trial significances are 2.98 σ, 3.63 σ and 4.53 σ which are very close to the results from Ahlers [14]. The resulting significance maps are shown in Appendix A.1. But as described in Chapter 3.3, the final iterators might lead to an overestimation of the significance.

The pre-trial significance has to be corrected for the number of trials. In this case with a smoothing radius of 20° the number of trials is $N = 14$. The resulting maximum post-trial significances are listed in Table 5.2. The maximum absolute significance is found in bin 3 with a post-trial significance of 2.37 σ and thus no significant medium-scale anisotropy was found. Also, no significant large-scale anisotropy could be found. Therefore, the reported values have to be interpreted as upper values. An overview of the results, compared with other experiments and the previous results from Chiavassa [33], is shown in Fig. 5.7. The pure dipole LLH results are in agreement within the uncertainties with the East–West results reported by Chiavassa [33]. A noticeable deviation is observed only in bin 2, where the reconstructed phase differs substantially. Overall, the phase seems to be stable around the direction of the galactic centre at 260°, while the amplitude increases with energy. An overview of the results for KASCADE and KASCADE-Grande with other experiments and

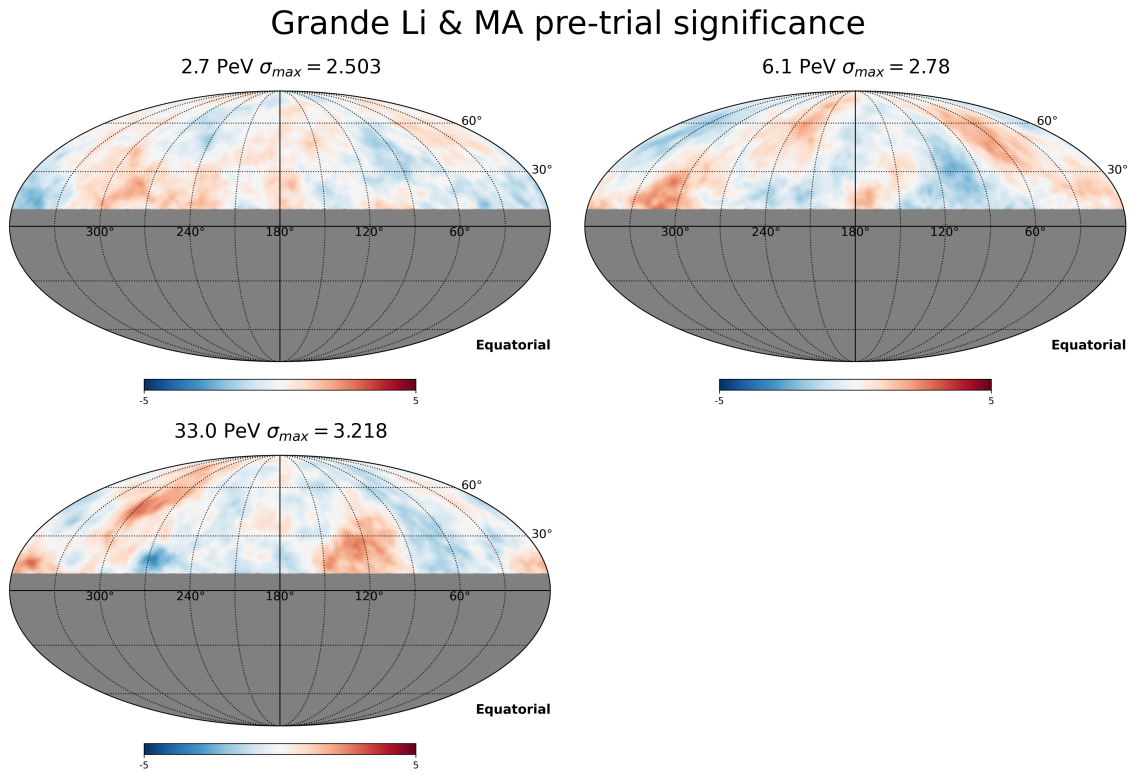

Figure 5.6.: Smoothed sky maps of the reconstructed pre-trial Li & Ma significance for KASCADE-Grande.

also the higher energy measurements from the Pierre Auger Observatory [2] is shown in Fig. 5.8.

Table 5.2.: Dipole reconstruction results. The 1D amplitudes were corrected for the limited FOV.

	A_{1D} [10^{-3}]	α_{1D} [°]	A_{2D} [10^{-3}]	α_{2D} [°]	A_{LLH} [10^{-3}]	α_{LLH} [°]	Dipole likelihood p-Value	Pre-trial max. Li & Ma	Post-trial max. Li & Ma
bin 1	1.54 ± 0.33	248 ± 12	1.85 ± 0.15	245 ± 5	2.16 ± 1.02	243 ± 27	0.10	2.50	1.39
bin 2	2.46 ± 0.88	315 ± 20	2.98 ± 0.25	318 ± 5	3.30 ± 1.78	315 ± 31	0.17	2.78	1.78
bin 3	17.04 ± 6.44	279 ± 22	16.36 ± 1.64	283 ± 6	8.92 ± 11.49	299 ± 74	0.73	3.22	2.37
complete data	1.59 ± 0.33	269.81 ± 11.87	1.84 ± 0.13	268.79 ± 3.95	2.07 ± 0.88	270 ± 15	0.062	2.58	1.49

Table 5.3.: Comparison of East–West and maximum-likelihood results.

	East–West (Chiavassa [33])		East–West (Ahlers [14])		max-$\mathcal{L}$ (Ahlers [14])				
data	A [10^{-3}]	α [°]	A [10^{-3}]	α [°]	A [10^{-3}]	α [°]	λ	p-value	Pre-trial max. Li & Ma
bin 1	2.6 ± 1.0	225 ± 22	3.4 ± 1.5	218 ± 26	2.1 ± 1.0	243 ± 27	4.49	0.11	3.09
bin 2	2.9 ± 1.6	227 ± 30	1.9 ± 2.7	281 ± 82	3.3 ± 1.8	314 ± 31	3.46	0.18	3.54
bin 3	12 ± 9	254 ± 42	24 ± 18	240 ± 42	9 ± 11	299 ± 77	0.57	0.75	4.73

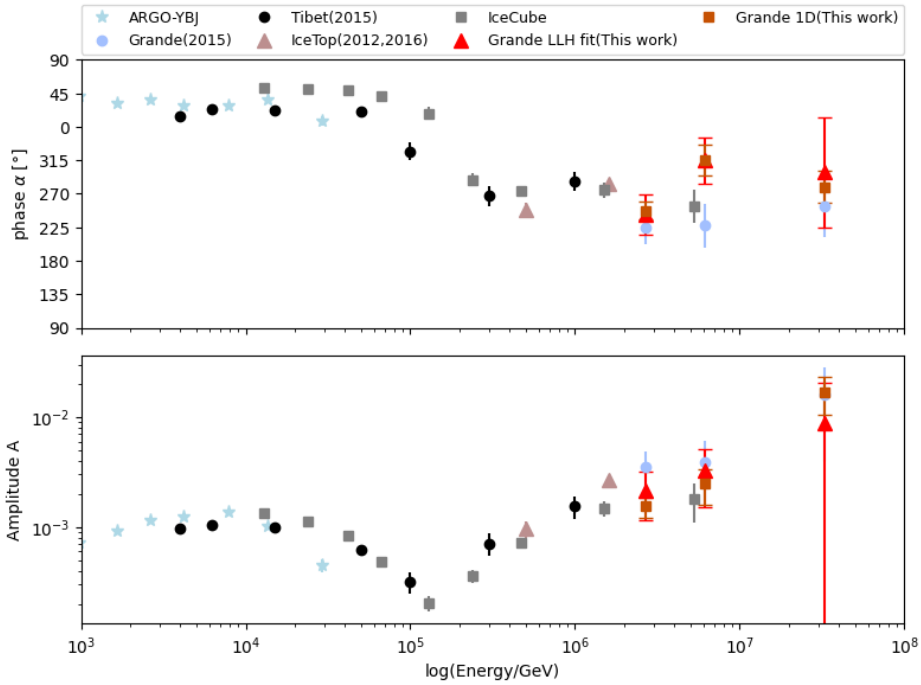

Figure 5.7.: KASCADE-Grande results compared with other results: IceTop [5], Tibet [22, 23], ARGO-YBJ [31], IceCube [9] and KASCADE-Grande with the East-West method [33]. The red triangle and red square markers represent the results obtained from the LLH fit and the 1D fit method, respectively. All one-dimensional measurement of the amplitude were corrected for their limited FOV.

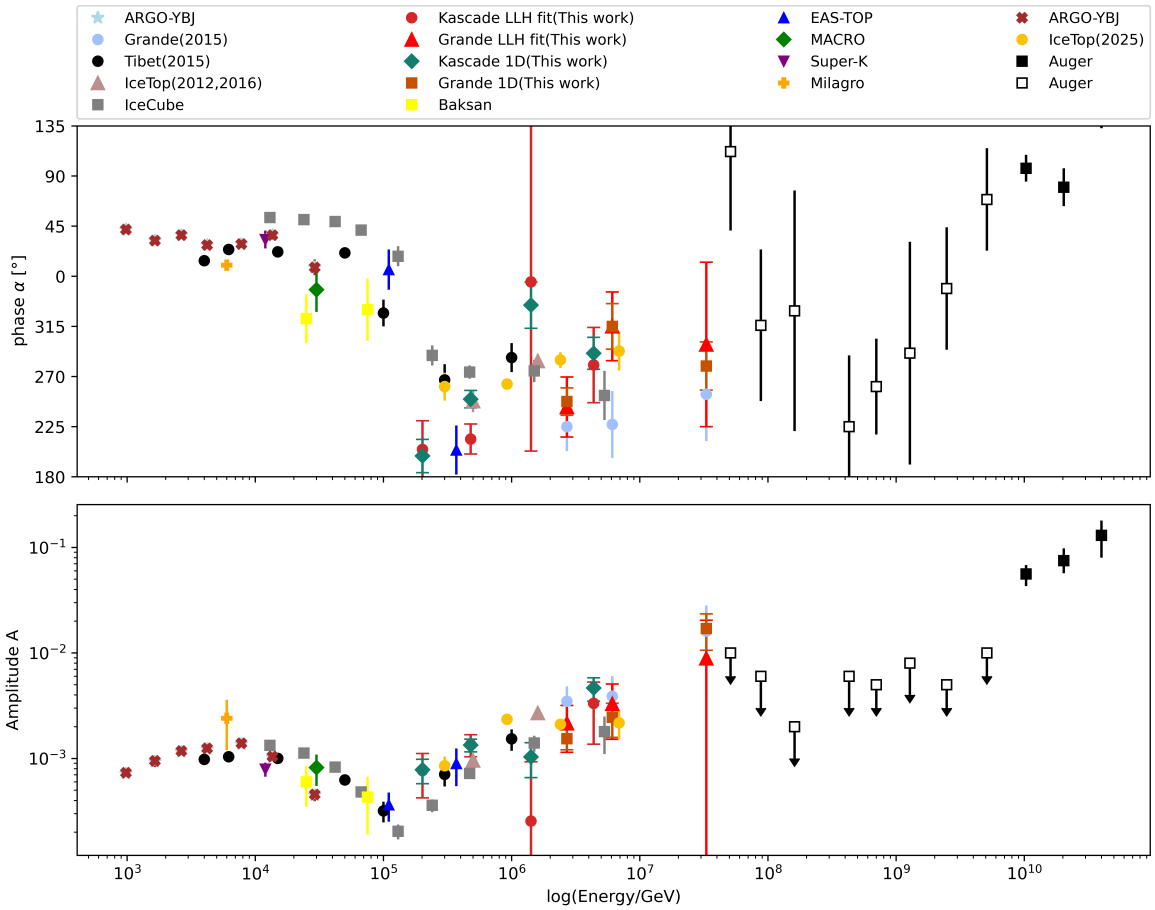

Figure 5.8.: KASCADE and KASCADE-Grande results compared with other results: IceTop [5, 8], Tibet [22, 23], ARGO-YBJ [31], IceCube [9], Baksan [18], EAS-Top [13], Macro [20], Super-Kamiokande [48], Milagro [10],Auger [2] and KASCADE-Grande with the East-West method [33]. All one-dimensional amplitudes were corrected for their limited FOV. MACRO and Baksan could not be rescaled due to limited information about their FOV [9].

5.3. KASCADE-Grande Systematic checks

In this section, the same systematic checks as for the KASCADE data set are performed (see. Section 4.3). This includes an analysis of the complete data set in the sidereal, anti-sidereal, solar, and extended reference frames. Since the complete data set is used for the systematic studies , resulting in a larger number of events, the local data maps were not smoothed with a Gaussian beam as in the previous Chapter. The unsmoothed sideral amplitude results in a FOV corrected value of $(2.56 \pm 0.38) \times 10^{-3}$, which is higher than the smoothed result given in Table 5.2. This already demonstrates some systematics related to the detailed choice of the analysis and smoothing methods. To check the stability of these results the data set was split into various time-based subsets. These include data only from daytime, nighttime, winter, summer, the first half and last half of data taking, even and odd Unix times, which gives the time of the event in seconds after January 1st 1970, as well as for different days of the week (see Fig. 5.10, 5.11, 5.12). A more detailed definition of the selections, the number of events per bin and the resulting one-dimensional fit results are listed in Table 5.4.

Table 5.4.: Results of systematic tests for KASCADE-Grande. The one-dimensional results A_{1D} are not corrected for the FOV.

	Definition	N_{Events} $[10^6]$	A_{1D} $[10^{-3}]$	α_{1D} [°]
Sidereal	complete data	23.63	1.91 ± 0.29	292.81 ± 8.61
Solar	complete data	23.63	0.39 ± 0.38	142.52 ± 56.36
Anti-Sidereal	complete data	23.63	1.21 ± 0.40	196.86 ± 18.84
Ext-Sidereal	complete data	23.63	2.26 ± 0.31	120.63 ± 7.83
Day	between 6.00 am and 18 pm	11.70	3.19 ± 0.37	283.47 ± 6.73
Night	between 18.00 pm and 6 am	11.93	0.88 ± 0.40	326.38 ± 26.06
Summer	01.04 to 31.09	12.09	2.30 ± 0.33	249.1 ± 8.34
Winter	01.10 to 31.03	11.53	2.75 ± 0.38	328.92 ± 7.87
Unix even	Unix time is even	11.81	2.55 ± 0.43	329.43 ± 9.51
Unix odd	Unix time is odd	11.82	2.33 ± 0.49	252.14 ± 12.16
First half	01.01.2005 to 01.01.2009	11.40	0.66 ± 0.51	50.12 ± 43.97
Last half	01.01.2009 to 01.01.2013	11.32	3.71 ± 0.46	291.16 ± 7.11
Mondays and Tuesday	each from 00:00:00 to 23:56:04	6.52	2.29 ± 0.62	241.7 ± 15.47
Wednsday and Thursday	each from 00:00:00 to 23:56:04	6.65	3.86 ± 0.42	4.27 ± 6.28
Saturday and Sunday	each from 00:00:00 to 23:56:04	6.83	2.89 ± 0.6	268.32 ± 11.87

Again similiar to KASCADE, the resulting solar, anti-sidereal and extended sidereal distributions are large. The anti-sideral distribution with $(1.21 \pm 0.40) \times 10^{-3}$ is of the same magnitude as in the KASCADE analysis. For the extended sidereal reference frame, the amplitude for Grande is about four times larger than in KASCADE. As the anti-sidereal and extended sidereal reference frames are unphysical, the phase of the distributions is not relevant. The solar amplitude for KASCADE-Grande is smaller than for KASCADE. However, the strongest structures in the solar reference frame still reach values of about 0.003. In general, the difference in the reconstructed amplitudes and phases from the systematic

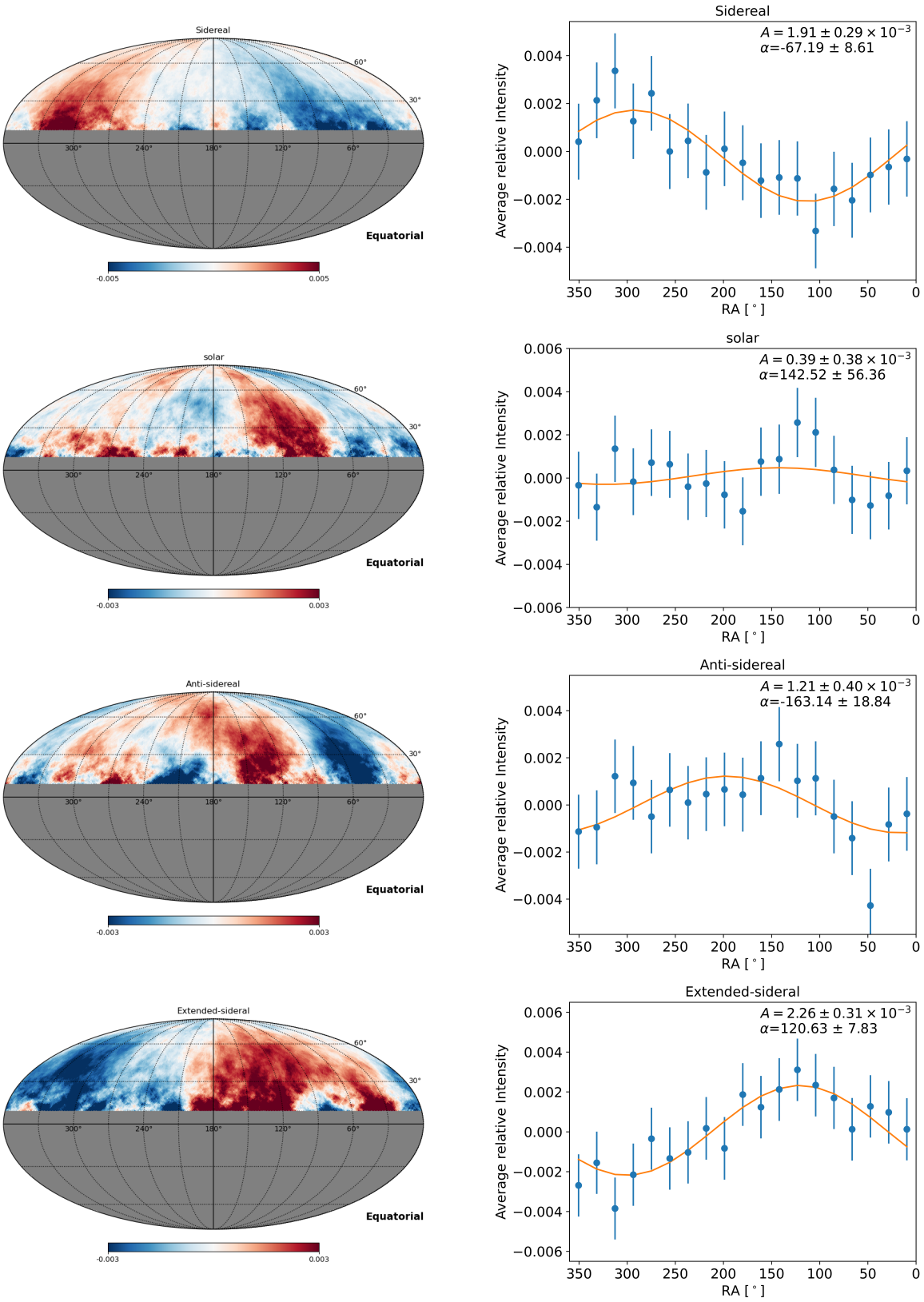

Figure 5.9.: Results for various systematic tests for the complete data set of KASCADE-Grande. Left: anisotropy sky maps smoothed with a 20° top hat function. Right: Dipole fits on unsmoothed 1D projected anisotropy. Top to bottom: Sidereal, solar, anti-sidereal and extended sidereal.

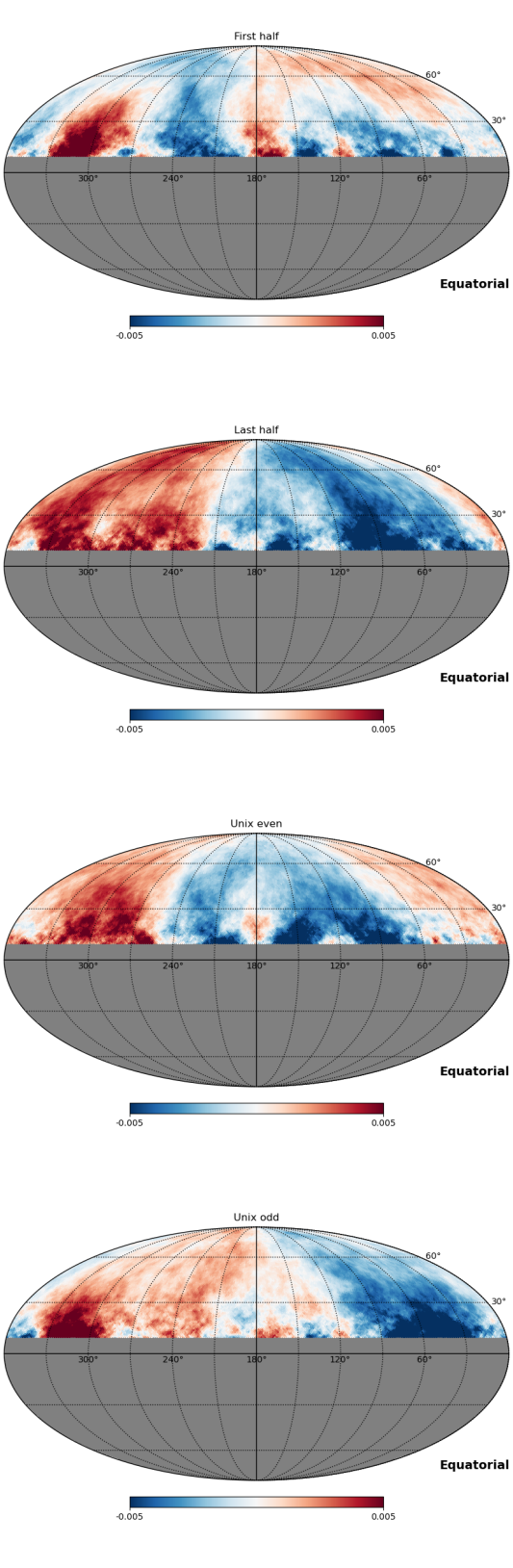

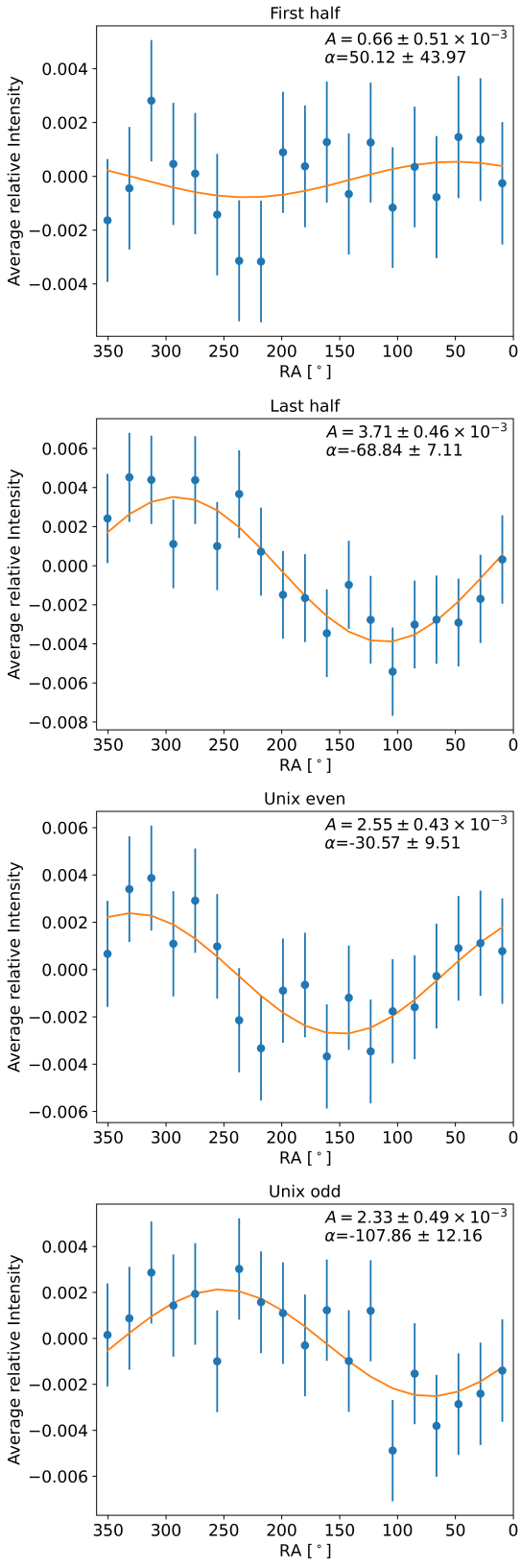

Figure 5.10.: Results for various systematic tests for the complete data set of KASCADE-Grande. Left: anisotropy sky maps smoothed with a 20° top hat function. Right: Dipole fits on unsmoothed 1D projected anisotropy. Top to bottom: First half of detection period, last half of detection period, Events with even Unix time and odd Unix time.

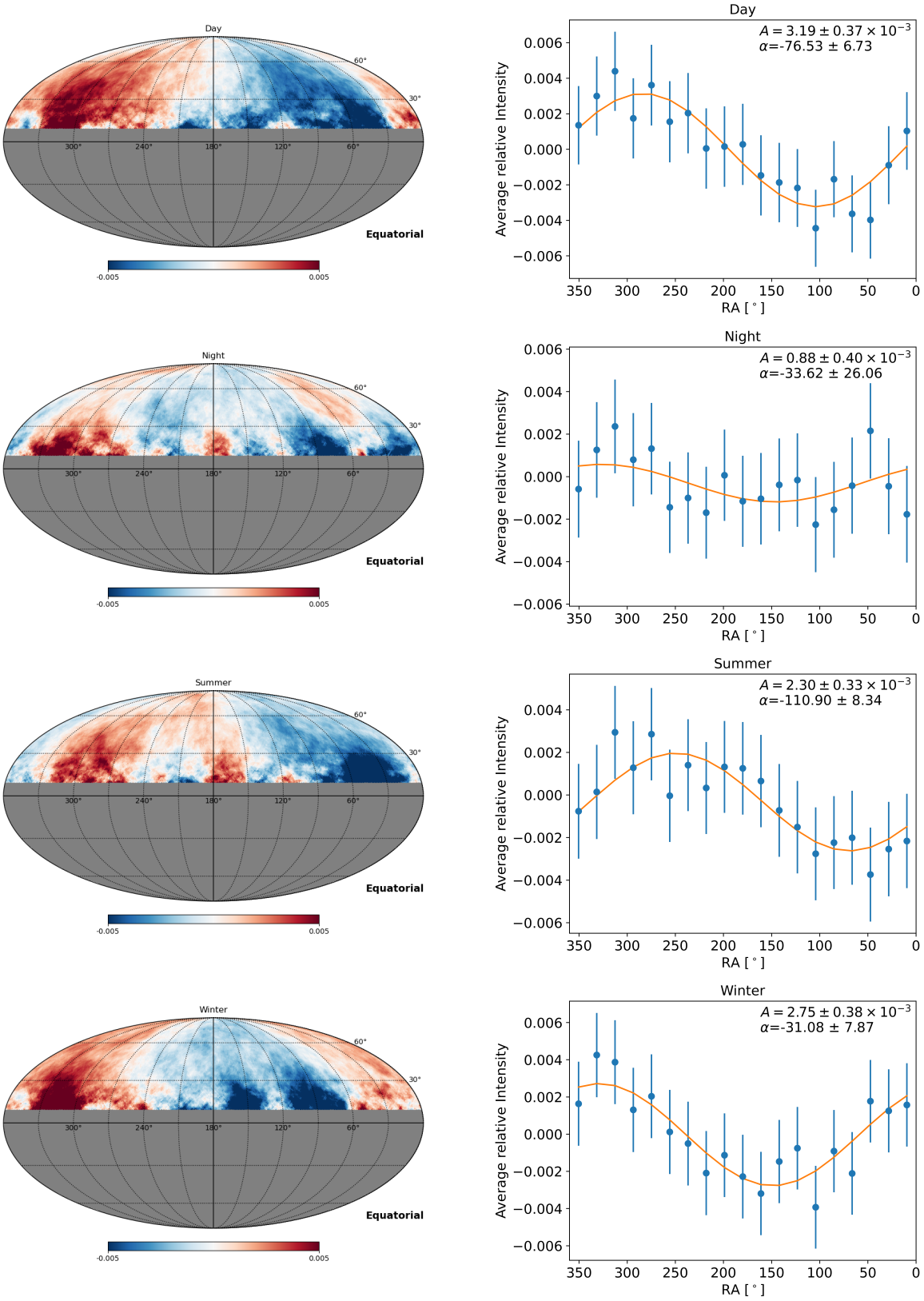

Figure 5.11.: Results for various systematic tests for the complete data set of KASCADE-Grande. Left: anisotropy sky maps smoothed with a 20° top hat function. Right: Dipole fits on unsmoothed 1D projected anisotropy. Top to bottom: Only using events during the day, night, summer and winter.

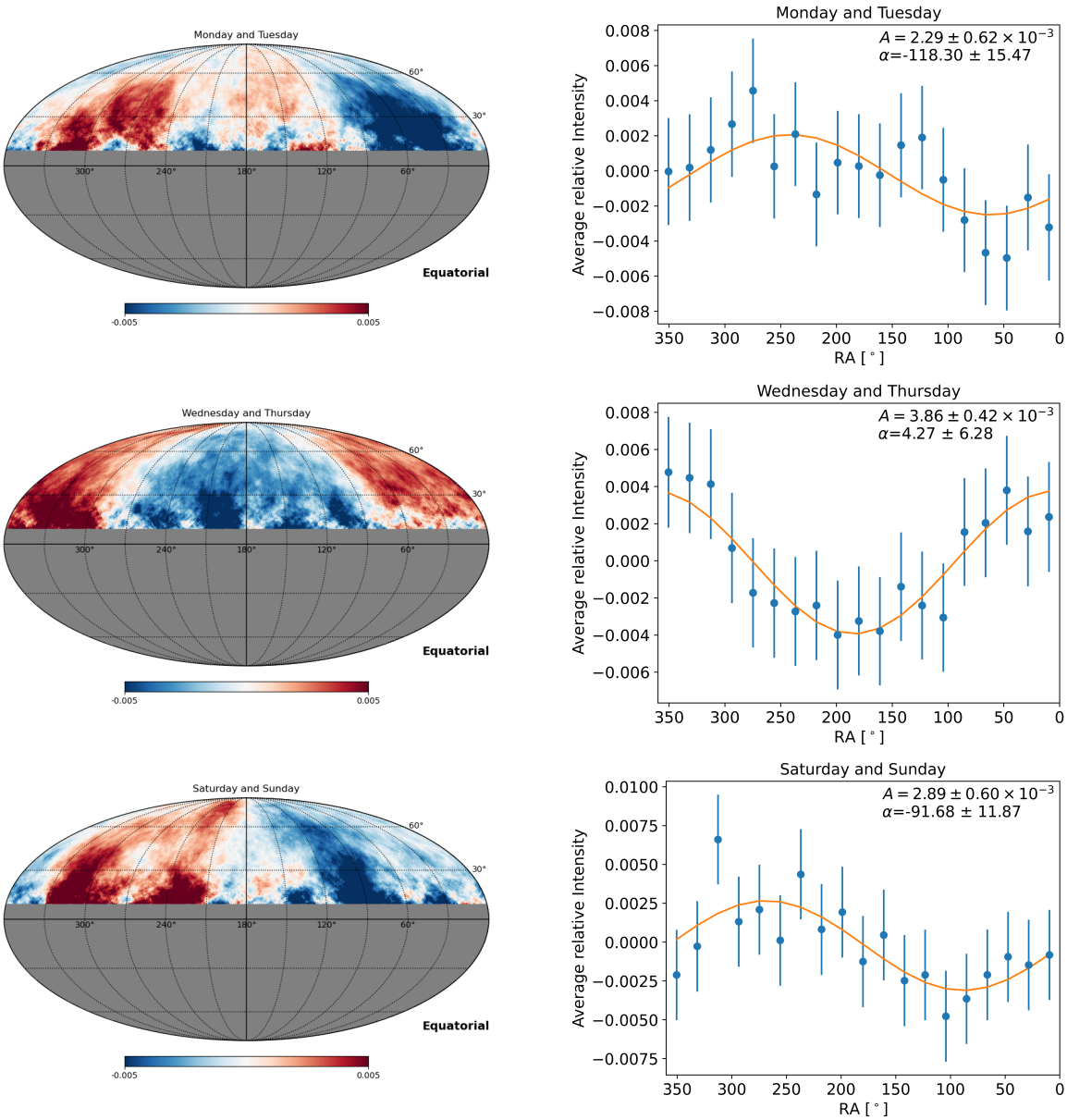

Figure 5.12.: Results for various systematic tests for the complete data set of KASCADE-Grande. Left: anisotropy sky maps smoothed with a 20° top hat function. Right: Dipole fits on unsmoothed 1D projected anisotropy. Top to bottom: Only using Monday and Tuesday, Wednesday and Thursday and Saturday and Sunday.

subsamples, like first/last-half and even/odd Unix times, is larger than in the KASCADE data set. This behaviour is expected, as the number of events is considerably smaller and therefore the fluctuations due to dividing the data into two halves are expected to be larger. A particularly notable difference is observed between the first and last half, as in the first half, the amplitude is about one order of magnitude smaller, and the phase is shifted about 120°. This might be due to the difference in time gaps in the first and last half (see Section 5.2) and the smaller size of the data set. Another notable difference is seen in the analysis

of different weekdays. For Wednesday and Thursday, the phase shift is about 90° to 100° compared to Monday and Tuesday, and Saturday and Sunday. These differences may be due to recalibration, detector maintenance and other man-made effects that accumulate differently across weekdays.

A similar cross-check of the significance of the KASCADE-Grande amplitudes using the previous Monte Carlo simulation was performed. The results are shown in Table 5.5. None of the resulting amplitudes is significant. As in the previous Chapter, the resulting likelihood ratio was also compared to the distribution of likelihood ratios obtained by Monte Carlo simulation for the dipole likelihood method. The results are listed in Table 5.6, and the dipole p-value is consistent with the significance obtained from the Monte Carlo simulations.

Table 5.5.: Cross-check of the KASCADE-Grande results with Monte Carlo simulations.

Bin	Amplitude 1D $[10^{-3}]$	N $[10^6]$	N_{sim} $[10^6]$	p-Value
complete data	1.59 ± 0.33	23.7	20	0.30
Bin 1	1.54 ± 0.33	17.41	20	0.32
Bin 2	2.46 ± 0.88	6.07	6	0.42
Bin 3	17.04 ± 6.44	0.15	/	/

Table 5.6.: Crosscheck of the KASCADE-Grande dipole LLH p-values.

Bin	λ	LLH p-value	MC p-value
complete data	5.56	0.06	0.0615
Bin 1	4.56	0.10	0.103
Bin 2	3.49	0.17	0.174
Bin 3	0.62	0.73	0.726

6. Analysis of IceTop burnsample data

6.1. IceTop Detector

The IceCube Neutrino Observatory is located at the South Pole. It uses 1 km^3 of ice to measure neutrinos via the Cherenkov light emitted by particles produced in neutrino interactions with the ice. The Cherenkov light is measured by Digital Optical Modules (DOMs) attached to 86 strings. In addition to that, IceCube also consists of a more dense sub-part of the detector, DeepCore, located in the inner region of the ice and the surface array IceTop [7]. A schematic of the IceCube detector is presented in Fig. 6.1. IceTop

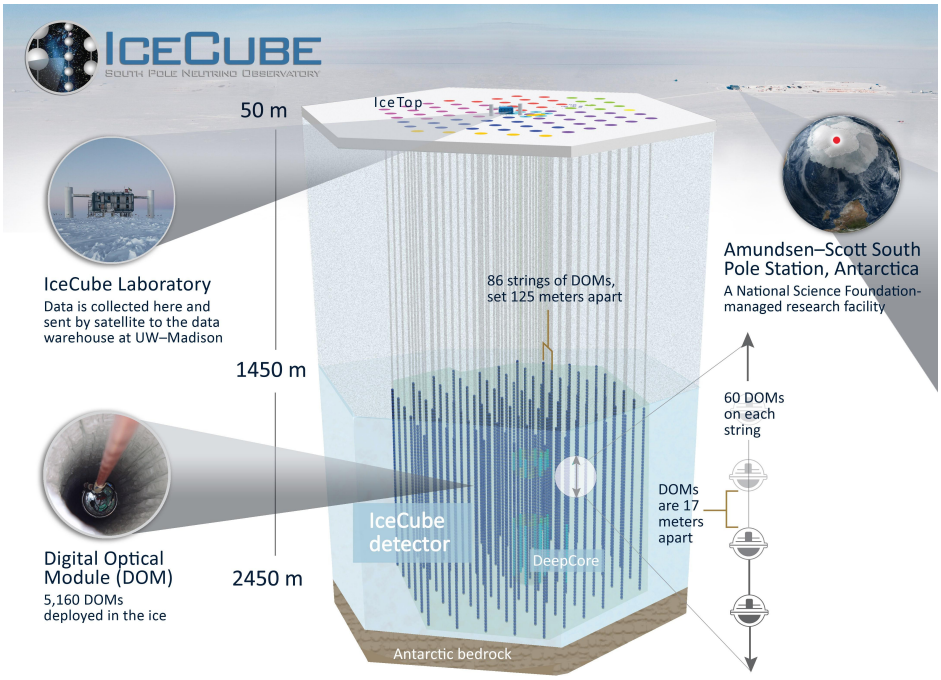

Figure 6.1.: Schematic of the IceCube neutrino observatory [4].

expands IceCube's ability to detect cosmic rays and acts as an additional veto for some of the background muons. The array consists of 81 detector stations arranged on a triangular grid, with an average spacing of 125 m between two stations. Each station consists of two tanks filled with ice and each tank is equipped with two DOMs [7]. An event is triggered if at least 3 stations, corresponding to 6 DOMs, register a signal within a time window of 5 μs [8]. The layout of the IceTop detector is presented in Fig. 6.2. The number of charged

particles at ground level is measured through the detection of the Cherenkov light emitted in the detector stations. Using the information from the triggered stations, the shower direction, core position, and shower size are estimated. This is done by fitting the lateral distribution and the geometric shape of the shower front. The shower size is defined as the signal S_{ref} at a reference distance from the shower core and is a measure of the primary energy. The reference distance for IceTop was set to 125 m, as this leads to the smallest correlation between the shower size S_{ref} and the slope of the lateral distribution β [7]. To not bias the analysis on the full data set, a 10% or 1% burnsmaple is used for validation and testing of the analysis methods.

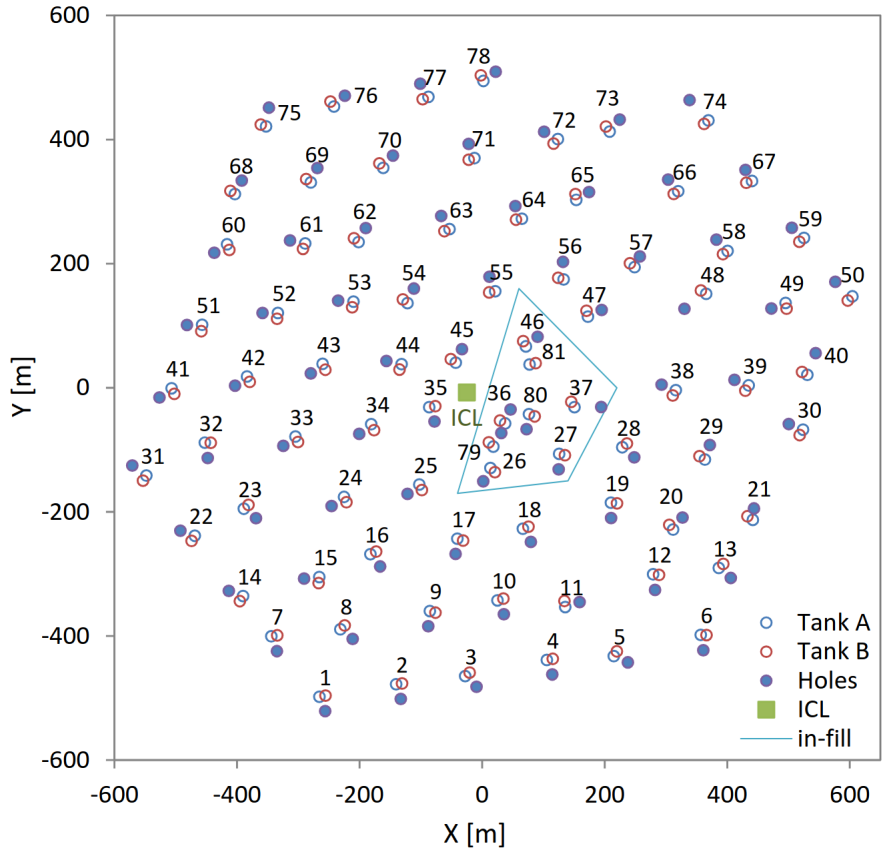

Figure 6.2.: Layout of the IceTop array [7].

6.2. Large scale anisotropy

In preparation for the combined analysis of IceTop with KASCADE and KASCADE-Grande in the subsequent Chapter, the IceTop burn sample is first analysed separately to provide a consistent reference and to validate the analysis procedure. This analysis follows the work of Abbasi et al. [8]. The number of triggered stations is used to bin the data into four energy bins, referred to as "Tiers". Since IceTop is located at the surface of the South Pole,

the accumulated snow on top of the detectors varies with time. Thus, the relation between the number of stations ($n_{stations}$) parameter and the primary energy changes over time. To account for this effect, the number of station cuts is adjusted by about one station every two years. The binning was then validated with comparison of the S_{ref} parameter for every year on the 10% burnsample data in Abbasi et al. [8]. The resulting true energy distributions referred from Monte Carlo simulations are presented in Fig. 6.3, where the events are weighted with the H4a model and the y-axis shows the number of events normalised to the total number of entries. The weighting process for the simulations and the H4a model for the composition of the cosmic rays spectrum are explained in the next chapter. The all particles histogram corresponds to the sum of the proton, helium, oxygen, and iron spectra.

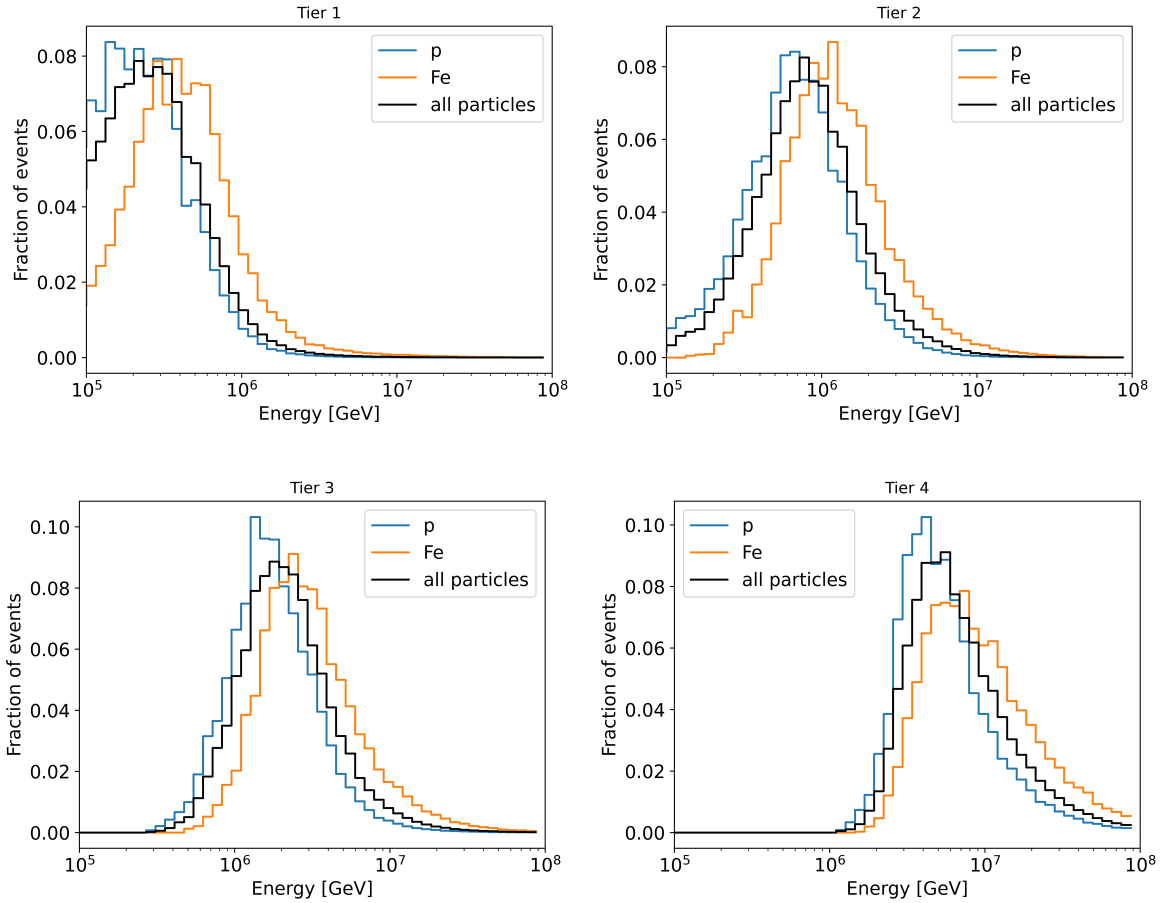

Figure 6.3.: True energy distributions for the resulting IceTop energy tiers for protons (blue) , Iron (orange) and all particles (black). The all-particle distribution corresponds to the sum of the proton, helium, oxygen, and iron spectra.

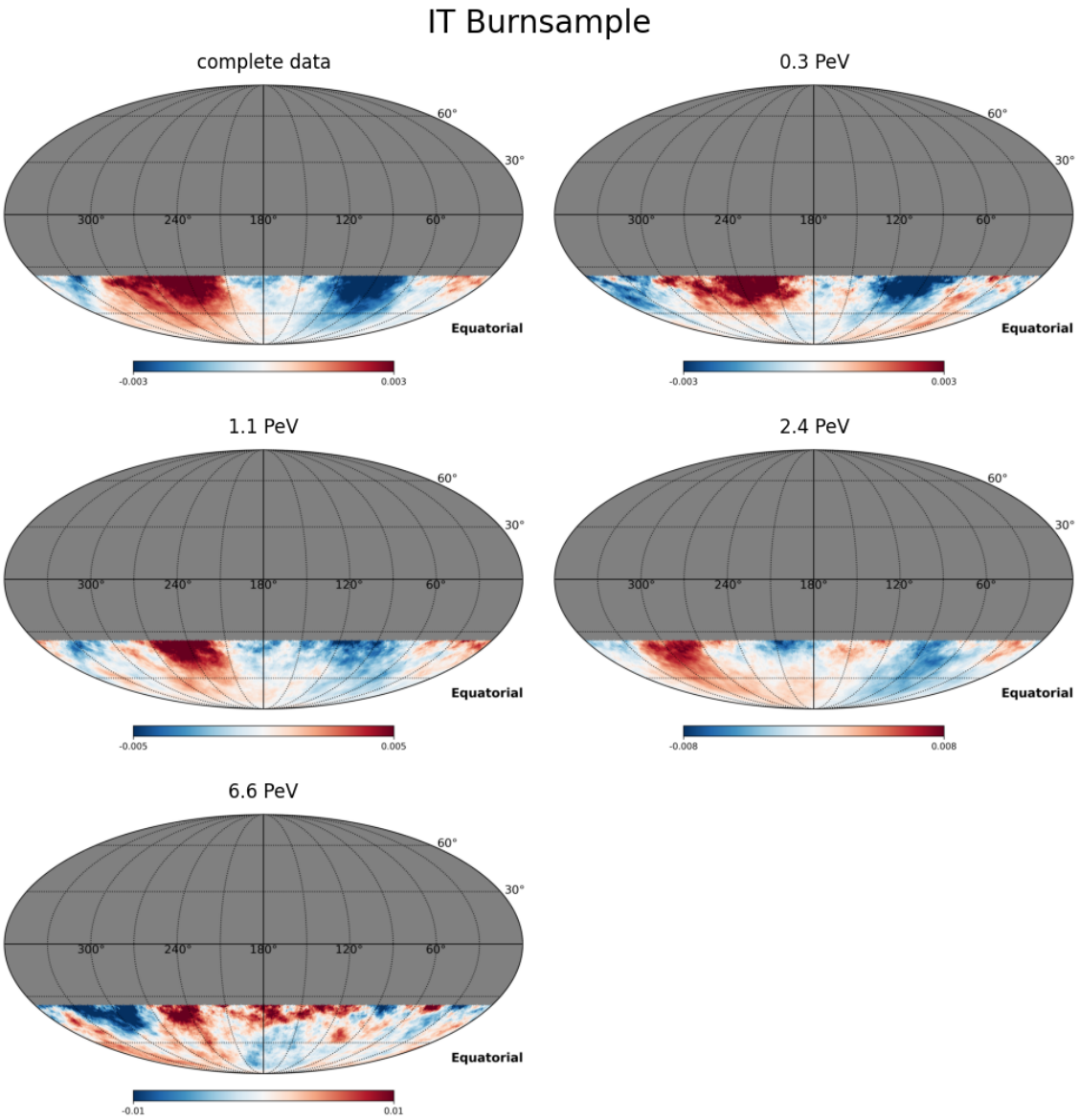

Figure 6.4.: IceTop sidereal anisotropy skymaps smoothed with 20° smoothing radius.

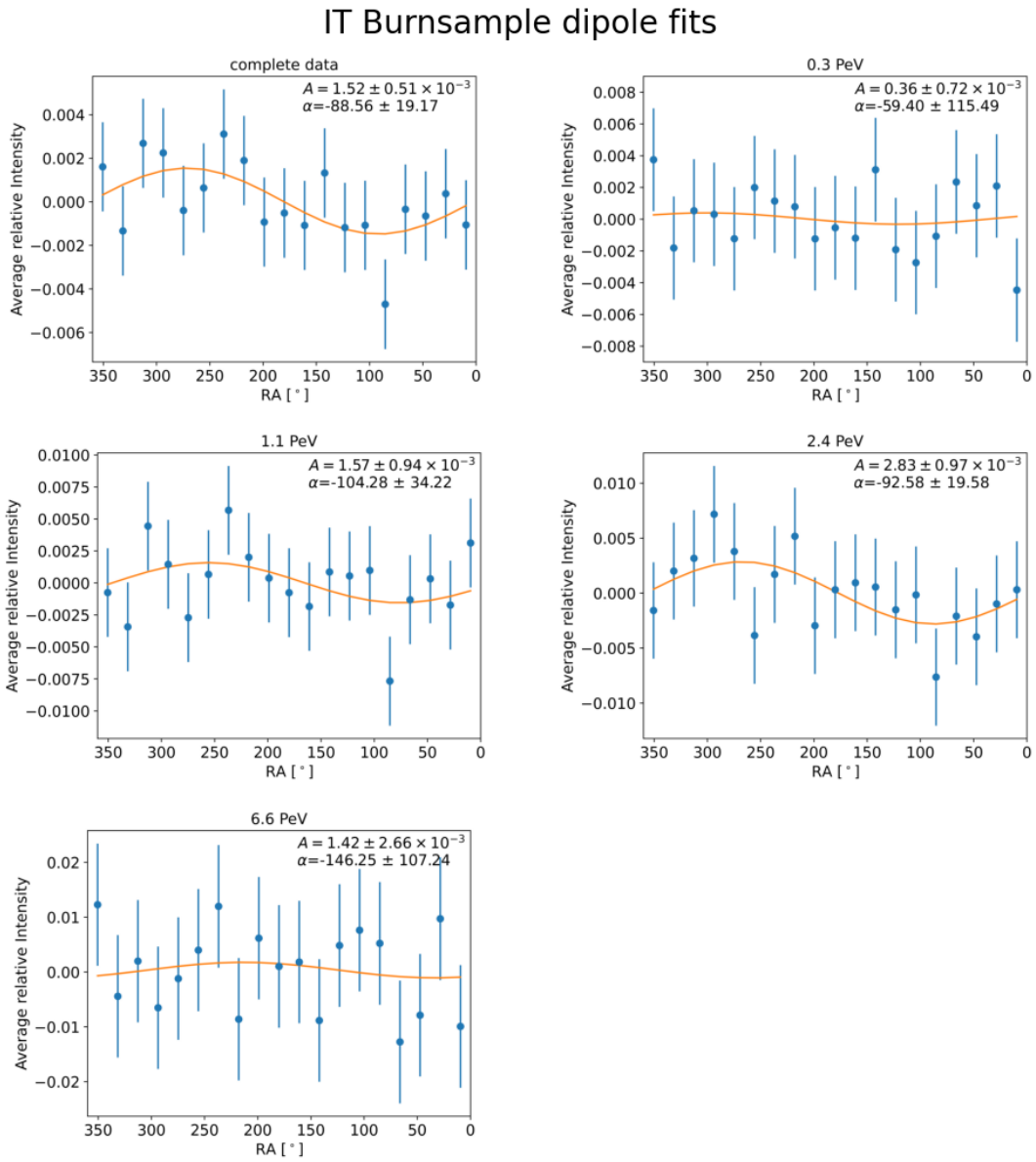

Figure 6.5.: One-dimensional projection for IceTop. The unsmoothed data and background maps were used to calculate an average relative intensity for right ascension bin.

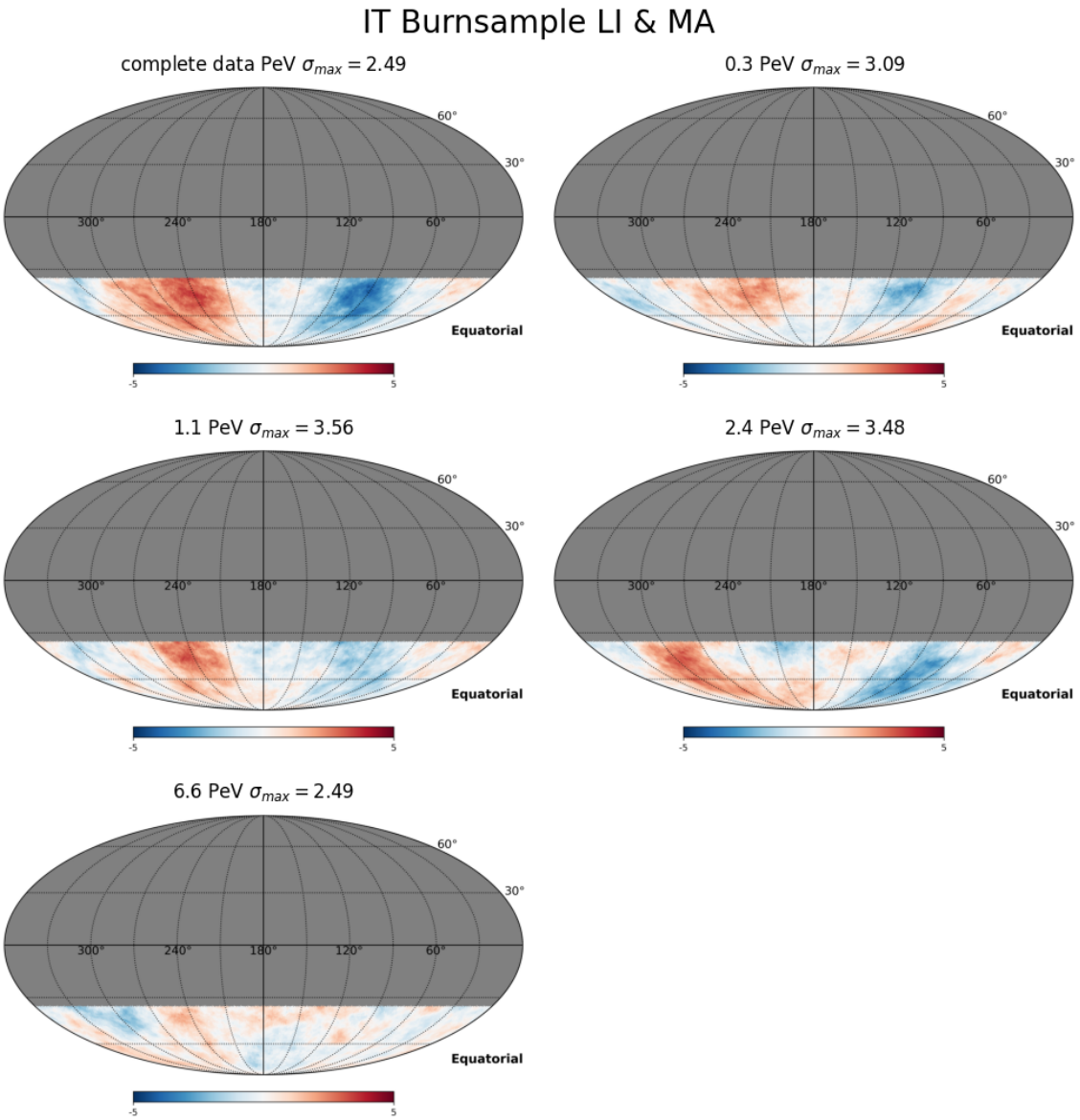

Figure 6.6.: Smoothed sky maps of the reconstructed pre-trial Li & Ma significance for IceTop.

	$E_{med}[TeV]$	$N[10^6]$	$A_{1D}[10^{-3}]$	$\alpha_{1D}[°]$	$A_{2D}[10^{-3}]$	$\alpha_{2D}[°]$	$A_{LLH}[10^{-3}]$	$\alpha_{LLH}[°]$	p-value
complete	/	12.7	1.52 ± 0.51	271 ± 19	3.60 ± 0.84	267 ± 13	3.64 ± 0.85	265 ± 13	0.000120
bin 1	300	5.7	0.36 ± 0.72	301 ± 115	1.93 ± 1.31	247 ± 39	2.06 ± 1.31	246 ± 36	0.295090
bin 2	920	4.1	1.57 ± 0.94	256 ± 34	3.48 ± 1.46	261 ± 24	3.56 ± 1.47	263 ± 24	0.056390
bin 3	2400	2.6	2.83 ± 0.97	267 ± 20	4.80 ± 1.83	274 ± 22	4.65 ± 1.85	269 ± 23	0.044060
bin 4	6900	0.3	1.42 ± 2.66	214 ± 107	3.23 ± 5.18	178 ± 92	3.46 ± 5.18	167 ± 86	0.801270

Table 6.1.: Amplitudes and phases of the dipole reconstruction results. The 1D amplitudes have not been corrected for the limited FOV.

	$A_{1D}[10^{-3}]$	$\alpha_{1D}[^\circ]$
bin 1	0.49 ± 0.11	263.9 ± 12.6
bin 2	1.35 ± 0.12	266.2 ± 5.0
bin 3	1.21 ± 0.15	287.8 ± 7.1
bin 4	1.25 ± 0.38	295.9 ± 17.5

Table 6.2.: Results from previous IceTop study[8]. These are the uncorrected 1D results.

In this work, the data of the 1% burn sample are analysed. The relative intensity, the Li & Ma significance and the one-dimensional dipole fits are calculated as in the previous Chapters. The resulting skymaps are shown in Fig. 6.4 and the dipole fits in Fig. 6.5. The results for the 1% burnsample are shown in table 6.1. The results from Abbasi et al. [8] are presented in the Table 6.2. Note that these are the uncorrected 1D results as presented in the study.

The results are in good agreement with the previous analysis for bins 1, 2, and 4. The amplitude observed in bin 3 is considerably higher than that reported in the previous study. This discrepancy may be attributed to the extremely limited size of the data set, which includes only 1% of the total data. As a result, the statistical sample is too small to provide quantitative results. Nonetheless it shows, that the workflow is correct and provides similiar results as in [8] even for a small sample of the data. The resulting phases and amplitude for IceTop are shown in Fig 5.8. The phase results are similar to those of KASCADE and KASCADE-Grande, although the uncertainties particularly from the dipole LLH are large. An offset is observed between the lowest energy bins of KASCADE and IceTop, as well as between KASCADE-Grande and IceTop. All of the three experiments measured an amplitude that increases with energy and of similar magnitude. A more detailed comparison of the IceTop results as a function of energy and rigidity is presented in the next chapter.

7. Combined Analysis

7.1. Rigidity

The currently available IceTop burnsample data is too small to obtain quantitative results. Nonetheless, with the simulations and the burnsample the possibility for a future combined analysis can be explored.

One goal of this Chapter is to identify KASCADE and KASCADE-Grande bins that match the rigidity distributions of the IceTop bins. Another is to determine the median rigidity for each energy bin analysed in the previous chapters, for both KASCADE and KASCADE-Grande. Anisotropy studies often report only the median energy per bin. But cosmic rays consist of many elements with different charges, and the mass composition changes with energy. If detectors have rigidity-dependent acceptances, the rigidity of the measured cosmic-ray events must be accounted for when comparing results. This was also proposed as an explanation for the differences in the anisotropy results between IceTop and IceCube. For ground-based detectors, the mass or charge of the primaries can not be determined on an event-by-event basis. Therefore, the mean rigidity has to be estimated from Monte Carlo simulations. IceTop and KASCADE-Grande use the CORSIKA (COsmic Ray event Simulation for KAscade) simulation program. CORSIKA [52] allows simulating protons, light nuclei up to iron, photons, and many other particles up to 10^{20} eV [70]. The particle trajectories are simulated until they interact with the atmosphere or decay. It uses a random number generator to produce independent, uniformly distributed numbers, which are used to model the probabilities of interaction, ionisation and deflection in Earth's magnetic field. An important part of the simulation process is the implementation of hadronic interaction models. Because cosmic rays are at energies many magnitudes higher than in man-made accelerators and because interactions occur in a more forward direction, describing these interactions is difficult, and there are several interaction models. Some standard models used in cosmic ray physics are SIBYLL [63], QGSJet [60] and EPOS [62].

Rigidity is defined as:

$$R = \frac{E}{Z} \tag{7.1}$$

where E is the particle energy and Z is the charge of the nucleus. Therefore, in addition to an interaction model, a model that predicts the mass composition as a function of energy is also required. An example is the H4a flux model by Gaisser [42]. This model assumes that cosmic rays until the charge-dependent knee are accelerated by supernova remnants (SNRs) in our Galaxy and the ankle is caused by the transition between galactic and extragalactic sources. If SNRs reach their maximum energy at the knee, forming population 1 and the transition

to extragalactic cosmic rays occurs at the ankle, forming population 3, then the resulting gap needs to be filled by an additional component. This population is called population 2. In addition to this three-population spectrum proposed by Hillas [53], the H4a model assumes a fourth population consisting only of protons. Each population, except the fourth, consists of five groups (p, He, CNO, Mg-Si, Fe) of nuclei, and after a characteristic rigidity, the spectrum cuts off. The rigidity-dependent cutoff is motivated by the fact that both acceleration and propagation depend on the rigidity. As Peters noted [61], the maximum energy a cosmic ray can reach in a cosmic accelerator depends on the size of the acceleration region and thus on the Larmor radius $r_L = R/B$. This means that spectral features appear first for protons, then for helium, and finally for heavier nuclei. The spectrum (or flux) is then given as:

$$\phi_i = \sum_{j=1}^{4} a_{i,j} E^{-\gamma_{i,j}} \cdot \exp\left[\frac{-E}{Z_i R_{c,j}}\right] \tag{7.2}$$

where $a_{i,j}$ are the normalisations, $R_{c,j}$ the characteristic rigidity and $\gamma_{i.j}$ the spectral indices for each population. These parameters for the four populations are listed in Table 7.1. The

R_c	γ	p	He	CNO	Mg–Si	Fe
γ for Pop. 1	–	1.66	1.58	1.63	1.67	1.63
Population 1: 4 PV	see line 1	7860	3550	2200	1430	2120
Pop. 2: 30 PV	1.4	20	20	13.4	13.4	13.4
Pop. 3: 2 EV	1.4	1.7	1.7	1.14	1.14	1.14
Pop. 4 (proton only): 60 EV	1.6	200.	0	0	0	0

Table 7.1.: Rigidity cutoffs and spectral indices for different populations from [40].

spectrum and mass composition according to the H4a Gaisser model is shown in fig. 7.1. The simulations for KASCADE and KASCADE-Grande were performed with a spectral index of $\gamma = 2$. To account for the mass composition and energy-dependent spectral index of the true spectrum, the simulation events have to be reweighted. This is done by dividing the expected flux after the H4a model with the simulated flux:

$$w_i = \frac{\Phi_{H4a}}{\Phi_{sim}} \sim \frac{\Phi_{H4a}}{E^{-2}} \tag{7.3}$$

With these weights, the median energy and rigidity, as well as the rigidity distribution, can be calculated. For KASCADE and KASCADE-Grande the QGSJet-II-04 simulation was used. One effect observed in the unweighted KASCADE-Grande simulations was a second, smaller peak in the distribution of the highest-energy bin. Since this peak is comparatively small relative to the main peak, it has only a minor impact on the median unweighted energy. However, if the events are reweighted, lower-energy events receive larger weights, causing the median of the energy or rigidity distribution to shift toward smaller values. It was investigated what causes the large asymmetry in the highest-energy bin, and it was found that this is due to showers with a negative AGE parameter. A scatter plot of the energy compared to N_{ch} is shown in Fig. 7.2. The AGE parameter describes the shape or steepness of the lateral electron distribution. Common showers should not have values below zero

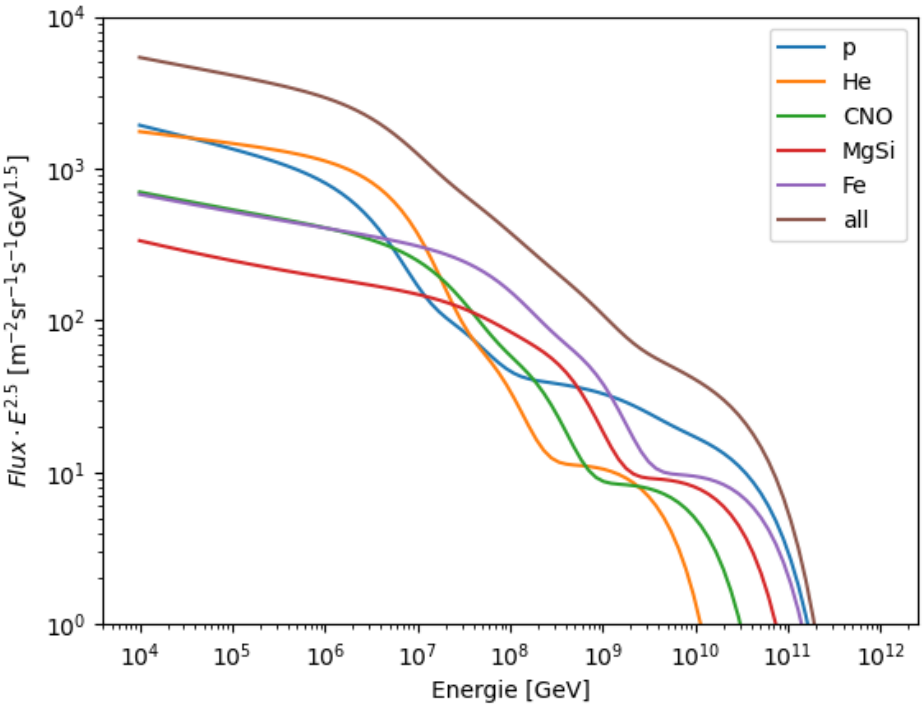

Figure 7.1.: Spectrum and mass composition according to Gaisser H4a composition model [40].

[69] and the AGE distribution for GRANDE is almost completely positive, as shown in Fig. 7.3. Therefore, this might be a simulation artifact and from now on, no simulated showers for KASCADE-Grande with AGE<0 will be considered.

The results after reweighting for the median true energy from the simulations, the median rigidity, and the 0.16 and 0.84 quantiles of the rigidity for the KASCADE and KASCADE-KASCADE-Grande bins are shown in Tables 7.2 and 7.3. For KASCADE, the reconstructed median energies for the previous energy bins (see Table 4.1) agree with the weighted median of the true energies from the simulation. For KASCADE-Grande, the difference between the energies reported results by Chiavassa [33] and the median energies obtained from the reweighted simulations is relatively large, in particular for bin 2 and 3.

In the previous study, the energy was estimated from the attenuation-corrected number of charged particles, assuming a flux of only protons and then applying the energy conversion relation given in [55]. In contrast, the present analysis determines the true median energy directly from simulations using the H4a model.

The different assumptions of the primary mass composition lead to different median energies in each bin. However, for bin 1, a good agreement is observed between the reconstructed and the true median energies. This is expected, since at energies around 2 PeV the proton component is dominant.

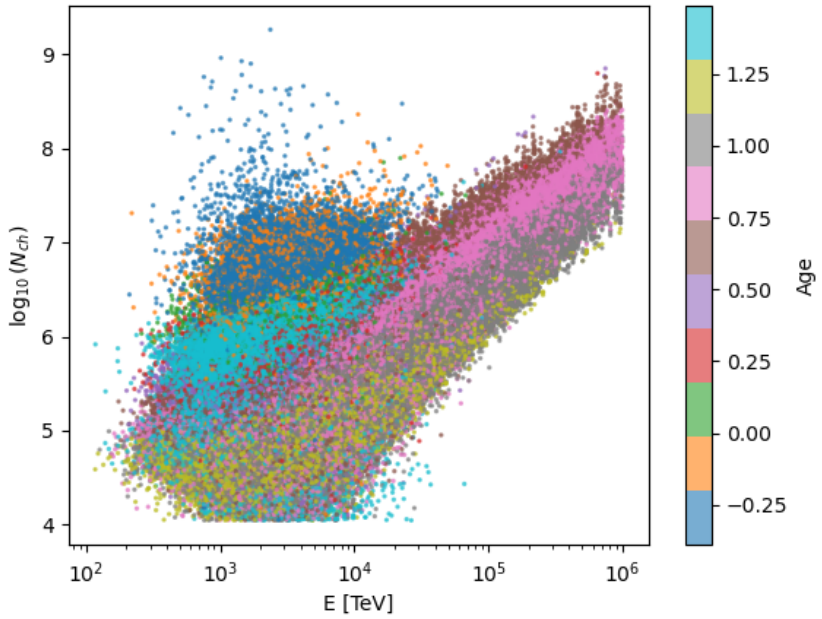

Figure 7.2.: KASCADE-Grande simulations scatter plot of *Nch* compared to energy and age.

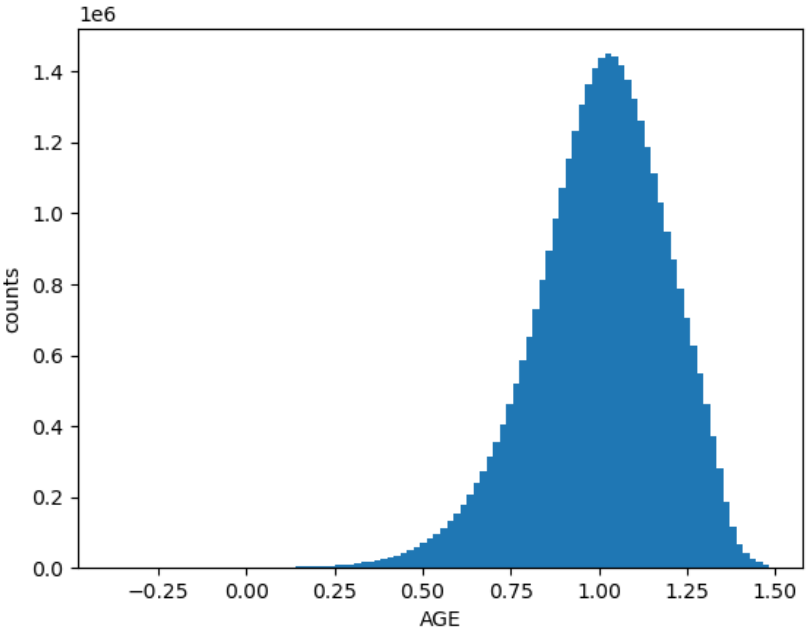

Figure 7.3.: Distribution of the AGE parameter for measured KASCADE-Grande events.

Table 7.2.: Mean reconstructed energies, mean true energies, the corresponding rigidity and the 68% intervals from the rigidity distributions from KASCADE simulations.

Bin	median E_{rec} [TeV]	median E_{true} [TeV]	median R [TV]	68% Interval [TV]
Bin 1	180	154	83	18-156
Bin 2	440	448	221	40-449
Bin 3	1374	1385	625	95-1319
Bin 4	4248	4287	1692	240-3672

Table 7.3.: Mean true energies, the corresponding rigidity and the 68% intervals from the rigidity distributions from KASCADE-Grande simulations.

Bin	median true E [TeV]	median R [TV]	68% Interval [TV]
Bin 1	2496	1108	374-2375
Bin 2	3569	1510	456-3933
Bin 3	16045	3529	993-16357

The IceTop simulations were also reweighted to fit the H4a model with the preexisting simweight weighting function. The resulting energy distributions are shown in Fig. 6.3. The corresponding rigidity distributions are shown in Fig. 7.5. A comparison between the energy and rigidity of bins from the three experiments is shown in Fig. 7.4

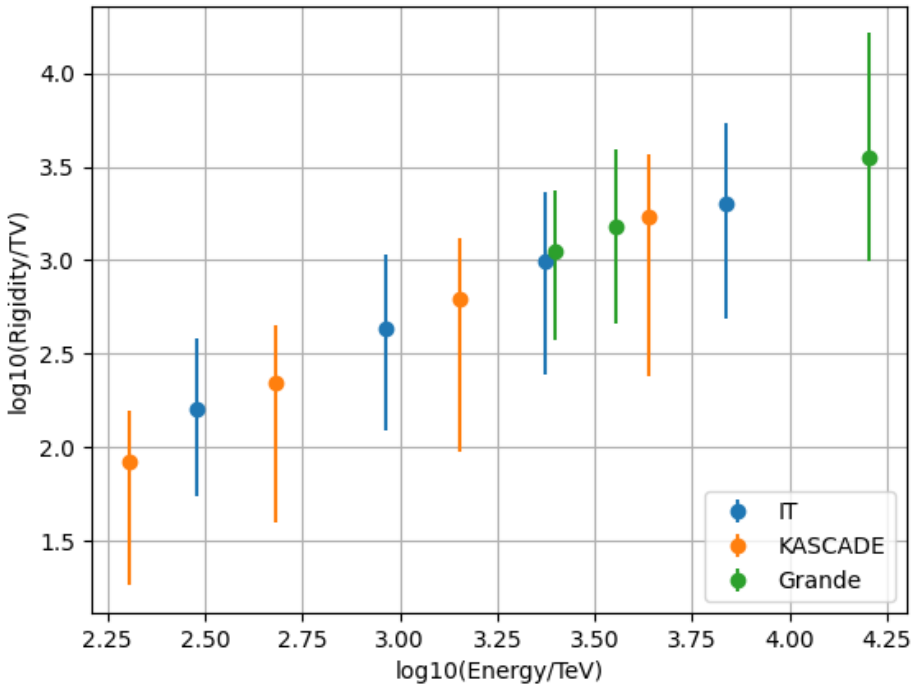

Figure 7.4.: Comparison between the energy and rigidity of IceTop, KASCADE and KASCADE-Grande. The KASCADE-Grande energies estimated in this work have been used.

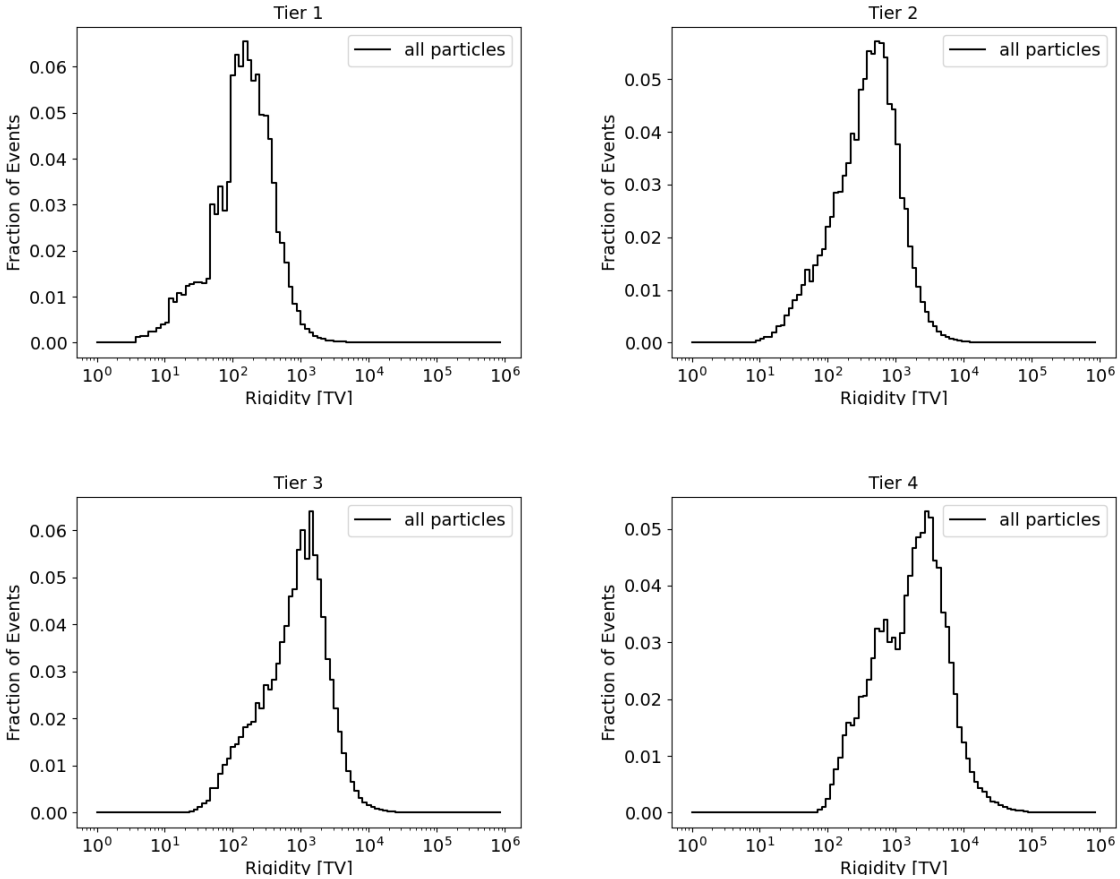

Figure 7.5.: Rigidity distributions for the four IceTop energy tiers.

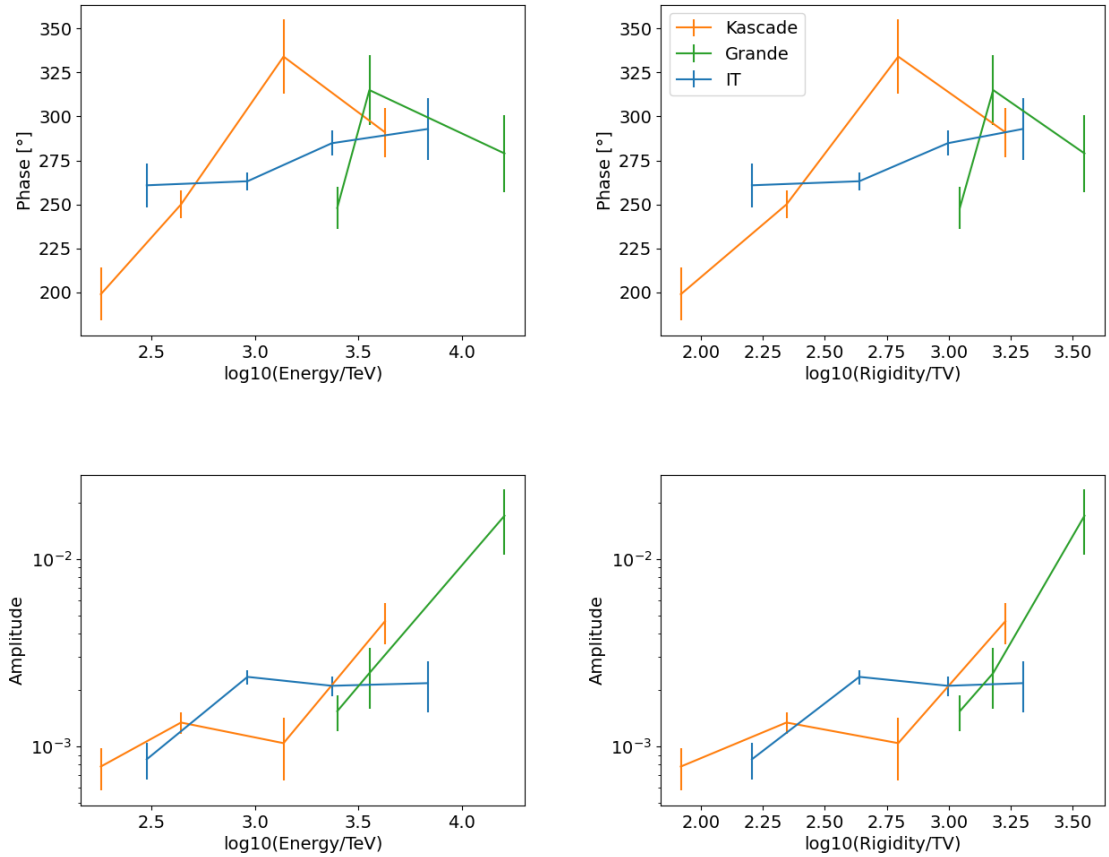

Figure 7.6.: Results for phase (top) and amplitude (bottom) for KASCADE, KASCADE-Grande and IceTop as a function of rigidity (right) and energy (left). All measurements are FOV-corrected one-dimensional results.

A comparison of IceTop results from Abbasi et al. [8], KASCADE and KASCADE-Grande are presented as a function of energy and rigidity in Fig. 7.6. Note that the median true energies from the simulation study in this work was used as the energy. The overall distribution of the results changes only slightly by transforming it from energy to rigidity. Therefore, the rigidity dependence of all detectors is similar and cannot explain the differences observed in the measurements.

The phase corresponding to the second and third energy bins of KASCADE overlaps well with the IceTop results. However, the first and third bins show a large discrepancy. Possible reasons include the energy difference between the first KASCADE and the first IceTop bin, as well as the poor agreement of the third KASCADE bin with the dipole hypothesis, as indicated by the dipole LLH p-value of 0.93. The resulting uncertainties of the phase from the dipole LLH are large enough to overlap with the IceTop result (see Fig. 4.13).

For KASCADE-Grande, the phases are similar for bins 2 and 3, but a discrepancy is again observed for the first energy bin. The amplitude results of the three experiments are in relatively good agreement; only the third bin of KASCADE shows a large deviation. In

addition, the reconstructed amplitudes for the last KASCADE bin and the last KASCADE-Grande bin increase compared to the earlier bins, while the IceTop results remain more stable. For the last IceTop bin in particular, the conversion to rigidity shows better agreement with the KASCADE and KASCADE-Grande results.

7.2. Comparison of IceTop with KASCADE

Since the binning of IceTop is complicated due to the accumulation of snow, this work will keep the IceTop bins fixed and search for KASCADE and KASCADE-Grande bins that match the rigidity distribution of IceTop. For KASCADE, this means that the data are not binned by the reconstructed energy, as this would lead to a sawtooth-shaped rigidity distribution, but by the number of reconstructed charged particles $N_{ch} = N_e + N_\mu$. For KASCADE the Tiers 1,2,3 are overlapping well and the resulting rigidity distributions are compared in Fig. 7.10. The corresponding selections and the median parameters are shown in Table 7.4. Note that the number of events for IceTop refers to the 1% burnsample used in this analysis. The analysis precedure is as in the previous chapters.

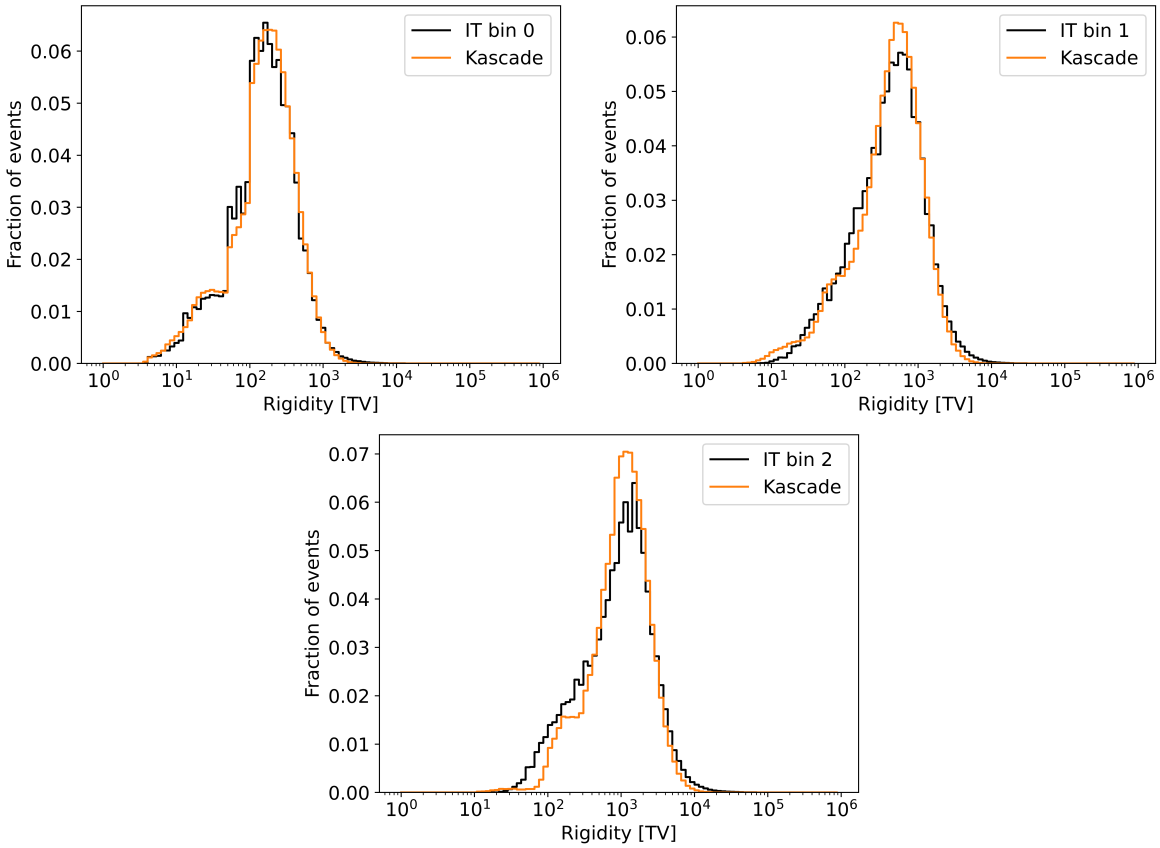

Figure 7.7.: Comparsion between the IT and KASCADE Rigidity distribution.

The resulting anisotropy skymaps are presented in Fig. 7.8 and the corresponding Li & Ma pre-trial significances in Fig. 7.9. The phase of the large-scale dipole is consistent between

	KASCADE				IceTop		
	$N_{ch}[\log_{10}]$ cuts	N [10^6]	true E_{med} [TeV]	$R_{med}[TV]$	N [10^6]	E_{med} [TeV]	R_{med} [TV]
IT/KA bin 1	[4.3,4.7)	122.4	339	168	5.6	300	160
IT/KA bin 2	[4.8,5.2)	21.6	969	445	4.1	920	435
IT/KA bin 3	[5.2,5.6)	4.7	2137	1042	2.6	2350	990

Table 7.4.: KASCADE and IceTop combined energy bins

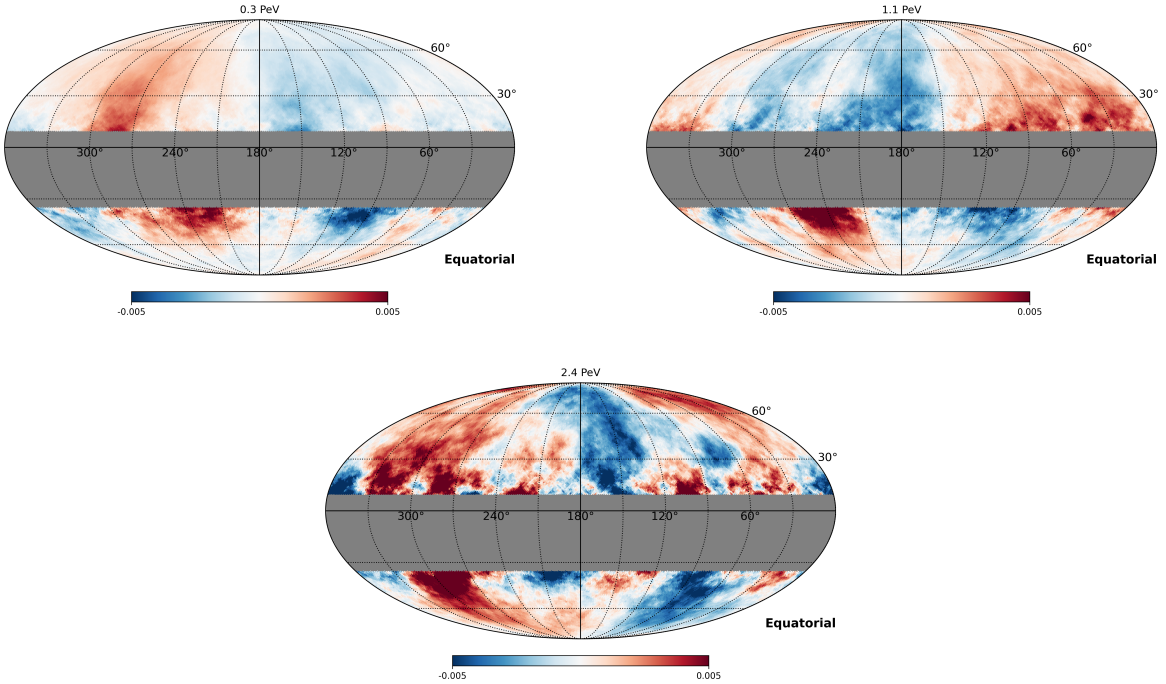

Figure 7.8.: Smoothed anisotropy maps of combined KASCADE and IceTop analysis.

the two experiments in the 0.3 PeV and 2.4 PeV energy bins. However, in the 1.1 PeV bin, the phase differs by approximately 180°. The median energy of this bin is close to that of bin 3 of KASCADE, where the KASCADE analysis already yielded a phase that is not comparable with the IceTop result. Additionally, the amplitude of the relative intensity variations is bigger for IceTop than for KASCADE in the first energy bin. This could also be due to the limited IceTop statistics.

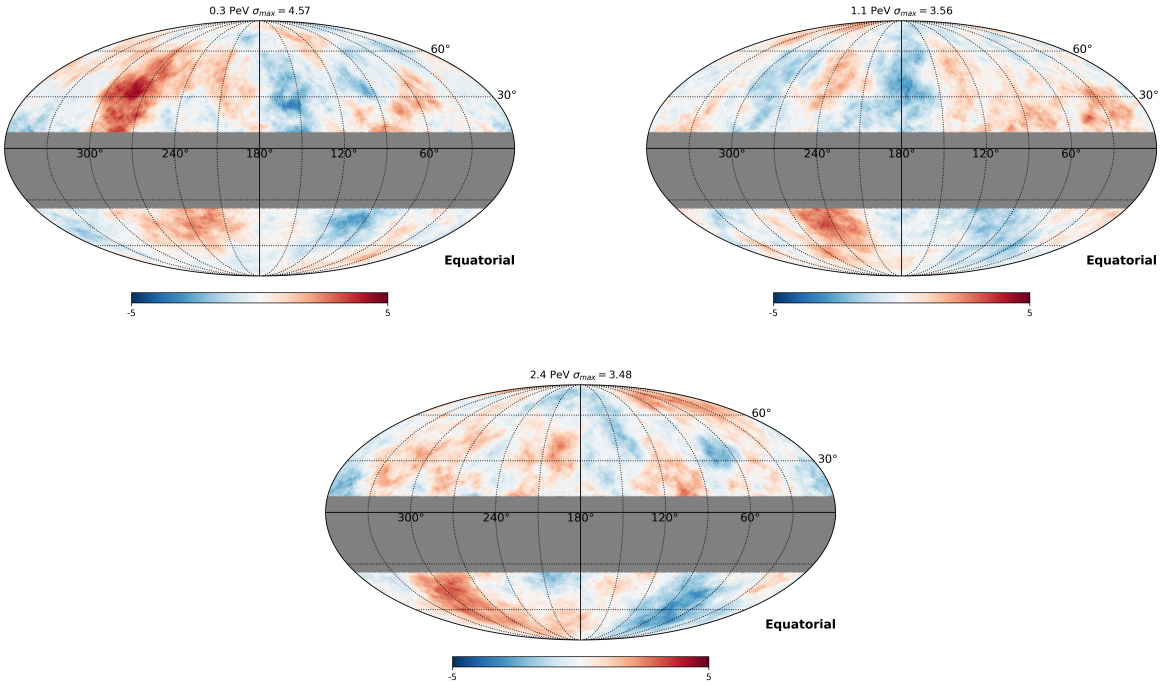

Figure 7.9.: Li & MA pre-trial significances in units of Gaussian σ of combined KASCADE and IceTop analysis.

7.3. Comparison of IceTop with KASCADE-Grande

For the combined analysis between IceTop and KASCADE-Grande, the KASCADE-Grande data were binned by the number of reconstructed charged particles N_{ch} to identify bins with similar rigidity distributions as in IceTop. This was possible for the last two energy bins of IceTop. A comparison of the resulting rigidity distributions is presented in Fig. 7.10. The corresponding selection cuts, the number of events and the resulting median energy and rigidity from the simulation analysis are shown in Table 7.5. Note that the number of events for IceTop refers to the 1% burnsample used in this analysis. The smoothed anisotropy maps for the combined IceTop and KASCADE-Grande bins are presented in Fig. 7.11 and the corresponding Li & Ma significance in Fig. 7.12. The phase of the large-scale dipole is consistent between the two experiments in both energy bins.

	KASCADE-Grande				IceTop		
	$N_{ch}[\log_{10}]$ cuts	N [10^6]	true E_{med} [TeV]	$R_{med}[TV]$	N [10^6]	E_{med} [TeV]	R_{med}
IT/GR bin 1	[5,5.9)	30.6	2324	1029	2.6	2350	990
IT/GR bin 2	$\geq$ 5.6	9.8	4931	1845	0.299	6850	1990

Table 7.5.: KASCADE-Grande and IceTop combined energy bins

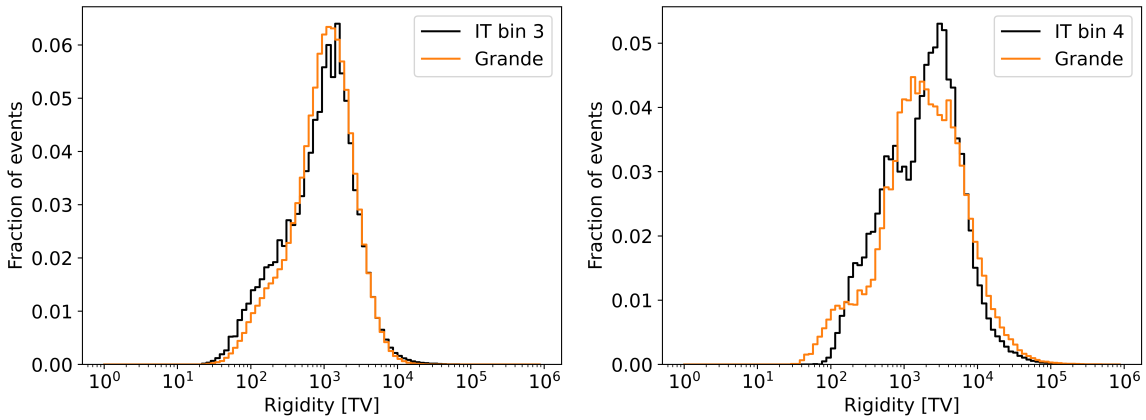

Figure 7.10.: Comparison between the IceTop and KASCADE-Grande Rigidity distribution for the IceTop bin 3 (left) and bin 4 (right).

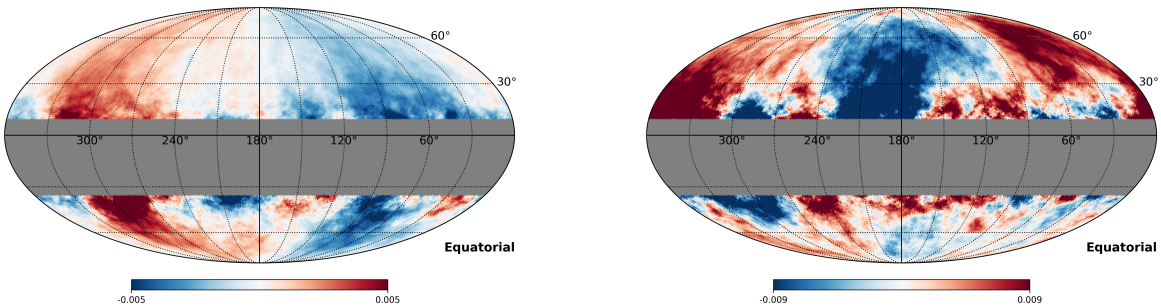

Figure 7.11.: Smoothed anisotropy maps of combined KASCADE-Grande and IceTop analysis for bin 3 (left) and bin 4 (right), respectively.

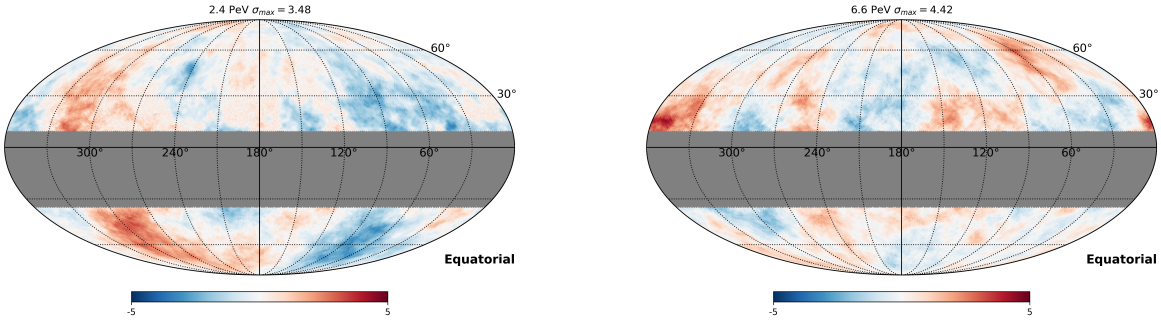

Figure 7.12.: Li & MA pre-trial significances in units of Gaussian σ of combined KASCADE and IceTop analysis.

The combination of the IceTop dataset with the KASCADE and KASCADE-Grande datasets looks promising. And a full analysis with the unblinded IceTop data set, would drastically increase the statics and allow for a combined dipole estimation. Or the search for similar features in the northern and southern hemispheres on smaller scales. However, the detailed analysis could not be performed in the time frame of this thesis. In Future studies, an additional third detector in the mid latitudes could be used to fill the gap between KASCADE and IceTop. An example for this might be GRAPES [32] located in Ooty, India at a latitude of 11.4°.

8. Conclusion and Outlook

In this work, the variations in the arrival directions of cosmic rays for KASCADE and KASCADE-Grande were analysed. To determine the anisotropy, an iterative log-likelihood method was employed. With this method, estimators for the detector acceptance, the relative intensity and the number of events per sidereal time bin were obtained. After determining the anisotropy sky maps, the large-scale anisotropies ($l \leq 1$) were estimated by fitting both the one-dimensional projection in the right ascension and the two-dimensional sky map. As a third method for estimating the dipole, the likelihood was reformulated to depend directly on the components of the dipole vector. By maximising this likelihood, the dipole phase and amplitude were estimated, and the likelihood was further used to assess the significance of the results. The medium-scale anisotropies were estimated by smoothing the anisotropy maps with a 20° top-hat function, and the significance was estimated using the Li & Ma method.

This procedure was described for the KASCADE data set in Section 4.2. And this was the first anisotropy study performed using the complete KASCADE data set. The maximum large-scale significance determined from the dipole likelihood ratio was obtained for the energy bin with a median energy of 439 TeV with a p-value of $1.2 \cdot 10^{-4}$ ($3.66\,\sigma$). The complete data set yields a p-value for a large-scale dipole of $3 \cdot 10^{-5}$ ($4.01\,\sigma$). The most significant medium-scale anisotropy was observed for the lowest energy bin with a median energy of 180 TeV with a maximum absolute post-trial Li & Ma significance of $3.77\,\sigma$. As a next step, systematic checks on the KASCADE data set were performed. The anisotropy was analysed for the complete data set in the sidereal, solar, anti-sidereal and extended-sidereal reference frames and various other systematic selections. The resulting anti-sidereal and extended sidereal amplitudes are of the same order of magnitude as the sidereal distribution. The amplitude in the solar reference frame is also larger than expected. This is probably due to the large gaps in the data taking, seasonal effects and other human-related effects such as recalibration and maintenance.

In Chapter 5, the analysis of the KASCADE-Grande dataset is described. As there are previous analyses with the East-West method and the iterative likelihood method, this enabled us to check our analysis workflow. For the dipole likelihood method, results consistent with those reported in Ahlers [14] were obtained. The one- and two-dimensional results also agree within the uncertainties with the dipole likelihood results. The significance of the large-scale dipole and the medium-scale anisotropies were estimated similarly to the KASCADE analysis. In this case, no significant large- or medium-scale anisotropy was found. The same systematic checks were also performed on KASCADE-Grande. The resulting amplitudes for the anisotropies in the anti-sidereal and extended-sidereal reference frames are of similar magnitude to those obtained in the KASCADE analysis.

To cross-check the significance of the results, toy Monte-Carlo simulations of isotropic event distributions with various sample sizes were performed. The resulting distribution of one-dimensional amplitudes was used to estimate a p-value for the amplitudes obtained for KASCADE and KASCADE-Grande. No resulting amplitude led to a significant p-value. This illustrates how probable amplitudes due to fluctuation of similar size as the expected anisotropies are even for an isotropic distribution. Secondly, the toy Monte-Carlo simulations were analysed with the dipole likelihood method and the resulting likelihood ratio λ was determined. The distribution of likelihood ratios was used to cross-check the p-value obtained from this likelihood ratio for the KASCADE and KASCADE-Grande results and this method seems to estimate the significance well. The medium-scale Li & Ma significance was also determined for the simulations. It was found that the peak of the post-trial significance distribution is at about 2.5σ. This means that the estimation for the number of trials is likely an underestimation.

The analysis of the 1% burnsample of IceTop is described in 6. This does not provide sufficient statistics to allow for a quantitative analysis, but may still be useful for further studies with the 10 % burnsample or the complete data set. After this, the median rigidity for the KASCADE and KASCADE-Grande bins and the IceTop bins was determined with simulations. This also allows us to report the amplitude and phase not only in comparison to the median energy but also to the median rigidity. As the rigidity dependence of different detectors might vary, the difference in the median rigidity of the energy bins could explain some of the differences in the results for the amplitude and phase. But for KASCADE, KASCADE-Grande and IceTop the rigidity dependencies are not large enough to explain the differences in results. Therefore, selection cuts for KASCADE and KASCADE-Grande were identified so that the resulting rigidity distributions are similar to the IceTop rigidity distributions. A combined anisotropy analysis with the 1% IceTop burnsample and KASCADE and KASCADE-Grande was performed. Again, the statistics for IceTop are not large enough for a quantitative study of the combined anisotropy sky maps, but the analysis lays the groundwork for a future combined anisotropy analysis and illustrates its potential. A combination of multiple detectors would allow to increase the statistics and to resolve larger parts of the sky and by that reducing systematic uncertainties. An advantage of a full-sky coverage would be that the true multipole moments could be recovered, rather than only the pseudo multipole moments, and therefore decreasing the systematic effects. A possible future extension might also be the combination with a detector at mid-latitudes, such as GRAPES to achieve a full-sky coverage.

In summary, the KASCADE and KASCADE-Grande anisotropy measurements indicate an energy-increasing dipole pointing toward the Galactic Center. These results are relatively consistent with IceTop and IceCube measurements at lower energies and the results from the Pierre Auger measurement at higher energies.

References

[1] A. Chiavassa et al. “Summary of the main results of the KASCADE and KASCADE-Grande experiments”. In: *EPJ Web Conf.* 208 (2019), p. 03002. DOI: 10.1051/epjconf/201920803002.

[2] A. Aab et al. “Cosmic-Ray Anisotropies in Right Ascension Measured by the Pierre Auger Observatory”. In: *The Astrophysical Journal* 891.2 (Mar. 2020), p. 142. DOI: 10.3847/1538-4357/ab7236.

[3] M. G. Aartsen et al. “Anisotropy in cosmic-ray arrival directions in the Southern Hemisphere based on six years of data from the ICECUBE detector”. In: *The Astrophysical Journal* 826.2 (Aug. 2016), p. 220. DOI: 10.3847/0004-637x/826/2/220.

[4] M. G. Aartsen et al. “Astrophysical neutrinos and cosmic rays observed by IceCube”. In: *Advances in Space Research* 62.10 (Nov. 2018), pp. 2902–2930. ISSN: 0273-1177. DOI: 10.1016/j.asr.2017.05.030.

[5] M. G. Aartsen et al. “Observation of cosmic-ray anisotropy with the IceTop air shower array”. In: *The Astrophysical Journal* 765.1 (Feb. 2013), p. 55. DOI: 10.1088/0004-637X/765/1/55.

[6] R. Abbasi and the IceCube Collaboration. “OBSERVATION OF ANISOTROPY IN THE ARRIVAL DIRECTIONS OF GALACTIC COSMIC RAYS AT MULTIPLE ANGULAR SCALES WITH IceCube”. In: *The Astrophysical Journal* 740.1 (Oct. 2011), p. 16. ISSN: 0004-637X, 1538-4357. DOI: 10.1088/0004-637X/740/1/16. (Visited on 01/13/2026).

[7] R. Abbasi et al. “IceTop: The surface component of IceCube”. In: *Nuclear Instruments and Methods in Physics Research Section A: Accelerators, Spectrometers, Detectors and Associated Equipment* 700 (Feb. 2013), pp. 188–220. ISSN: 0168-9002. DOI: 10.1016/j.nima.2012.10.067.

[8] R. Abbasi et al. *Investigating Energy-Dependent Anisotropy in Cosmic Rays with IceTop Surface Array*. 2025. arXiv: 2507.23044 [astro-ph.HE]. URL: https://arxiv.org/abs/2507.23044.

[9] R. Abbasi et al. “Observation of cosmic-ray anisotropy in the Southern Hemisphere with 12 yr of data collected by the IceCube Neutrino Observatory”. In: *The Astrophysical Journal* 981.2 (Mar. 2025), p. 182. DOI: 10.3847/1538-4357/adb1de.

[10] A. A. Abdo et al. “The large-scale cosmic-ray anisotropy as observed with Milagro”. In: *The Astrophysical Journal* 698.2 (June 2009), p. 2121. DOI: 10.1088/0004-637X/698/2/2121.

[11] A. U. Abeysekara. "All-sky Measurement of the Anisotropy of Cosmic Rays at 10 TeV and Mapping of the Local Interstellar Magnetic Field". In: *The Astrophysical Journal* 871.1 (Jan. 2019), p. 96. DOI: 10.3847/1538-4357/aaf5cc.

[12] A. U. Abeysekara et al. "All-sky Measurement of the Anisotropy of Cosmic Rays at 10 TeV and Mapping of the Local Interstellar Magnetic Field". In: *The Astrophysical Journal* 871.1 (Jan. 2019), p. 96. ISSN: 1538-4357. DOI: 10.3847/1538-4357/aaf5cc.

[13] M. Aglietta et al. "Evolution of the cosmic-ray anisotropy above 10^{14} eV". In: *The Astrophysical Journal* 692.2 (Feb. 2009), p. L130. DOI: 10.1088/0004-637X/692/2/L130.

[14] M. Ahlers. "Large- and medium-scale anisotropies in the arrival directions of cosmic rays observed with Kascade-Grande". In: *The Astrophysical Journal Letters* 886.1 (Nov. 2019). DOI: 10.3847/2041-8213/ab552f.

[15] M. Ahlers. "Searching for all-scale anisotropies in the arrival directions of cosmic rays above the ankle". In: *The Astrophysical Journal* 863.2 (Aug. 2018), p. 146. DOI: 10.3847/1538-4357/aad27c.

[16] M. Ahlers and P. Mertsch. "Origin of small-scale anisotropies in Galactic Cosmic Rays". In: *Progress in Particle and Nuclear Physics* 94 (May 2017), pp. 184–216. DOI: 10.1016/j.ppnp.2017.01.004.

[17] M. Ahlers et al. "A new maximum-likelihood technique for reconstructing cosmic-ray anisotropy at all angular scales". In: *The Astrophysical Journal* 823.1 (May 20, 2016), p. 10. ISSN: 0004-637X, 1538-4357. DOI: 10.3847/0004-637X/823/1/10. (Visited on 01/13/2026).

[18] V.V. Alekseenko et al. "10-100 TeV cosmic ray anisotropy measured at the Baksan EAS "Carpet" array". In: *Nuclear Physics B - Proceedings Supplements* 196 (2009). Proceedings of the XV International Symposium on Very High Energy Cosmic Ray Interactions (ISVHECRI 2008), pp. 179–182. ISSN: 0920-5632. DOI: https://doi.org/10.1016/j.nuclphysbps.2009.09.032.

[19] Rafael Alves Batista et al. "Open Questions in Cosmic-Ray Research at Ultrahigh Energies". In: *Frontiers in Astronomy and Space Sciences* 6 (June 2019). ISSN: 2296-987X. DOI: 10.3389/fspas.2019.00023.

[20] M. Ambrosio et al. "Search for the sidereal and solar diurnal modulations in the total MACRO muon data set". In: *Phys. Rev. D* 67 (4 Feb. 2003), p. 042002. DOI: 10.1103/PhysRevD.67.042002.

[21] M. Amenomori et al. "A Northern Sky Survey for Steady Tera-Electron Volt Gamma-Ray Point Sources Using the Tibet Air Shower Array". In: *The Astrophysical Journal* 633.2 (Nov. 2005), p. 1005. DOI: 10.1086/491612.

[22] M. Amenomori et al. "Large-Scale Sidereal Anisotropy of Galactic Cosmic-Ray Intensity Observed by the Tibet Air Shower Array". In: *The Astrophysical Journal* 626.1 (May 2005), pp. L29–L32. ISSN: 1538-4357. DOI: 10.1086/431582.

[23] M. Amenomori et al. "Northern Sky Galactic Cosmic Ray Anisotropy between 10 and 1000 TeV with the Tibet Air Shower Array". In: *The Astrophysical Journal* 836.2 (Feb. 2017), p. 153. ISSN: 1538-4357. DOI: 10.3847/1538-4357/836/2/153.

[24] Carl D. Anderson. “The Apparent Existence of Easily Deflectable Positives”. In: *Science* 76.1967 (1932), pp. 238–239. DOI: 10.1126/science.76.1967.238. eprint: https://www.science.org/doi/pdf/10.1126/science.76.1967.238.

[25] T. Antoni et al. “KASCADE measurements of energy spectra for elemental groups of cosmic rays: Results and open problems”. In: *Astroparticle Physics* 24.1–2 (Sept. 2005), pp. 1–25. ISSN: 0927-6505. DOI: 10.1016/j.astropartphys.2005.04.001.

[26] T. Antoni et al. “The cosmic-ray experiment KASCADE”. In: *Nuclear Instruments and Methods in Physics Research Section A: Accelerators, Spectrometers, Detectors and Associated Equipment* 513.3 (2003), pp. 490–510. ISSN: 0168-9002. DOI: https://doi.org/10.1016/S0168-9002(03)02076-X.

[27] W. D. Apel et al. “Ankle-like feature in the energy spectrum of light elements of cosmic rays observed with KASCADE-Grande”. In: *Physical Review D* 87.8 (Apr. 2013). ISSN: 1550-2368. DOI: 10.1103/physrevd.87.081101.

[28] W. D. Apel et al. “Kneelike Structure in the Spectrum of the Heavy Component of Cosmic Rays Observed with KASCADE-Grande”. In: *Physical Review Letters* 107.17 (Oct. 2011). ISSN: 1079-7114. DOI: 10.1103/physrevlett.107.171104.

[29] W. D. Apel et al. “Search for Large-scale Anisotropy in the Arrival Direction of Cosmic Rays with KASCADE-Grande”. In: *The Astrophysical Journal* 870.2 (Jan. 2019), p. 91. DOI: 10.3847/1538-4357/aaf1ca.

[30] W. D. Apel et al. “The KASCADE-Grande experiment”. In: *Nuclear Instruments and Methods in Physics Research Section A: Accelerators, Spectrometers, Detectors and Associated Equipment* 620.2 (2010), pp. 202–216. ISSN: 0168-9002. DOI: https://doi.org/10.1016/j.nima.2010.03.147.

[31] B. Bartoli et al. “ARGO-YBJ Observation of the large-scale cosmic ray anisotropy during the solar minimum between cycles 23 and 24”. In: *The Astrophysical Journal* 809.1 (Aug. 2015), p. 90. DOI: 10.1088/0004-637X/809/1/90.

[32] M. Chakraborty et al. “Small-scale Cosmic-Ray Anisotropy Observed by the GRAPES-3 Experiment at TeV Energies”. In: *The Astrophysical Journal* 961.1 (Jan. 2024), p. 87. DOI: 10.3847/1538-4357/ad132b.

[33] A. Chiavassa. “A study of the first harmonic of the large scale anisotropies with the KASCADE-Grande Experiment”. In: *Proceedings of The 34th International Cosmic Ray Conference — PoS(ICRC2015)* (Aug. 2016), p. 281. DOI: 10.22323/1.236.0281.

[34] Arthur H. Compton and Ivan A. Getting. “An apparent effect of galactic rotation on the intensity of Cosmic Rays”. In: *Physical Review* 47.11 (June 1935), pp. 817–821. DOI: 10.1103/physrev.47.817.

[35] O. Deligny. “Cosmic-Ray Anisotropies: A Review”. In: *25th European Cosmic Ray Symposium*. Dec. 2016. arXiv: 1612.08002 [astro-ph.HE].

[36] Juan Carlos Díaz Vélez et al. “Harmonic Interference of Earth’s orbital velocity and the sidereal Cosmic Ray Anisotropy”. In: *Proceedings of 37th International Cosmic Ray Conference — PoS(ICRC2021)* (July 2021), p. 085. DOI: 10.22323/1.395.0085.

[37] Ralph Engel, Dieter Heck, and Tanguy Pierog. "Extensive air showers and hadronic interactions at high energy". In: *Annual Review of Nuclear and Particle Science* 61.1 (Nov. 2011), pp. 467–489. DOI: 10.1146/annurev.nucl.012809.104544.

[38] J. Engler et al. "A warm-liquid calorimeter for cosmic-ray hadrons". In: *Nuclear Instruments and Methods in Physics Research Section A: Accelerators, Spectrometers, Detectors and Associated Equipment* 427.3 (1999), pp. 528–542. ISSN: 0168-9002. DOI: https://doi.org/10.1016/S0168-9002(99)00051-0.

[39] Stefano Gabici et al. "The origin of Galactic Cosmic Rays: Challenges to the standard paradigm". In: *International Journal of Modern Physics D* 28.15 (Nov. 2019), p. 1930022. DOI: 10.1142/s0218271819300222.

[40] T. K. Gaisser. "Spectrum of cosmic-ray nucleons, Kaon production, and the atmospheric muon charge ratio". In: *Astroparticle Physics* 35.12 (July 2012), pp. 801–806. DOI: 10.1016/j.astropartphys.2012.02.010.

[41] T. K. Gaisser, R. Engel, and E. Resconi. *Cosmic rays and particle physics*. Cambridge University Press, 2016.

[42] T. K. Gaisser, T. Stanev, and S. Tilav. "Cosmic Ray Energy Spectrum from measurements of Air Showers". In: *Frontiers of Physics* 8.6 (Apr. 2013), pp. 748–758. DOI: 10.1007/s11467-013-0319-7.

[43] Wei Gao et al. "Observation of large-scale anisotropy in the arrival directions of cosmic rays with LHAASO". In: *PoS* ICRC2021 (2021), p. 351. DOI: 10.22323/1.395.0351.

[44] K. M. Górski et al. "HEALPix: A Framework for High-Resolution Discretization and Fast Analysis of Data Distributed on the Sphere". In: *The Astrophysical Journal* 622.2 (Apr. 2005), p. 759. DOI: 10.1086/427976.

[45] Kenneth Greisen. "End to the Cosmic-Ray Spectrum?" In: *Phys. Rev. Lett.* 16 (17 Apr. 1966), pp. 748–750. DOI: 10.1103/PhysRevLett.16.748.

[46] Particle Data Group et al. "Review of Particle Physics". In: *Progress of Theoretical and Experimental Physics* 2022.8 (Aug. 2022), p. 083C01. ISSN: 2050-3911. DOI: 10.1093/ptep/ptac097. eprint: https://academic.oup.com/ptep/article-pdf/2022/8/083C01/49175539/ptac097.pdf.

[47] Claus Grupen. "The history of Cosmic Ray Studies after Hess". In: *Nuclear Physics B - Proceedings Supplements* 239–240 (June 2013), pp. 19–25. DOI: 10.1016/j.nuclphysbps.2013.05.003.

[48] G. Guillian and Hosaka. "Observation of the anisotropy of 10 TeV primary cosmic ray nuclei flux with the Super-Kamiokande-I detector". In: *Phys. Rev. D* 75 (6 Mar. 2007), p. 062003. DOI: 10.1103/PhysRevD.75.062003.

[49] A. Haungs et al. "KASCADE-Grande: Composition studies in the view of the post-LHC hadronic interaction models". In: *EPJ Web of Conferences* 145 (2017), p. 13001. DOI: 10.1051/epjconf/201714513001.

[50] A. Haungs et al. "The KASCADE Cosmic-ray Data Centre KCDC: granting open access to astroparticle physics research data". In: *The European Physical Journal C* 78.9 (Sept. 2018). ISSN: 1434-6052. DOI: 10.1140/epjc/s10052-018-6221-2.

[51] Andreas Haungs, Heinigerd Rebel, and Markus Roth. “Energy Spectrum and mass composition of high-energy cosmic rays”. In: *Reports on Progress in Physics* 66.7 (June 2003), pp. 1145–1206. DOI: 10.1088/0034-4885/66/7/202.

[52] D. Heck et al. *CORSIKA: a Monte Carlo code to simulate extensive air showers.* 1998.

[53] A. M. Hillas. “Can diffusive shock acceleration in supernova remnants account for high-energy galactic cosmic rays?” In: *Journal of Physics G: Nuclear and Particle Physics* 31.5 (Apr. 2005), R95. DOI: 10.1088/0954-3899/31/5/R02.

[54] A. M. Hillas. “The Origin of Ultra-High-Energy Cosmic Rays”. In: *ARA&A* 22 (Jan. 1984), pp. 425–444. DOI: 10.1146/annurev.aa.22.090184.002233.

[55] D Kang et al. “All-particle energy spectrum of KASCADE-Grande based on shower size and different hadronic interaction models”. In: *Journal of Physics: Conference Series* 409 (Feb. 2013), p. 012101. ISSN: 1742-6596. DOI: 10.1088/1742-6596/409/1/012101.

[56] T.-P. Li and Y.-Q. Ma. “Analysis methods for results in gamma-ray astronomy”. In: *The Astrophysical Journal* 272 (Sept. 1983), p. 317. DOI: 10.1086/161295.

[57] Gernot Maier. “Suche nach Anisotropie in der kosmischen Strahlung mit dem KASCADE Experiment”. Available at https://astro.uni-wuppertal.de/fileadmin/physik/astro/mainpage/publications/theses/PhD/Maier-Promo.pdf. Dissertation. Universität (TH) Karlsruhe, Mar. 2004.

[58] J. Matthews. “A Heitler model of extensive Air Showers”. In: *Astroparticle Physics* 22.5–6 (Jan. 2005), pp. 387–397. DOI: 10.1016/j.astropartphys.2004.09.003.

[59] S. Navas et al. “Review of particle physics”. In: *Phys. Rev. D* 110.3 (2024), p. 030001. DOI: 10.1103/PhysRevD.110.030001.

[60] S. Ostapchenko. “QGSJET-II: towards reliable description of very high energy hadronic interactions”. In: *Nuclear Physics B - Proceedings Supplements* 151.1 (Jan. 2006), pp. 143–146. ISSN: 0920-5632. DOI: 10.1016/j.nuclphysbps.2005.07.026.

[61] B. Peters. “Primary cosmic radiation and extensive Air Showers”. In: *Il Nuovo Cimento* 22.4 (Nov. 1961), pp. 800–819. DOI: 10.1007/bf02783106.

[62] T. Pierog and K. Werner. “EPOS Model and Ultra High Energy Cosmic Rays”. In: *Nuclear Physics B - Proceedings Supplements* 196 (Dec. 2009), pp. 102–105. ISSN: 0920-5632. DOI: 10.1016/j.nuclphysbps.2009.09.017.

[63] Ralph Engel et al. “The hadronic interaction model Sibyll - past, present and future”. In: *EPJ Web Conf.* 145 (2017), p. 08001. DOI: 10.1051/epjconf/201614508001.

[64] Frank G. Schröder. “Radio detection of cosmic-ray air showers and high-energy neutrinos”. In: *Progress in Particle and Nuclear Physics* 93 (Mar. 2017), pp. 1–68. DOI: 10.1016/j.ppnp.2016.12.002.

[65] G. Di Sciascio and R. Iuppa. *On the Observation of the Cosmic Ray Anisotropy below 10^{15} eV*. 2014. arXiv: 1407.2144 [astro-ph.HE]. URL: https://arxiv.org/abs/1407.2144.

[66] J. C. Diaz Velez. *cra-ahlers-llh: Iterative log-likelihood reconstruction for CRA*. https://github.com/jcdiazvelez/cra-ahlers-llh. 2026.

[67] Michael Walter. “Early Cosmic Ray Research with balloons”. In: *Nuclear Physics B - Proceedings Supplements* 239–240 (June 2013), pp. 11–18. DOI: 10.1016/j.nuclphysbps.2013.05.002.

[68] S. S. Wilks. “The Large-Sample Distribution of the Likelihood Ratio for Testing Composite Hypotheses”. In: *The Annals of Mathematical Statistics* 9.1 (1938), pp. 60–62. ISSN: 00034851, 21688990. (Visited on 02/25/2026).

[69] Jürgen Wochele et al. *KCDC manual*. URL: https://kcdc.iap.kit.edu/static/pdf/kcdc_mainpage/kcdc-Manual.pdf.

[70] Jürgen Wochele et al. *KCDC simulation manual - KASCADE, GRANDE and CALORIMETER Simulations*. URL: https://kcdc.iap.kit.edu/static/pdf/kcdc_mainpage/kcdc-Simulation-Manual.pdf.

[71] E. O. Wollan. “Present status of solar and sidereal time variation of Cosmic Rays”. In: *Reviews of Modern Physics* 11.3–4 (July 1939), pp. 160–165. DOI: 10.1103/revmodphys.11.160.

[72] G. T. Zatsepin and V. A. Kuzmin. “Upper limit of the spectrum of cosmic rays”. In: *JETP Lett.* 4 (1966), pp. 78–80.

[73] Andrea Zonca et al. “healpy: equal area pixelization and spherical harmonics transforms for data on the sphere in Python”. In: *Journal of Open Source Software* 4.35 (2019), p. 1298. DOI: 10.21105/joss.01298.

A. Appendix

A.1. KASCADE-Grande pre-trial significance with final iterators

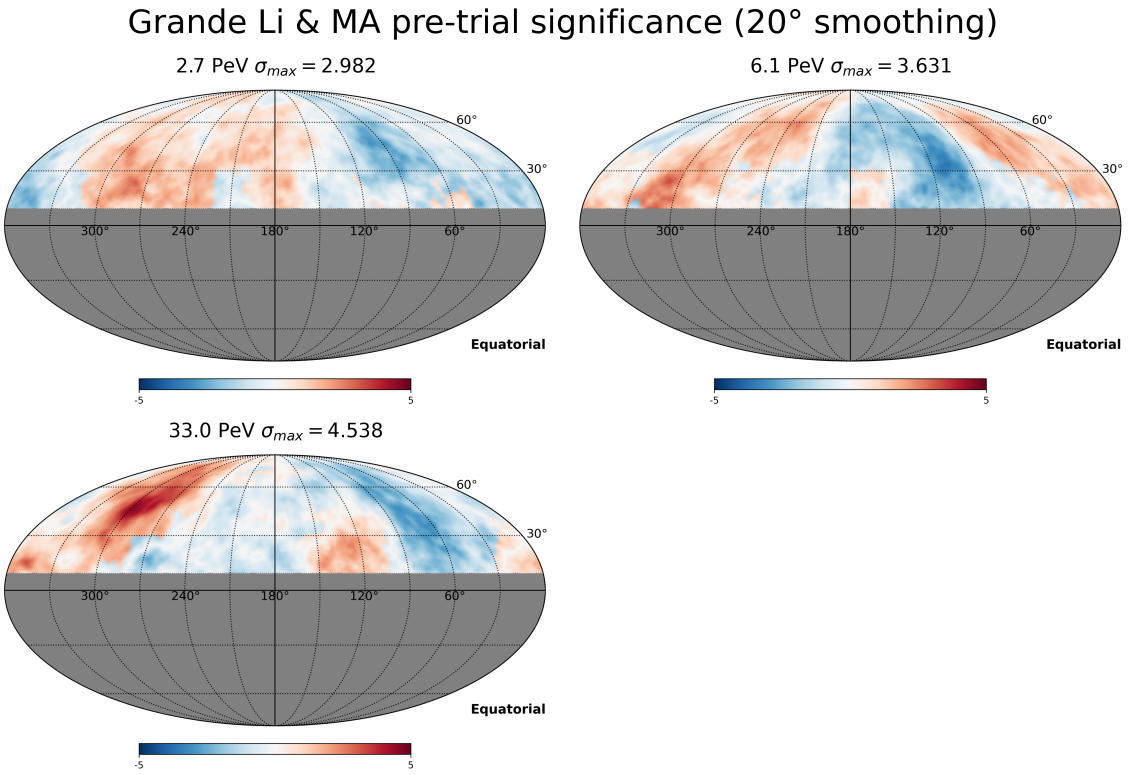

Figure A.1.: Grande pre-trial significance maps, where the final iterators for the acceptance and norm have been used to calculate $\tilde{\mu}_{\mathfrak{a}}^{\mathrm{bg}}$

Acknowledgements

I would like to thank Ralph Engel for supervising this thesis and for the productive and frequent discussions throughout the project. I am also grateful to Thomas Schwetz-Mangold for reviewing this thesis.

I would especially like to thank my advisor, Donghwa Kang, for her continuous support throughout this work and for her indispensable expertise and feedback, without which this thesis would not have been possible.

I also thank Andreas Haungs for his valuable feedback during the writing of this thesis and for his warm welcome at the IAP. In addition, I would like to thank Wenjie Hou for his insights on the anisotropy studies and the various analysis methods. More generally, I am grateful to everyone in the IceCube group for the welcoming environment and the pleasant working atmosphere.

Furthermore, I would like to thank Paolo Desiati and Juan Carlos Díaz Vélez for their help with the analysis method, the IceTop data, and their many inputs on the systematic studies.

Lastly, I would like to thank my family for their constant support throughout my studies and during the completion of this thesis.